Multiscale modeling of optical and transport properties of solids and nanostructures

Yia-Chung Chang

Research Center for Applied Sciences (RCAS)
Academia Sinica, Taiwan

NTU Colloquium , March 14, 2017

In collaboration with

Ming-Ting Kuo, NCU

S. J. Sun, J. Velev, Gefei Qian, Hye-Jung Kim, UIUC

Zhenhua Ning, Chih-Chieh Chen, UIUC/RCAS

Ching-Tang Liang, I-Lin Ho, RCAS

J. W. Davenport, R. B. James, BNL

T. O. Cheche, U. Burcharest, W. E. Mahmoud

Outline

- Optical excitations of solids/nanostructures modeled by: density-functional theory (DFT), tight-binding (TB), k.p model, and effective bond-orbital model (EBOM)
- Transport and thermoelectric properties of nanostructure junctions modeled by non-equilibrium Green function method, including correlation
- Examples: zincblende/cubic semiconductors, quantum wires, and QDs and QD tunnel junctions

Excitation spectra

Flow chart of BSE calculation for excitation spectra

[G. Onida, L. Reining, A. Rubio

Rev. Mod. Phys., **74,** 601, (2002)]

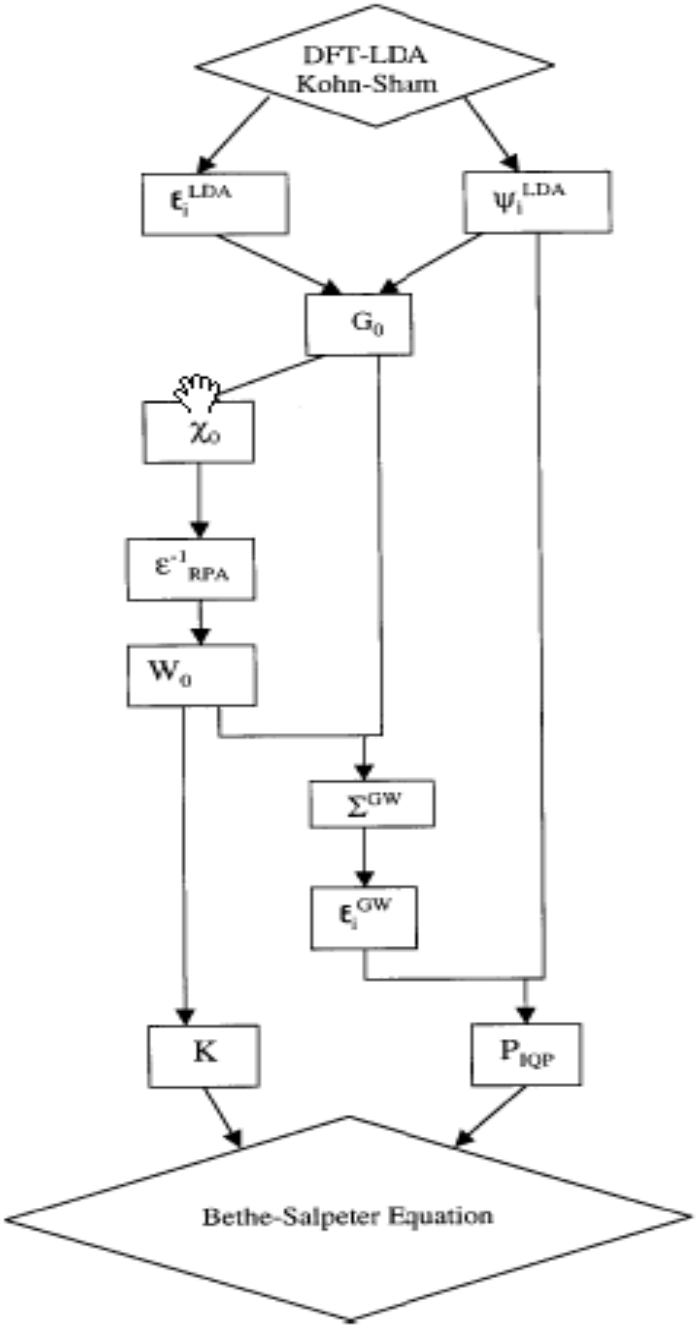

DFT packages:

VASP, CASTEP

Abinit

WIEN2K

LMTO

SIESTA

LASTO

Linearized Slater-type orbital (LASTO) method

[J. W. Davenport, Phys. Rev. B 29, 2896 (1994)]

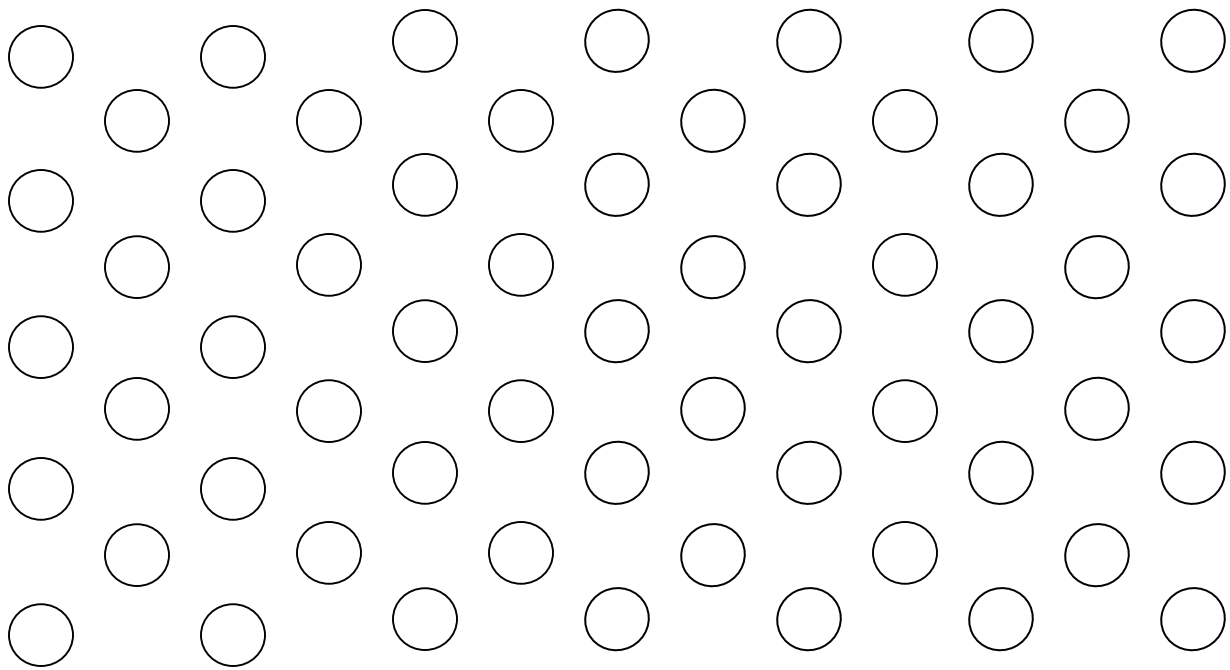

- Inside MTs: exact numerical solution (u) & du/dE
- Outside MTs: Slater-type orbitals, $r^{n-1}\, e^{-br}\, Y_{lm}(\Omega)$
- Match boundary conditions for each spherical harmonics

Symmetry-adapted basis

[Y.-C. Chang, R. B. James, and J. W. Davenport, PRB **73**, 035211 (2006)]

Use of symmetry can reduce the computation effort significantly

- Symmetry-adapted basis was not commonly adopted in DFT calculations
- (For general k, point symmetry is lost)
- For large supercell calculations, only k=0 is needed, the use of symmetry-adated basis can be very beneficial
- Examples:

1. Defects in solids with high point symmetry
2. High-symmetry nanoparticles like C60.
3. Optical excitations of nanoclusters
4. Excitonic excitation of solids with high symmetry

128-atom fcc supercell

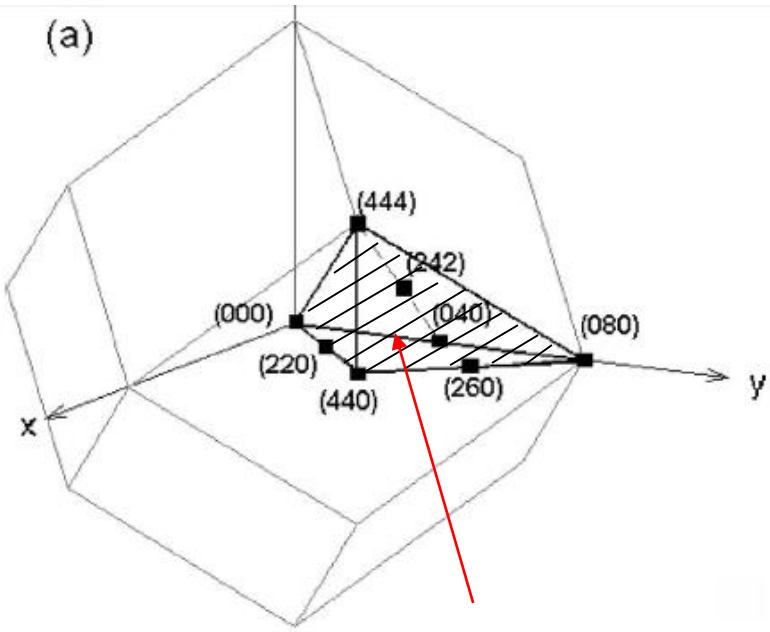

•Irreducible segment

Optically allowed transitions for T_d group

- Only the following 6 (& exch.) out of 100 possible configurations are allowed:

$$\langle\Gamma_1|p_x|\Gamma_{5x}\rangle,\ \langle\Gamma_{3u}|p_x|\Gamma_{5x}\rangle,\ \langle\Gamma_{4y}|p_x|\Gamma_{5z}\rangle,\ \langle\Gamma_{5y}|p_x|\Gamma_{5z}\rangle,\ \langle\Gamma_2|p_x|\Gamma_{5x}\rangle,\ \langle\Gamma_{3u}|p_x|\Gamma_{5x}\rangle$$

- Polarization matrix in RPA:

$$P^0_{\mathbf{G}\mathbf{G}'}(\omega) = \sum_i^{occ}\sum_j^{unocc} \zeta_{ij}(\mathbf{G})\zeta^*_{ij}(\mathbf{G}') \cdot \left[\frac{1}{\omega-\omega_{ij}} - \frac{1}{\omega+\omega_{ij}}\right]$$

$$\zeta_{ij}(\mathbf{G}) \equiv \int d\mathbf{r} e^{i\mathbf{G}\mathbf{r}}\phi_i(\mathbf{r})\phi^*_j(\mathbf{r})$$

[Use FFT]

- Polarization matrix in symmetry-adapted basis:

$$P^0_{\Gamma,s,s'}(\omega) = \sum_{l_i}^{occ}\sum_{l_j}^{unocc} \zeta_{l_i,l_j}(\Gamma,s)\zeta^*_{l_il_j}(\Gamma,s') \cdot \left[\frac{1}{\omega-\omega_{ij}} - \frac{1}{\omega+\omega_{ij}}\right],$$

$$\zeta_{ij}(\Gamma\nu,s) \equiv \sum_{\mathbf{G}} c^{\Gamma\nu}(s,\mathbf{G})\zeta_{ij}(\mathbf{G}).$$

Using Wigner-Ekart theorem:

$$\zeta_{ij}(\Gamma\nu,s) = \zeta_{l_i,l_j}(\Gamma,s)V(\gamma_i,\gamma_j,\Gamma;\nu_i,\nu_j,\nu),$$

Optical spectra calculated by Bathe-Salpeter Eq. in LASTO basis

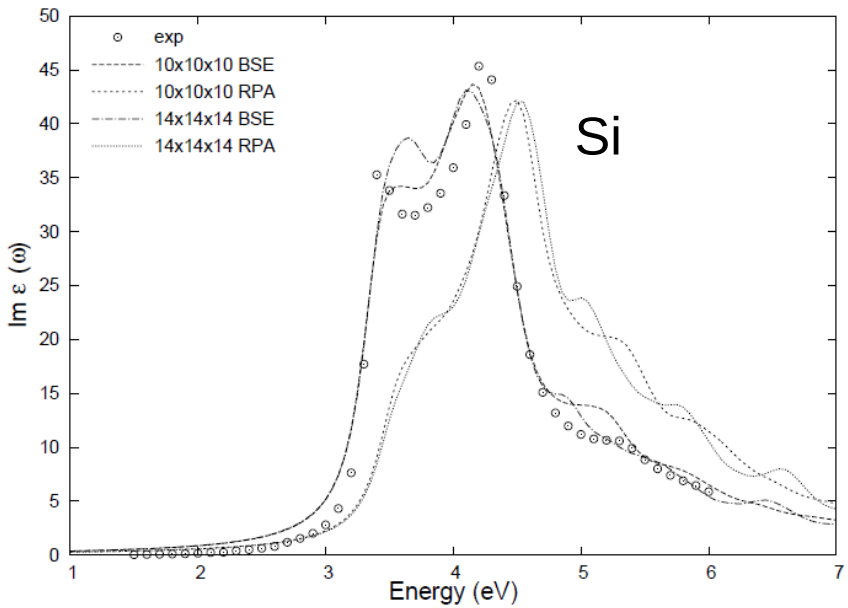

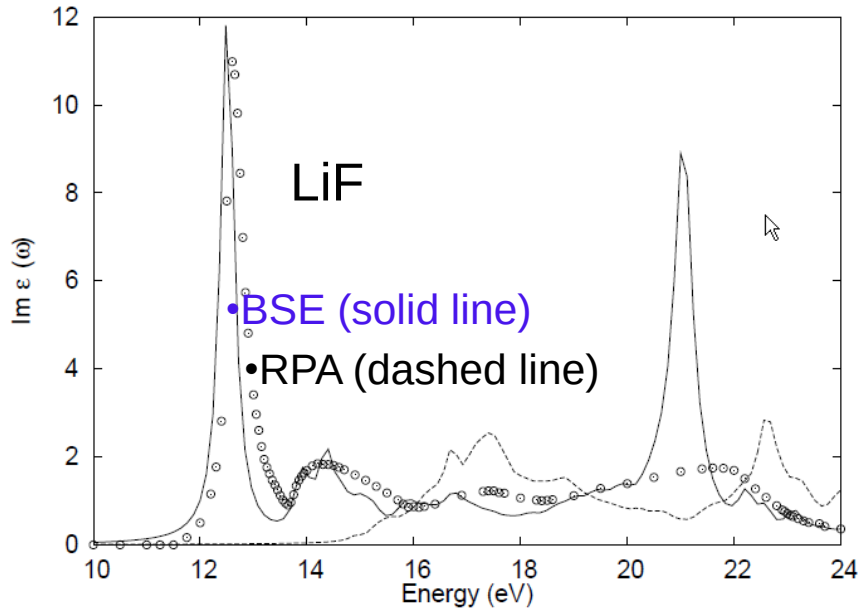

- Results similar to LAPW results:
- [Puschnig* and C. Ambrosch-Draxl, PRB **66**, 165105 (2002)]

Optical spectra of GaAs, AlAs & SLs

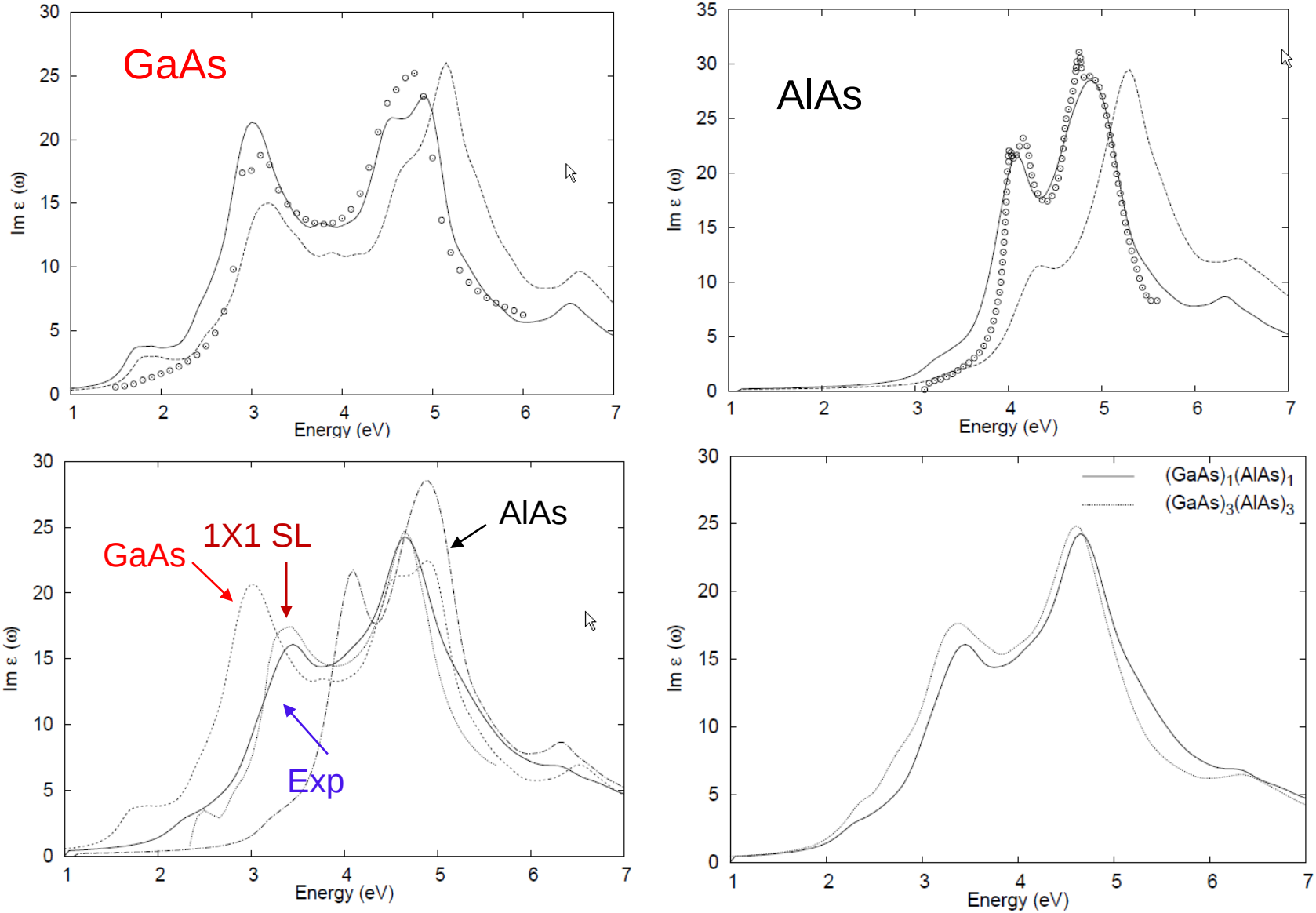

[Exp. data taken from [M. Garriga et al., Phys. Rev. B **36**, 3254 (1987)]

Supercell method in plane-wave basis

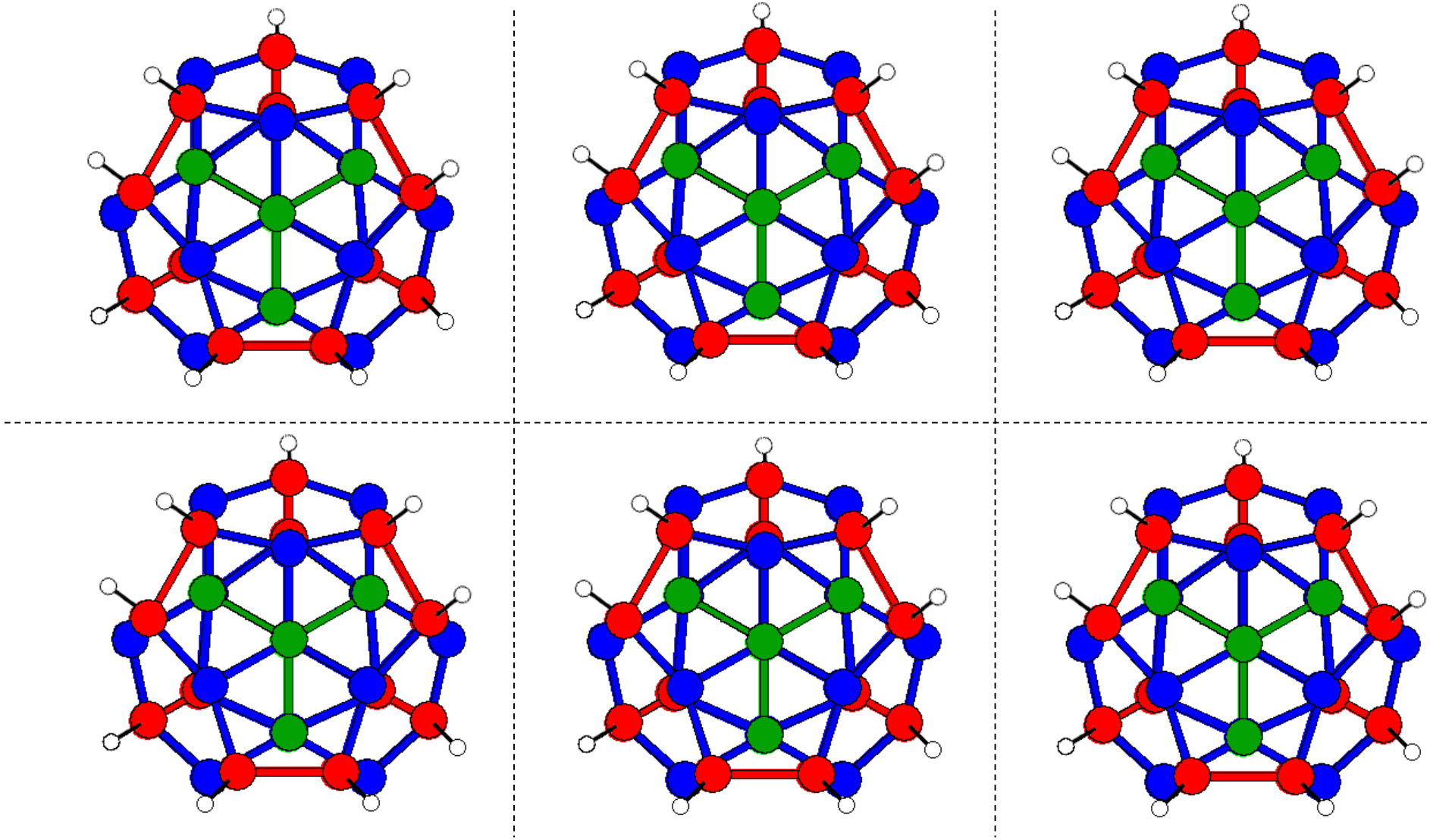

•Symmetrized Plane-wave basis

•The star of G

•$\Psi = \Sigma_s C(G_s)|G_s>$

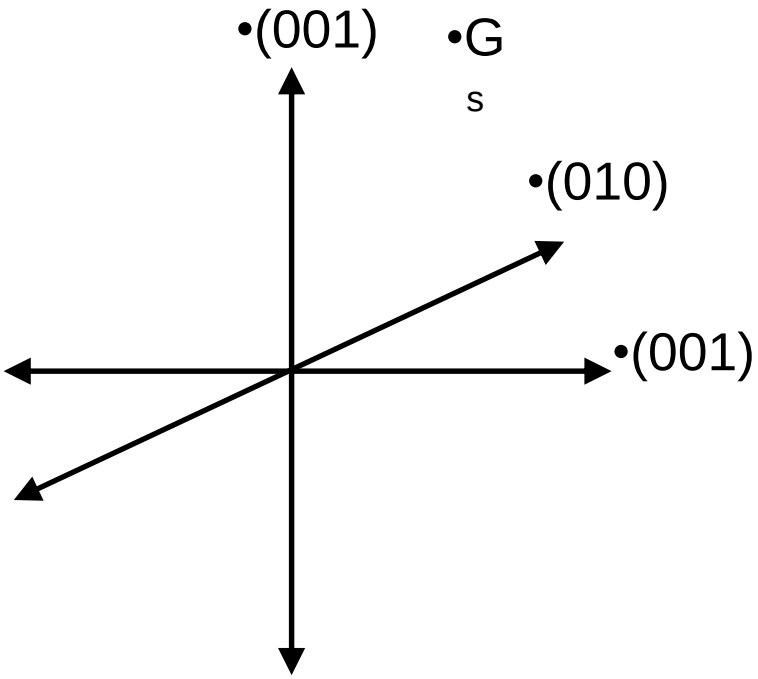

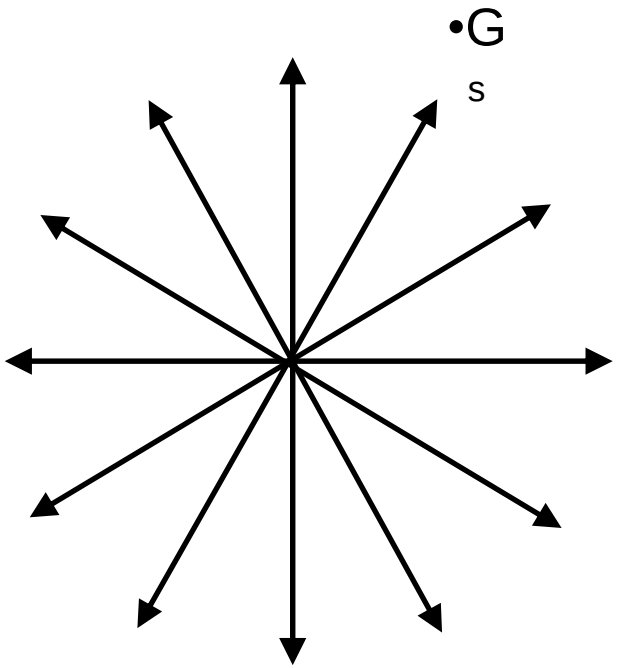

SiH_4

1) Comparison of our result to publication

	HOMO	LUMO	$E_{Singlet}$	$E_{Triplet}$
LDA	-8.0	-0.1	7.9	7.9
HFA	-12.9	1.5	8.3	6.9
GW-BSE (diag. Σ)	-12.1	1.3	8.4	7.1
LDA[3]	-8.4	-0.6	7.8	7.8
HFA[3]	-13.0	1.5	8.8	7.3
DMC[b)]			9.2	
GW-BSE (diag. Σ)[3]	-12.7	1.1	8.5	7.1
Exp[5]			8.8	

2) The HFA calculation shows our successful inclusion of long-range tail in self-energy.

3) Our converged planewave calculation gives right screening on electron and exciton screening.

1nm SiH clusters

Table 2: Energies of $Si_{29}H_{24}$ and $Si_{29}H_{36}$

	HOMO	LUMO	E_{QP}	$E_{Singlet}$	$E_{Triplet}$
LDA($Si_{29}H_{24}$)	-0.8	1.7	2.5		
HFA	-3.3	5.6	8.9	5.0	4.8
GW-BSE	-2.3	4.7	7.0	3.3	3.2
LDA($Si_{29}H_{36}$)	-0.8	2.5	3.3		
HFA	-3.6	6.6	10.2	6.2	5.9
GW-BSE	-2.0	5.4	7.4	4.9	4.7

- The $Si_{29}H_{24}$ has the 3.3eV peak as observed in experiment.
- The first excitation of $Si_{29}H_{36}$ is 4.9eV.
- Extra peaks can be found at 4.5eV and 5.3eV, which is corresponding to the Monte Carlo 4.8eV and 5.5eV.

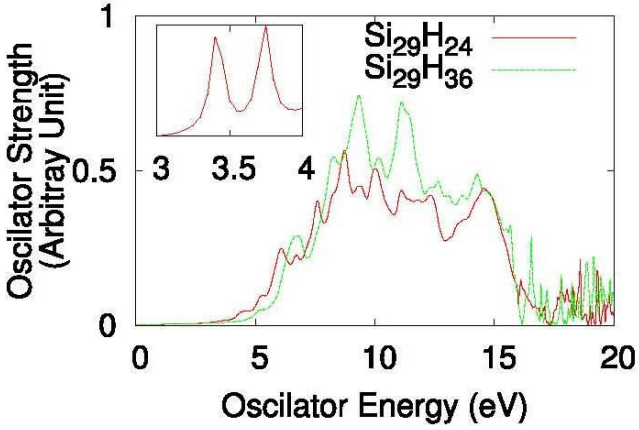

The meta-Generalized Gradient Approximation

mGGA (TB09) [F. Tran and P. Blaha, Phys. Rev. Lett. 102, 226401 (2009)]

In TB09, the exchange-correlation energy is

$$E_{XC}(\mathbf{r}) = \int \epsilon_{XC}[n(\mathbf{r}), \nabla n(\mathbf{r}), \tau(\mathbf{r})]\,,$$

$$v_{x,\sigma}^{TB}(\mathbf{r}) = c v_{x,\sigma}^{BR}(\mathbf{r}) + (3c-2)\frac{1}{\pi}\sqrt{\frac{5}{12}}\sqrt{\frac{\tau_\sigma(\mathbf{r})}{n_\sigma(\mathbf{r})}}\,, \qquad \tau_\sigma(\mathbf{r}) = \sum_{i,\sigma}^{occp.} |\nabla\psi_{i,\sigma}(\mathbf{r})|^2\,,$$

$$v_{x,\sigma}^{BR}(\mathbf{r}) = -\frac{1}{b_\sigma(\mathbf{r})}\left[1 - e^{x_\sigma(\mathbf{r})} - \frac{1}{2}x_\sigma(\mathbf{r})e^{x_\sigma(\mathbf{r})}\right]\,,$$ Becke-Roussel exchange potential

[A.D. Becke & M.R. Roussel, Phys. Rev. A 39, 3761 (1989)]

TDDFT with mGGA :

$$v_{xc}(\mathbf{r}) = \frac{\partial\epsilon_{xc}}{\partial n}(\mathbf{r}) - \nabla\frac{\partial\epsilon_{xc}}{\partial\nabla n}(\mathbf{r}) + \int\frac{\partial\epsilon_{xc}}{\partial\tau}(\mathbf{r}')\frac{\delta\tau(\mathbf{r}')}{\delta n(\mathbf{r})}d\mathbf{r}',$$

$$f_{\mathbf{G},\mathbf{G}'}^{xc} \approx -\overline{\frac{\partial\epsilon_{xc}}{\partial\tau}}\chi_{KS,s}^{-1}(\mathbf{G},\mathbf{G}')\,,$$ [V.U. Nazarov & G. Vignale, PRL 107, 216402(2011)]

$$\chi_{KS}(\mathbf{r},\mathbf{r}') = \sum_{\alpha,\beta,\sigma}\frac{f_\alpha - f_\beta}{\omega - \epsilon_\beta + \epsilon_\alpha + i\eta}\psi_{\alpha,\sigma}^*(\mathbf{r})\psi_{\beta,\sigma}(\mathbf{r})\psi_{\beta,\sigma}^*(\mathbf{r}')\psi_{\alpha,\sigma}(\mathbf{r}')$$

Band structure comparison

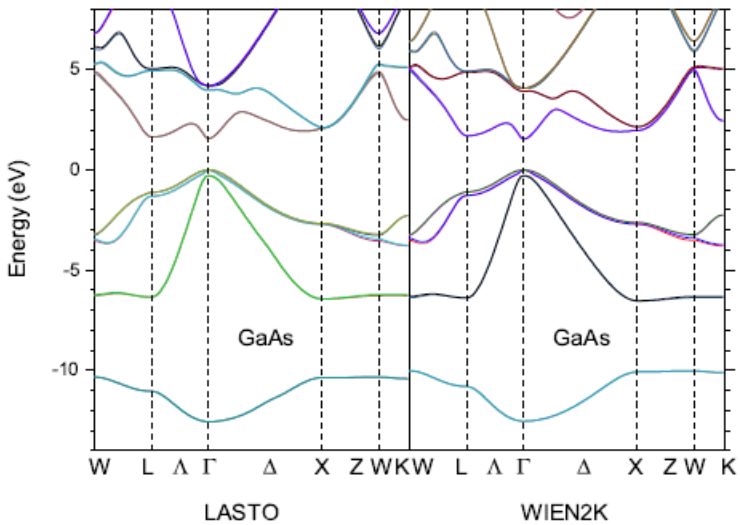

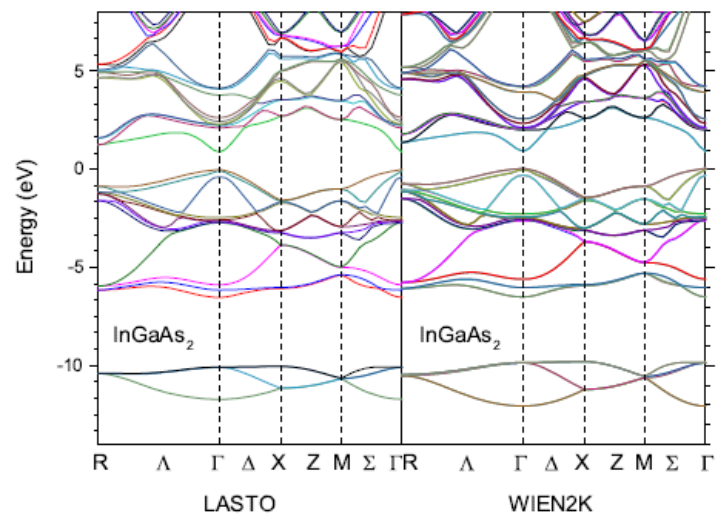

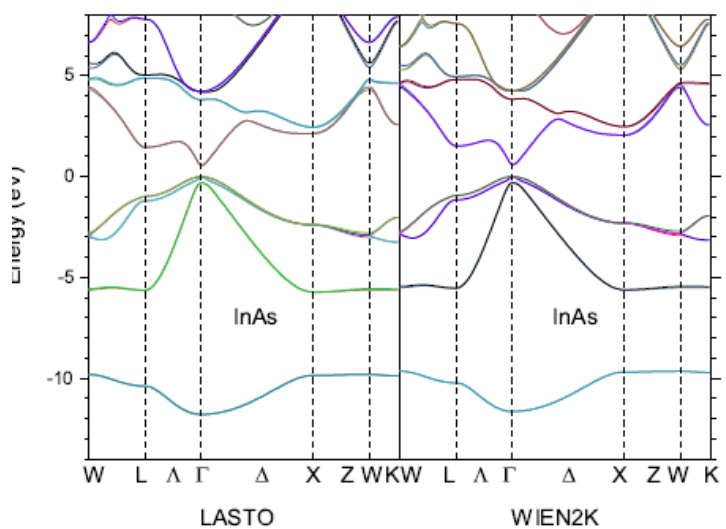

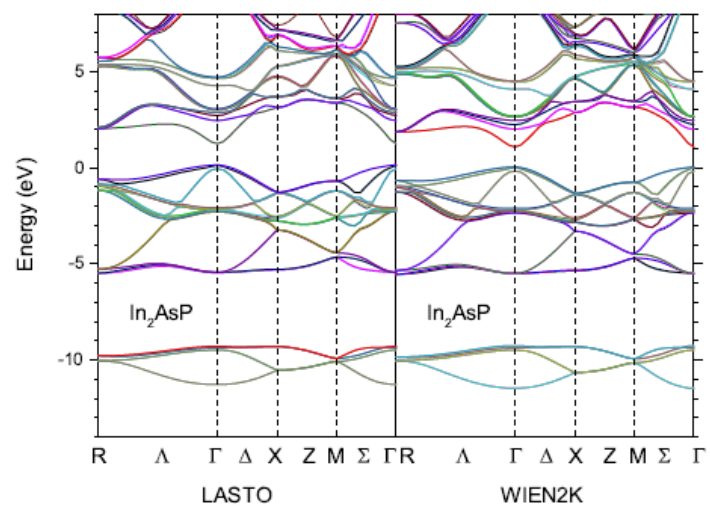

Comparison between LASTO & WIEN2k

$|\nabla n|$

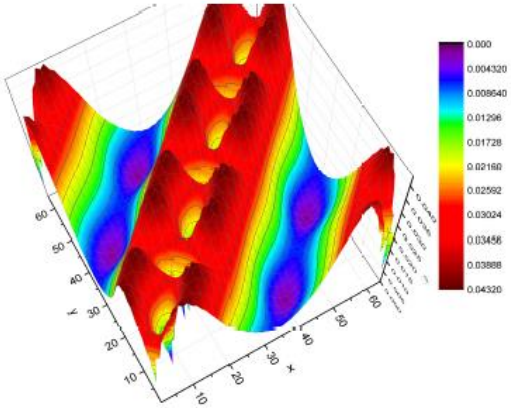

(a) Computed by LASTO

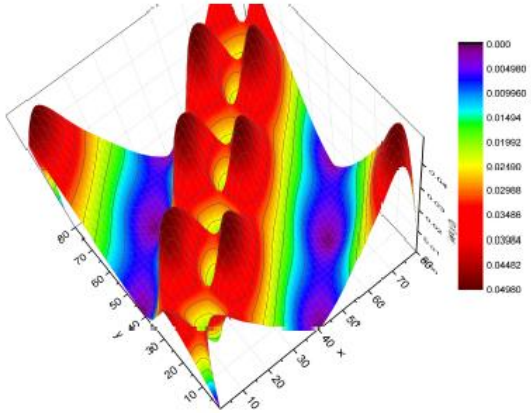

(b) Computed by WIEN2K

$\nabla^2\psi$

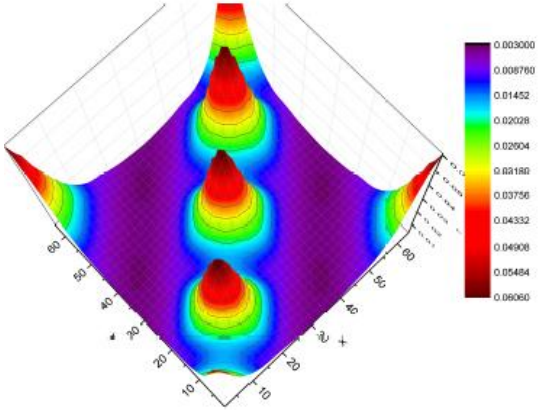

(a) Computed by LASTO

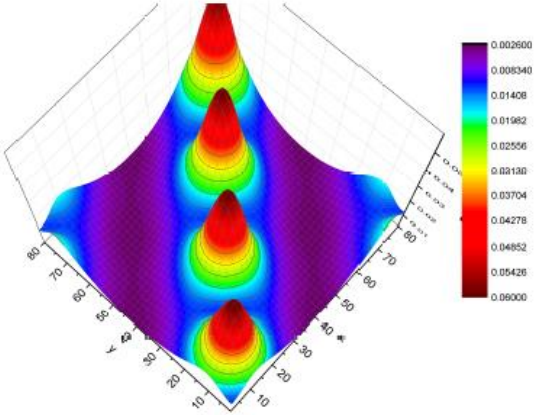

(b) Computed by WIEN2K

Figure 4.10: Plot the kinetic energy density of Si in the interstitial region

Excitation spectra

Si

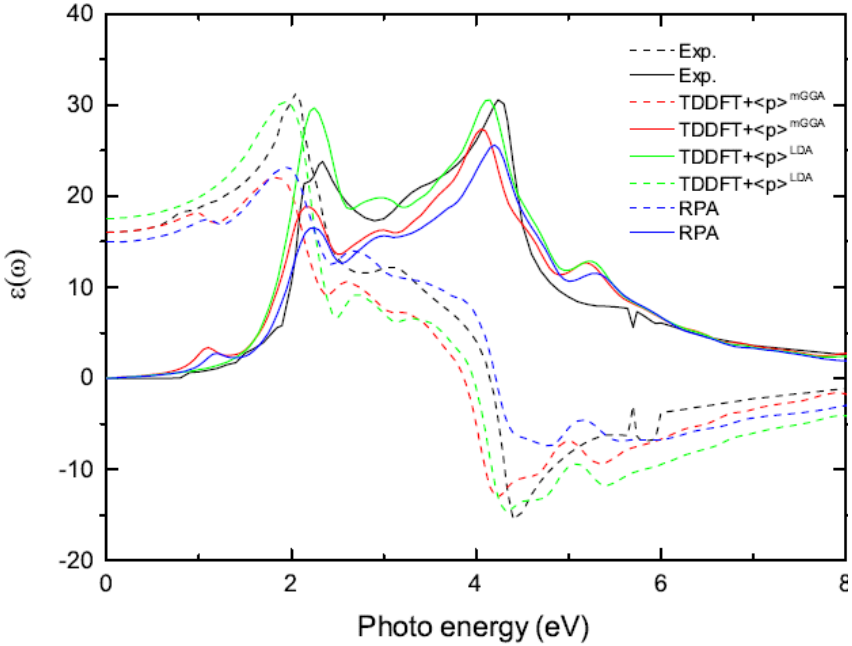

GaAs

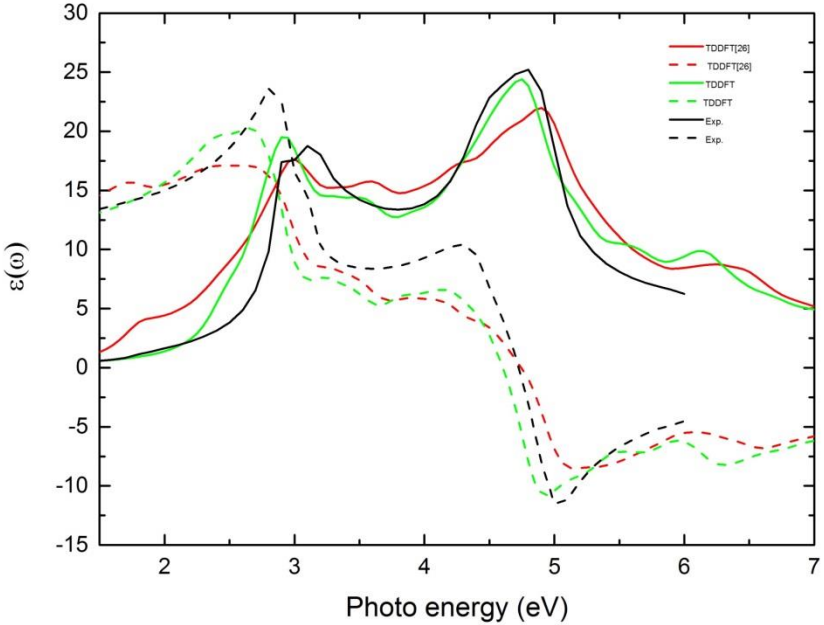

Dielectric functions of InGaAs & InAsP alloys obtained by TDDFT based on mGGA

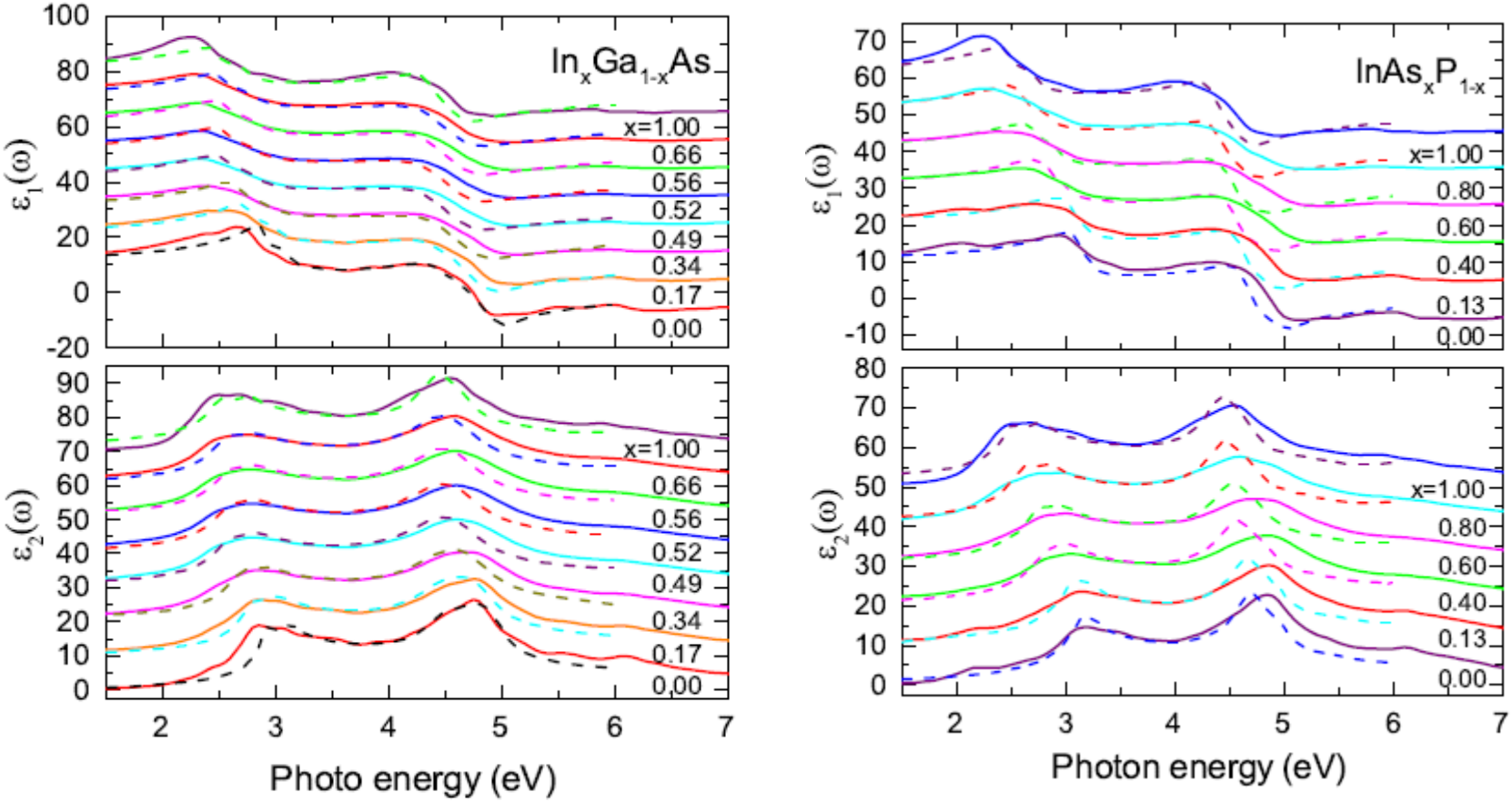

[F. Tran and P. Blaha, PRL 102, 226401 (2009)]

[V.U. Nazarov and G. Vignale, PRL **107**, 216402(2011)]

Bond-orbital model

[S. Sun,Y. C. Chang, PRB 62, 13631 (2000)]

$$H_{\alpha,\alpha'}(k) = E_p \delta_{\alpha,\alpha'} + \sum_{\tau} e^{ik\cdot\tau} \left\{ E_{xy}\tau_\alpha \tau_{\alpha'} + \left[\left(E_{xx} - E_{xy} \right) \tau_\alpha^2 + E_{zz}\left(1 - \tau_\alpha^2\right) \right] \delta_{\alpha,\alpha} \right.$$

Strain Hamiltonian

$$H_{st} = \begin{pmatrix} -\Delta V_H + D_1 & \sqrt{3}de_{xy} & \sqrt{3}de_{xz} \\ \sqrt{3}de_{xy} & -\Delta V_H + D_2 & \sqrt{3}de_{yz} \\ \sqrt{3}de_{xz} & \sqrt{3}de_{yz} & -\Delta V_H + D_3 \end{pmatrix}$$

$e_{ij}=(\varepsilon_{ij}+\varepsilon_{ji})/2$

$\Delta V_H=(a_1+a_2)(\varepsilon_{xx}+\varepsilon_{yy}+\varepsilon_{zz})$

$D_1=b(2\varepsilon_{xx}-\varepsilon_{yy}-\varepsilon_{zz})$

$D_2=b(2\varepsilon_{yy}-\varepsilon_{xx}-\varepsilon_{zz})$

$D_3=b(2\varepsilon_{zz}-\varepsilon_{xx}-\varepsilon_{yy})$

a_1, a_2, b, d = deformation potentials.

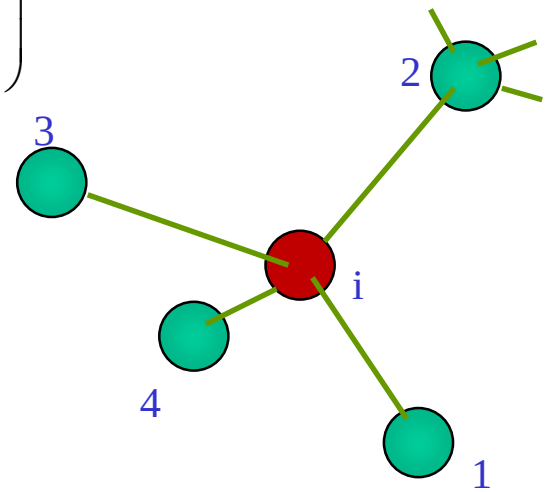

InAs/GaAs Self assembled quantum dots

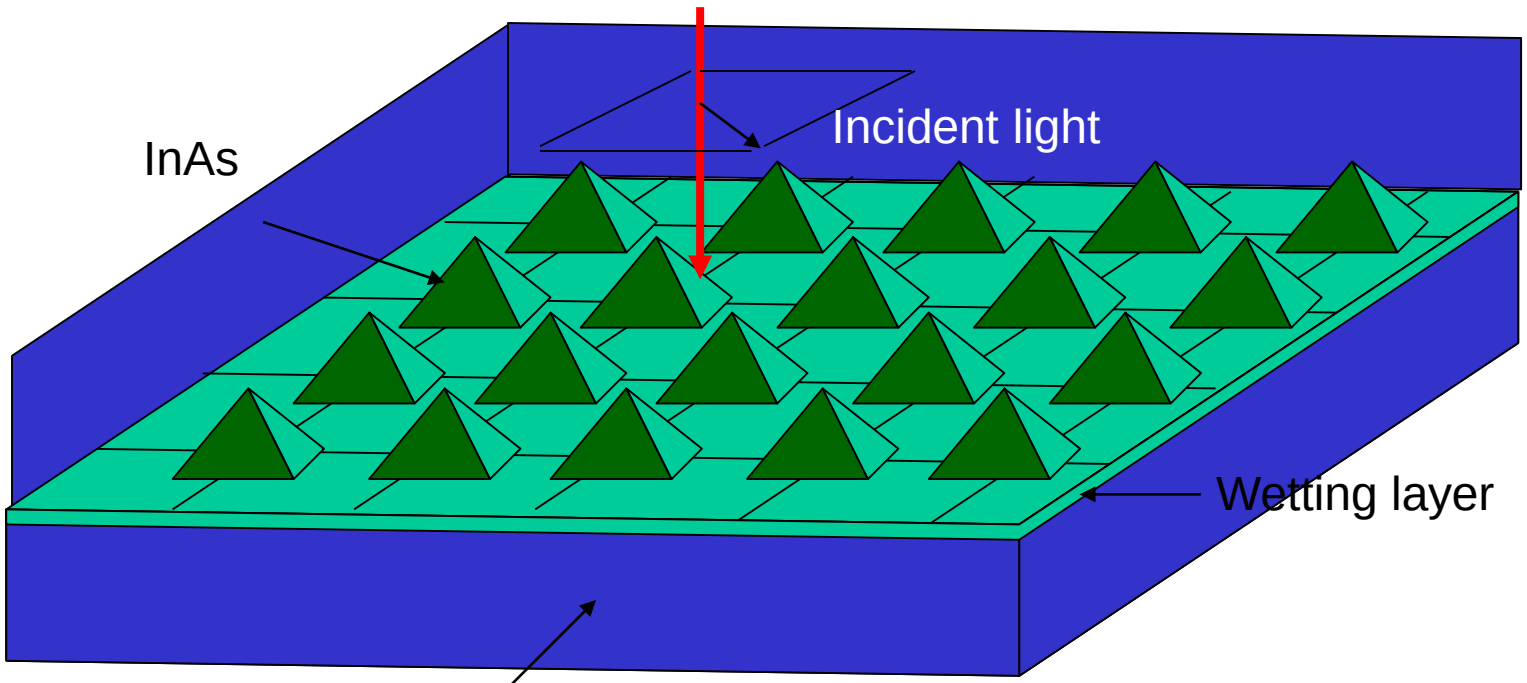

Lattice mismatch 7%

Infrared detector
Laser

Area density

$$10^{11} / cm^2$$

Bond-orbital model

[S. Sun,Y. C. Chang, PRB 62, 13631 (2000)]

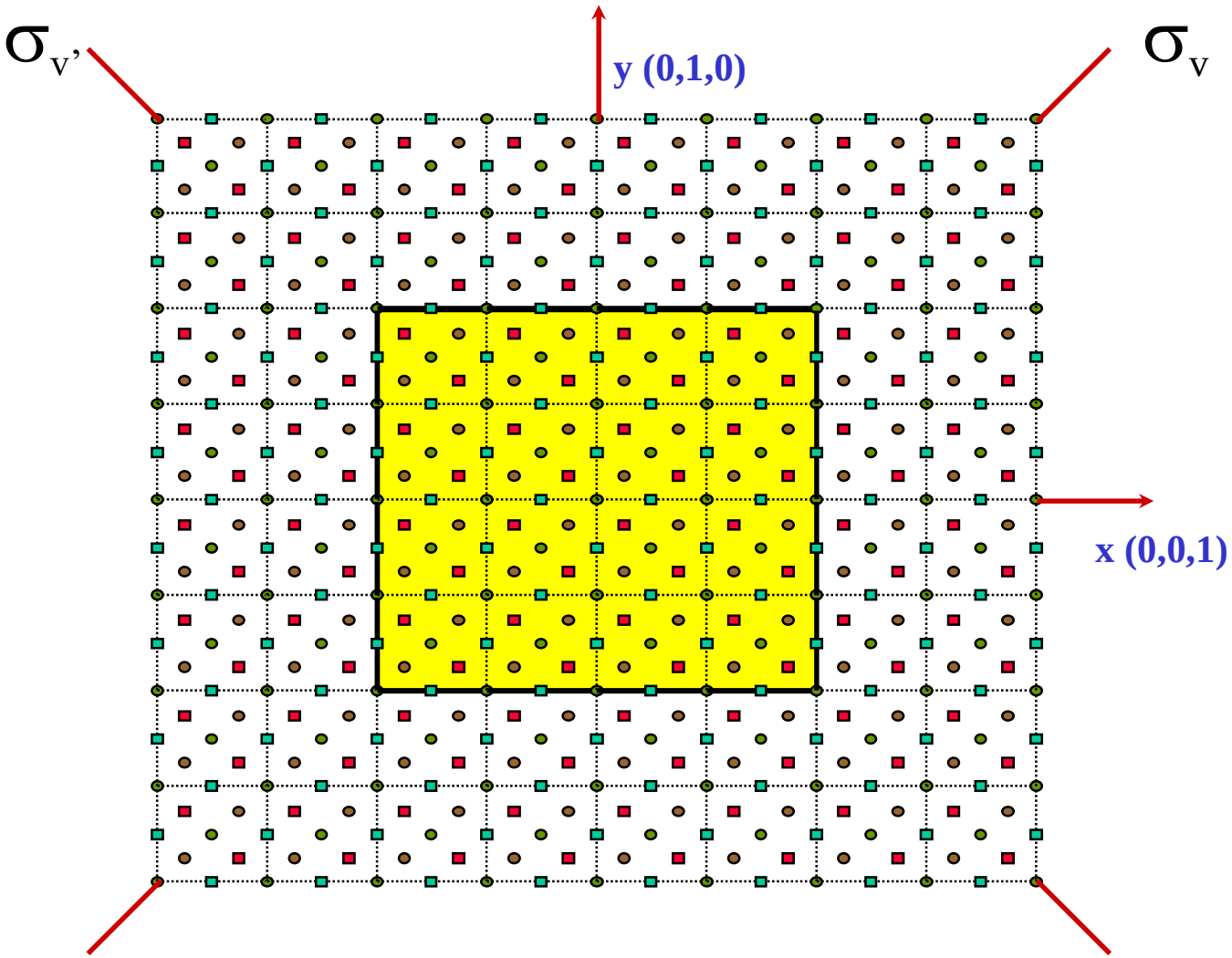

Valence force field (VFF) Model

$$V = \frac{1}{4}\sum_{ij}\frac{3}{4}\alpha_{ij}\left(d_{ij}^2 - d_{0,ij}^2\right)^2 \Big/ d_{0,ij}^2$$

$$+\frac{1}{4}\sum_{i}\sum_{j\neq k}\frac{3}{4}\beta_{ijk}\left(\vec{d}_{ij}\cdot\vec{d}_{ik} + d_{0,ij}d_{0,ik}/3\right)^2 \Big/ d_{0,ij}d_{0,ik}$$

i labels atom positions
j , k label nearest-neighbors of i
d_{ij} = bond length joining sites i and j
$d_{0,ij}$ is the corresponding equilibrium length
α_{ij}= bond stretching constants
d_{ijk}= bond bending constants
We take $d_{ijk}^2 = d_{ij}d_{ik}$

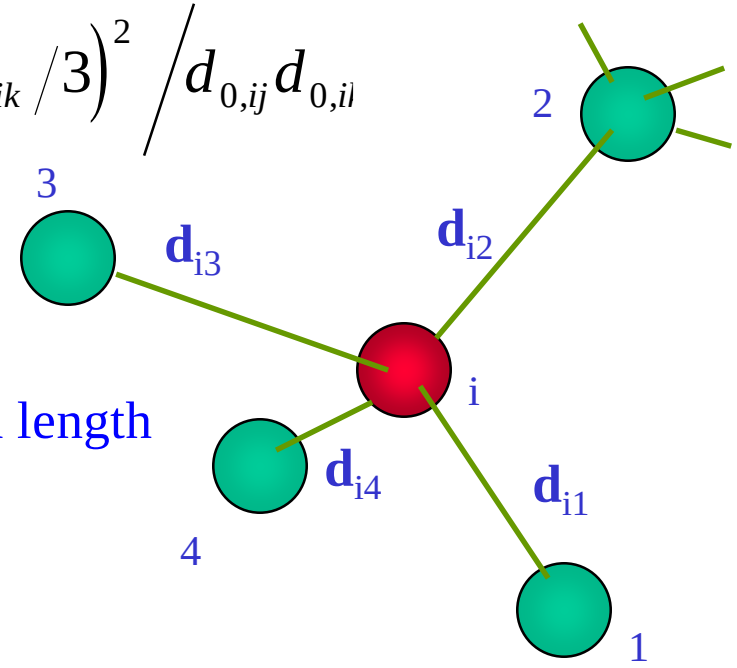

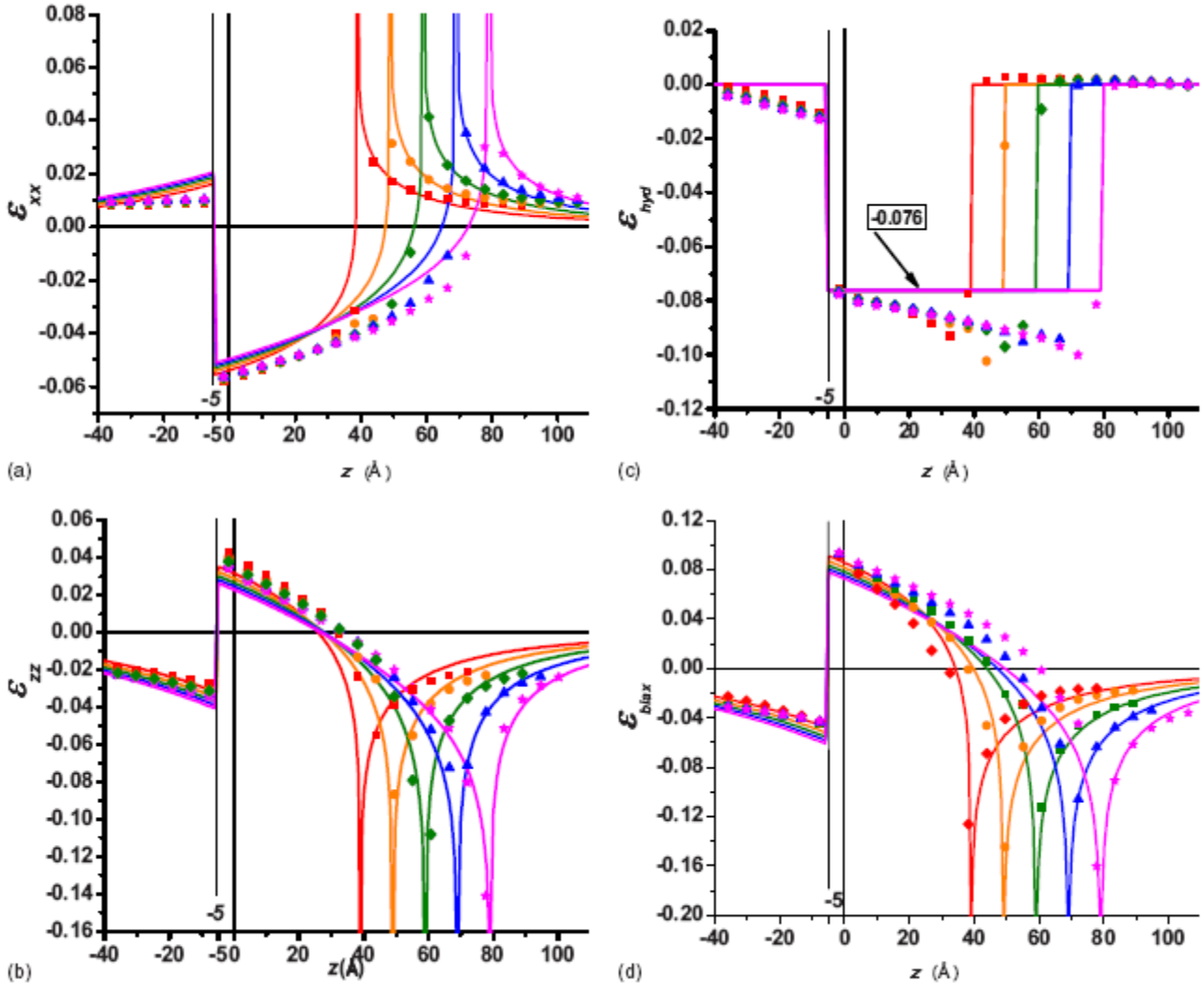

FIG. 3. (Color online) The strains on OZ axes: (a) the radial strain ε_{pp}, (b) the strain ε_{zz}, (c) the hydrostatic ε_{hyd}, and (d) the biaxial strain ε_{biax} on the OZ axis, for the ratios R/H=10/3.9, 10/4.9, 10/5.9, 10/6.9, 10/7.9, with R=100 Å. The dots are for the VFF model and the continuum lines for CM.

Ground Transition Energy Varying With Dot Height (comparing to Experiment)

UNIVERSITY OF ILLINOIS AT URBANA-CHAMPAIGN

Dot base length 200Å

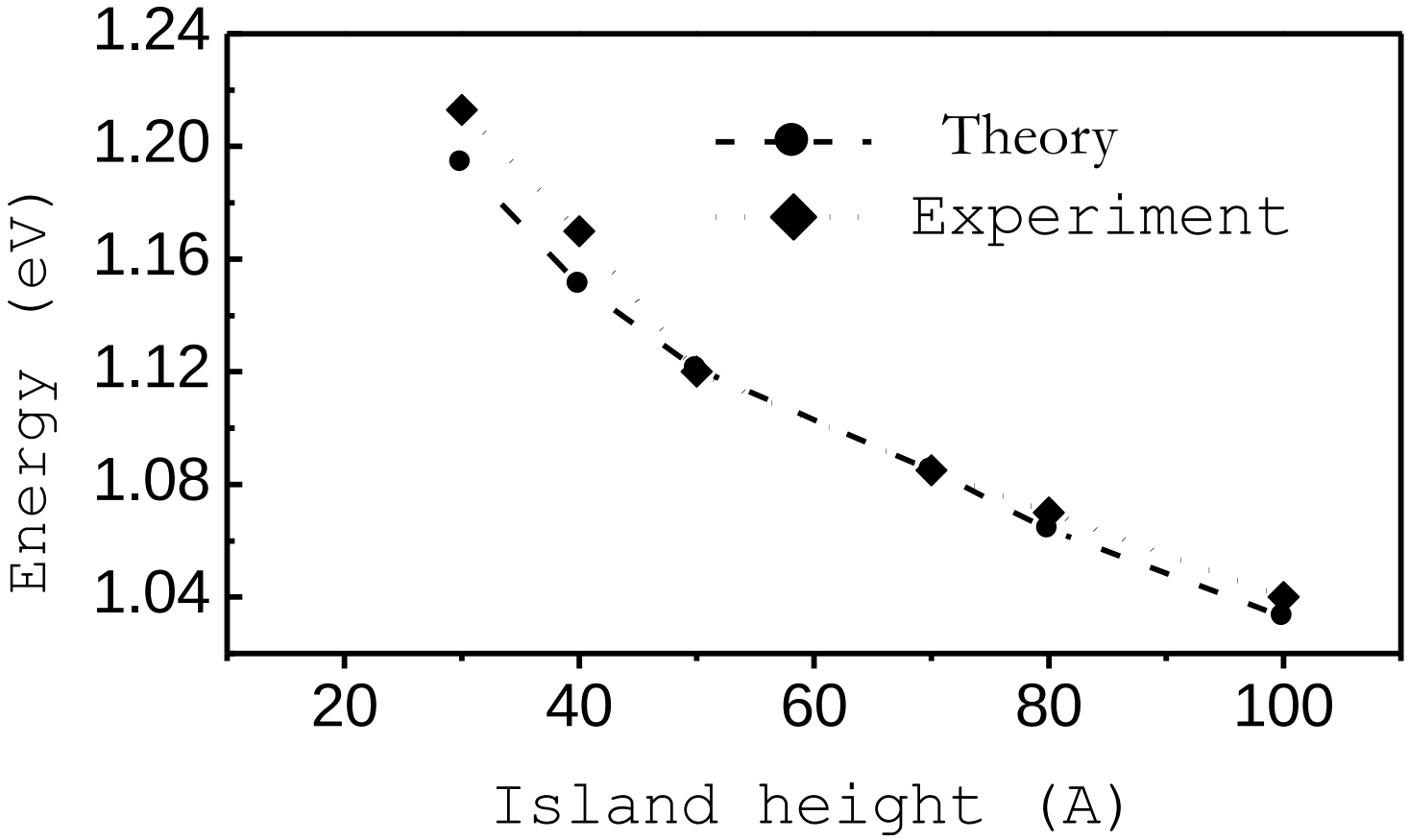

PL/PLE Characterization: Electronic Structure

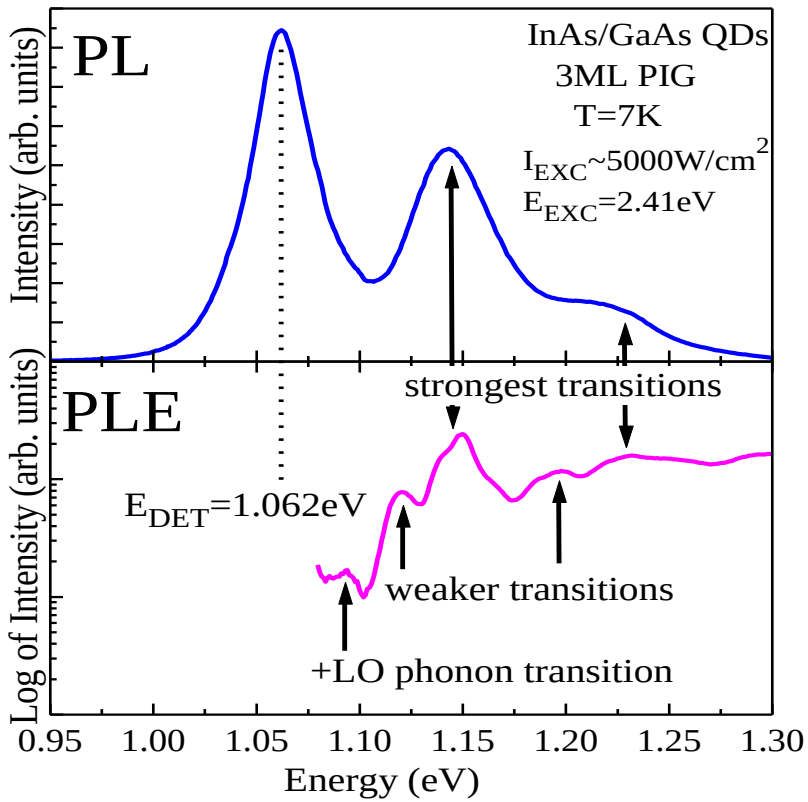

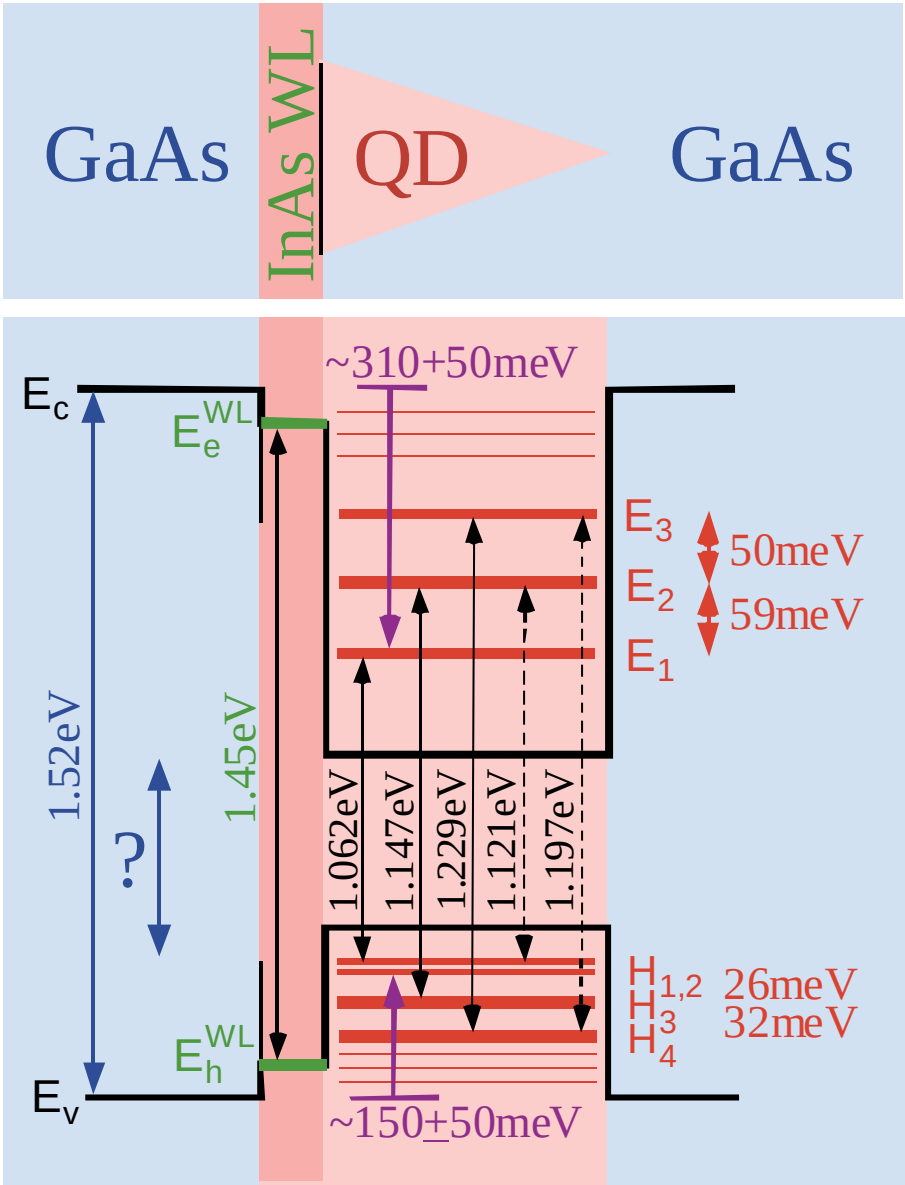

Ground state at 1.062eV

Excited states:

Strongest at 1.147eV and 1.229eV

Weaker at 1.121eV and 1.197eV

[Data from A. Madhkar (USC)]

Intra-band Transitions

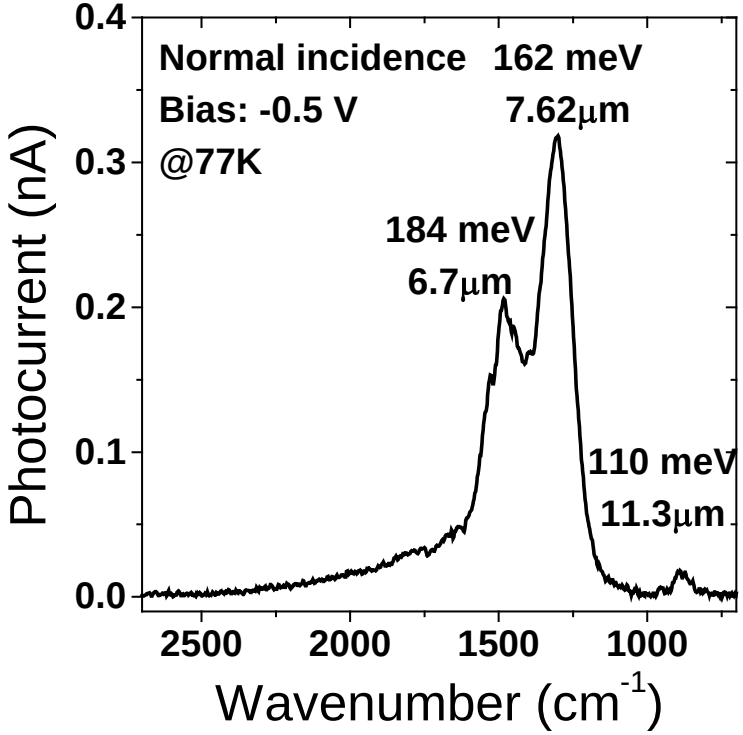

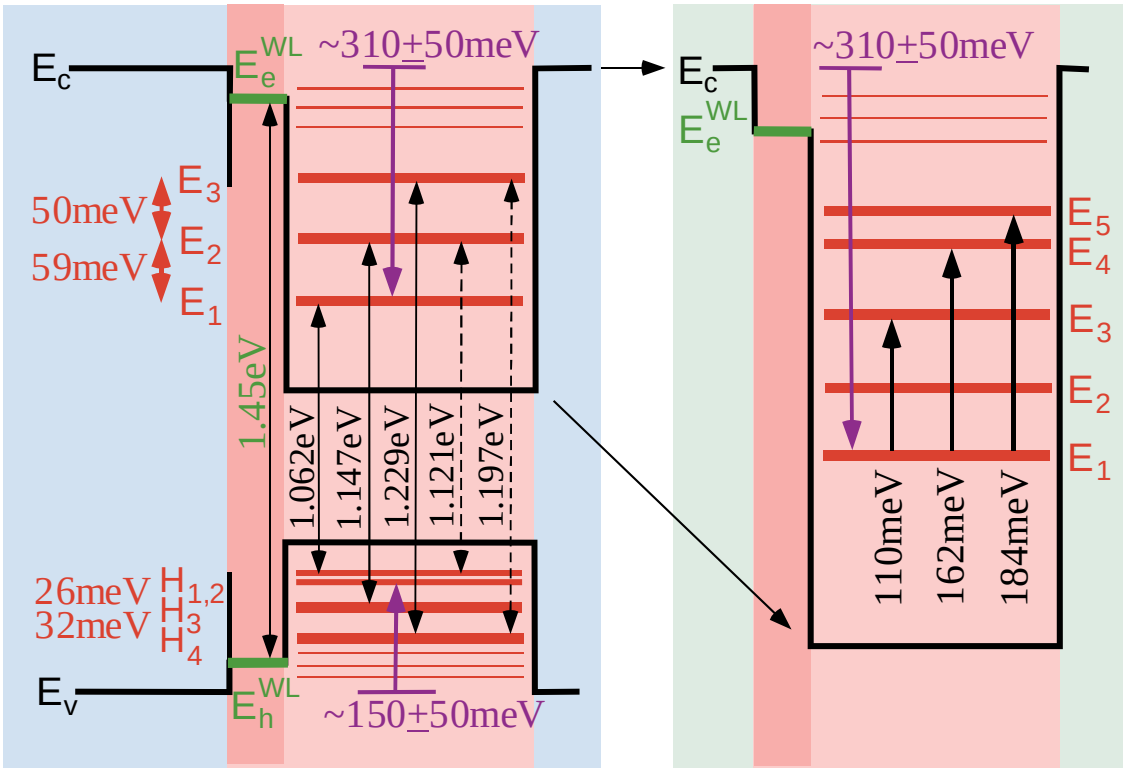

Data from A. Madhkar (USC)

Intra-band Transitions

Table 4 Inter-sub band transition matrix elements of ground electron state to upper three electron states, $\left|\langle \phi_{1,c} | \bar{r} | \phi_{i,c} \rangle\right|^2$. B=200A, h=80A.

Symmetry	state i	x	y	z
A1	#2 (0.111)	0	0	0.2
	#3 (0.123)	0	0	57
	#4 (0.197)	0	0	201
A2	#2 (0.106)	0	0	28.5
	#3 (0.114)	0	0	0
B1,B2	#2 (0.109)	0	0	15
	#3 (0.138)	0	0	42
	#4 (0.201)	0	0	14
A1-B1n	#1 (0.062)	446	446	0
	#2 (0.162)	0.2	0.2	0
	#3 (0.218)	0.4	0.4	0
B1-A1n	#2(0.049)	536	536	0
	#3(0.061)	659	659	0
	#4(0.135)	376	376	0
	#5(0.161)	10.2	10.2	0

Effective bond-orbital model for QWRs

[Y. C. Chang, W. E. Mahmoud, Comp. Phys. Comm., **196,** 92 (2015)]

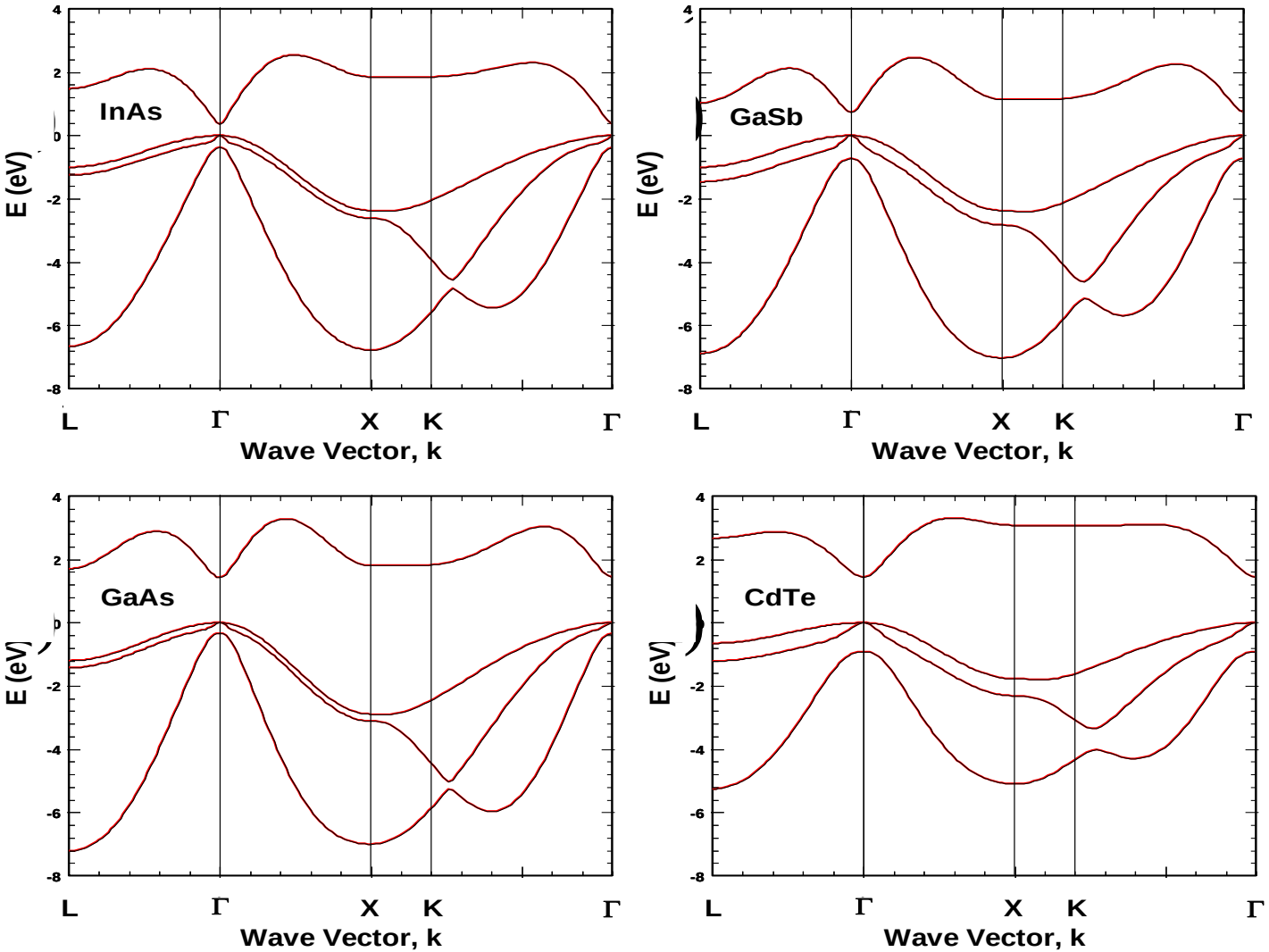

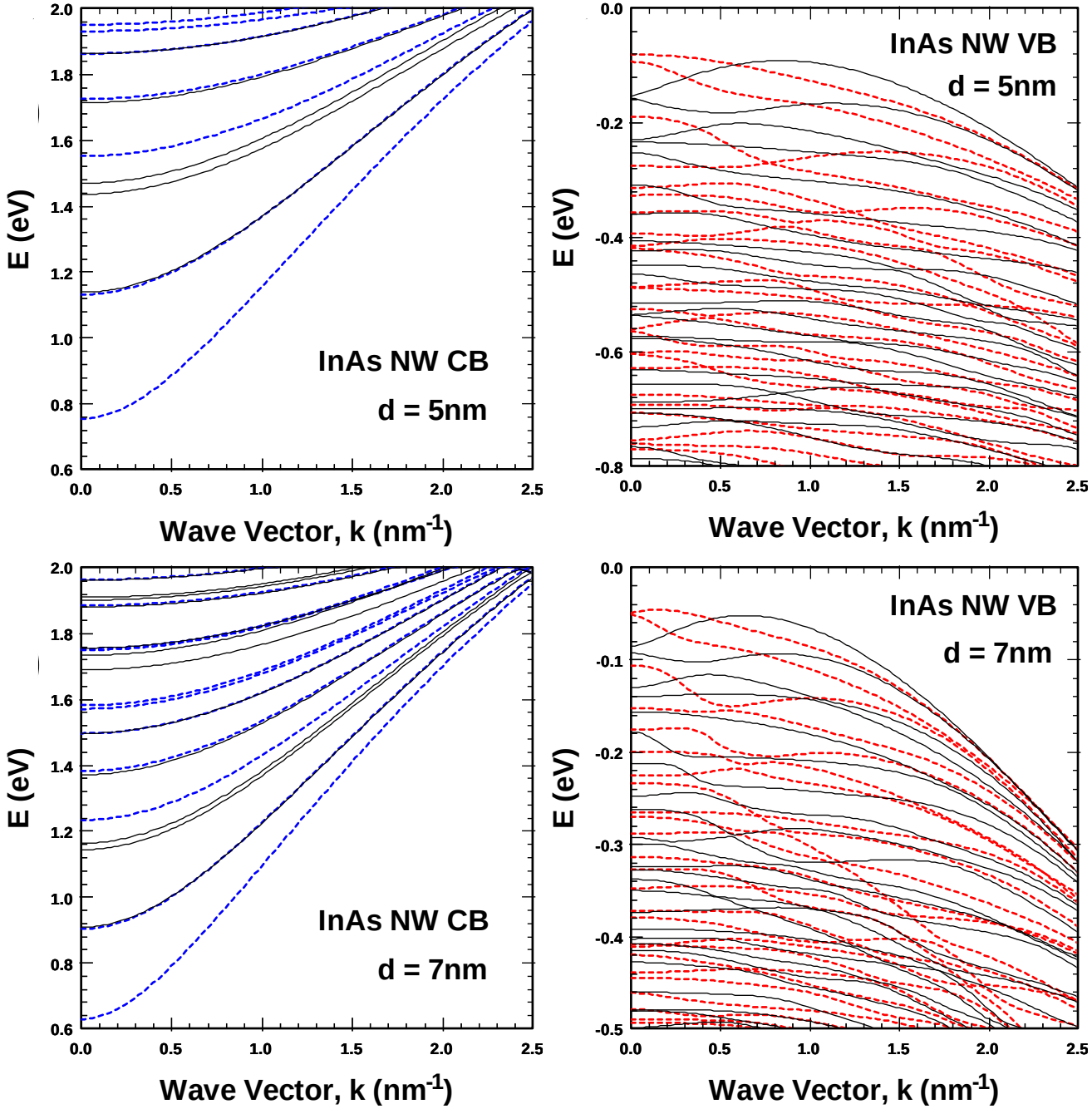
InAs NW CB
d = 5nm
InAs NW VB
d = 5nm
InAs NW CB
d = 7nm
InAs NW VB
d = 7nm
E (eV)
Wave Vector, k (nm-1)

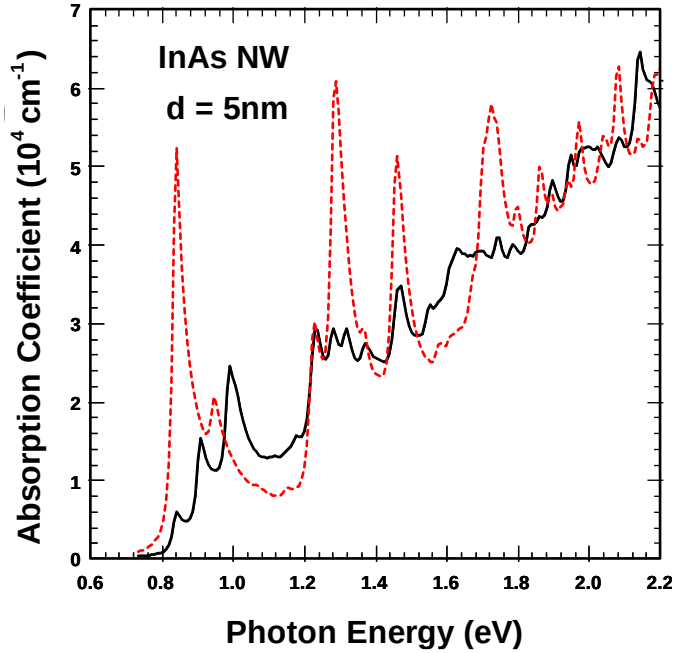
InAs NW
d = 5nm
Absorption Coefficient (10^4 cm^{-1})
Photon Energy (eV)
0
1
2
3
4
5
6
7
0.6
0.8
1.0
1.2
1.4
1.6
1.8
2.0
2.2

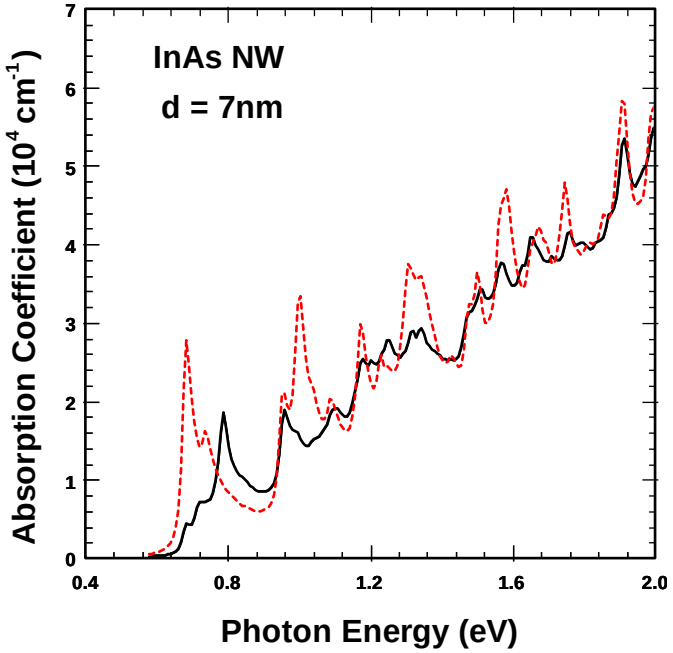
InAs NW
d = 7nm
Absorption Coefficient (10^4 cm^{-1})
Photon Energy (eV)
0
1
2
3
4
5
6
7
0.4
0.8
1.2
1.6
2.0

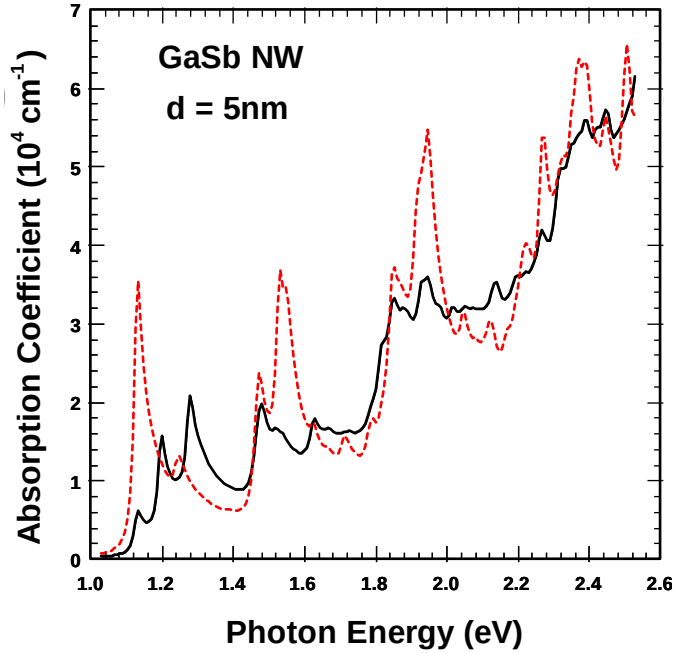
GaSb NW
d = 5nm
Absorption Coefficient (10^4 cm^{-1})
Photon Energy (eV)
0
1
2
3
4
5
6
7
1.0
1.2
1.4
1.6
1.8
2.0
2.2
2.4
2.6

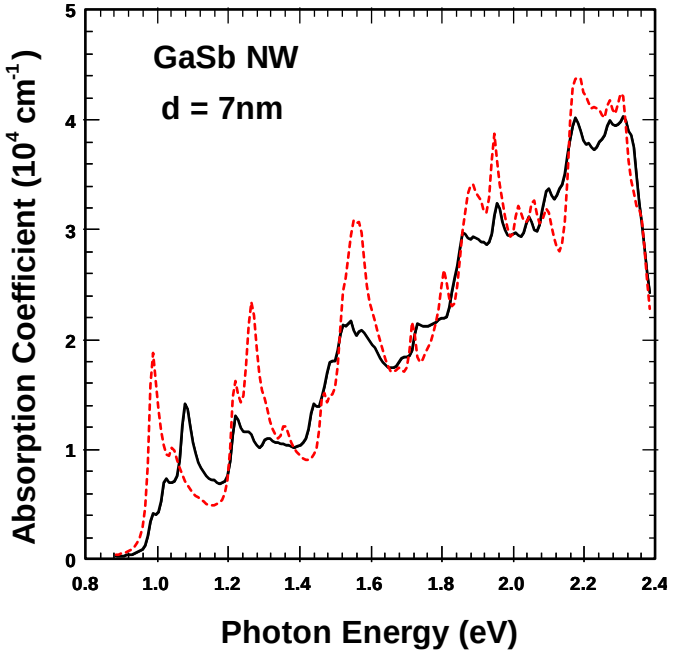
GaSb NW
d = 7nm
Absorption Coefficient (10^4 cm^{-1})
Photon Energy (eV)
0
1
2
3
4
5
0.8
1.0
1.2
1.4
1.6
1.8
2.0
2.2
2.4

Excitation spectra of colloidal QDs

[8-band or (6+2)-band **k.p** model]

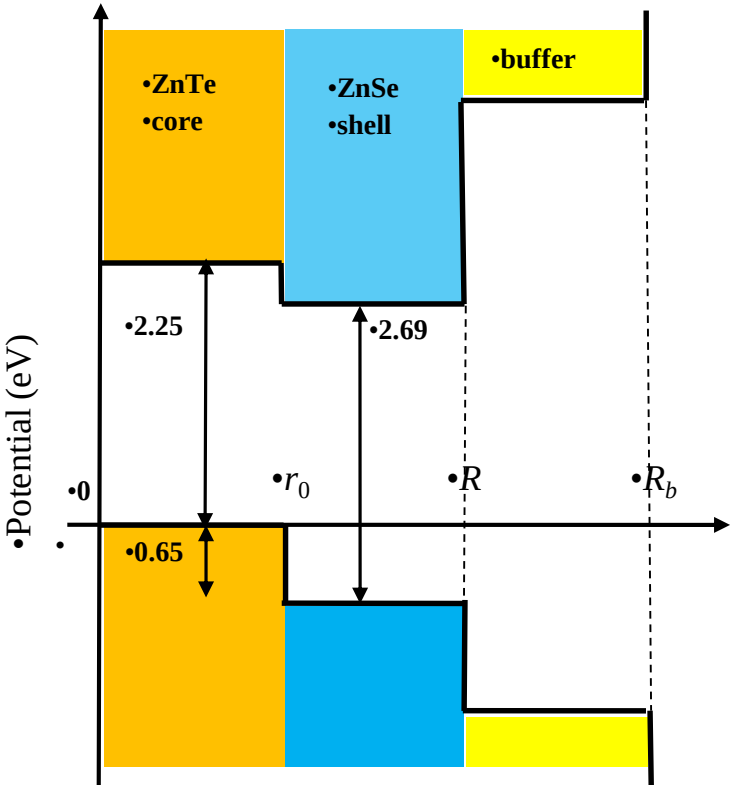

•**Figure 1.** Schematic bulk band-offset for

•ZnTe/ZnSe CSQD.

•

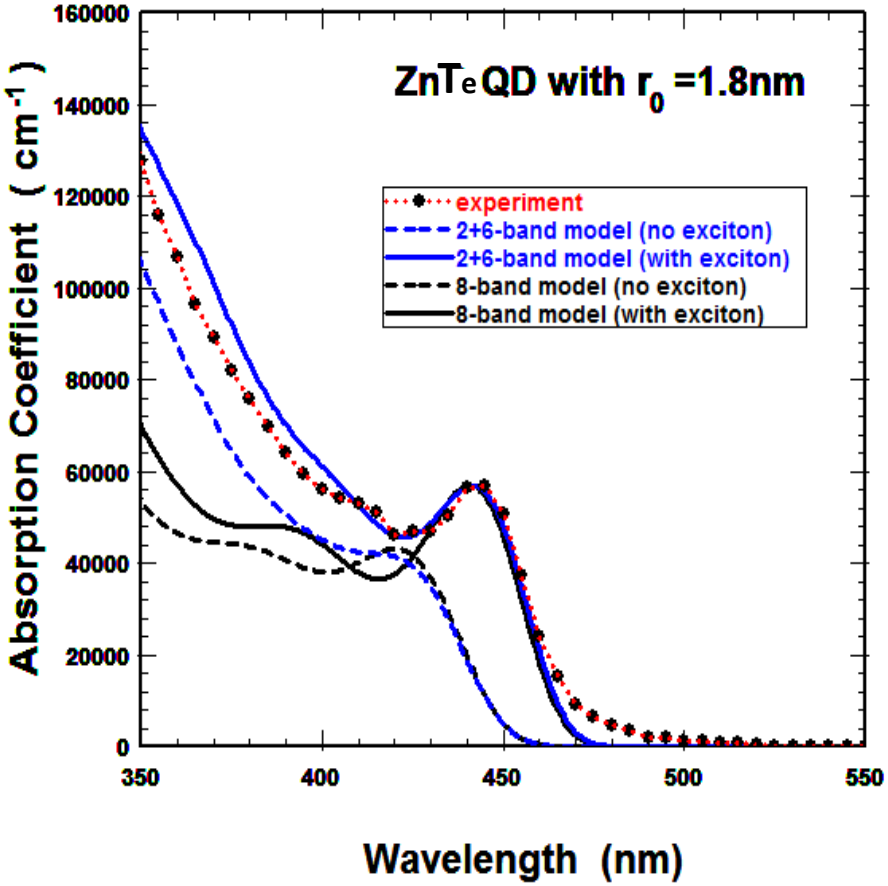

[Exp. data from S.M. Fairclough et al., J. Phys. Chem. C **116**, 26898 (2012)]

Absorption coefficient for ZnTe/ZnSe CSQDs

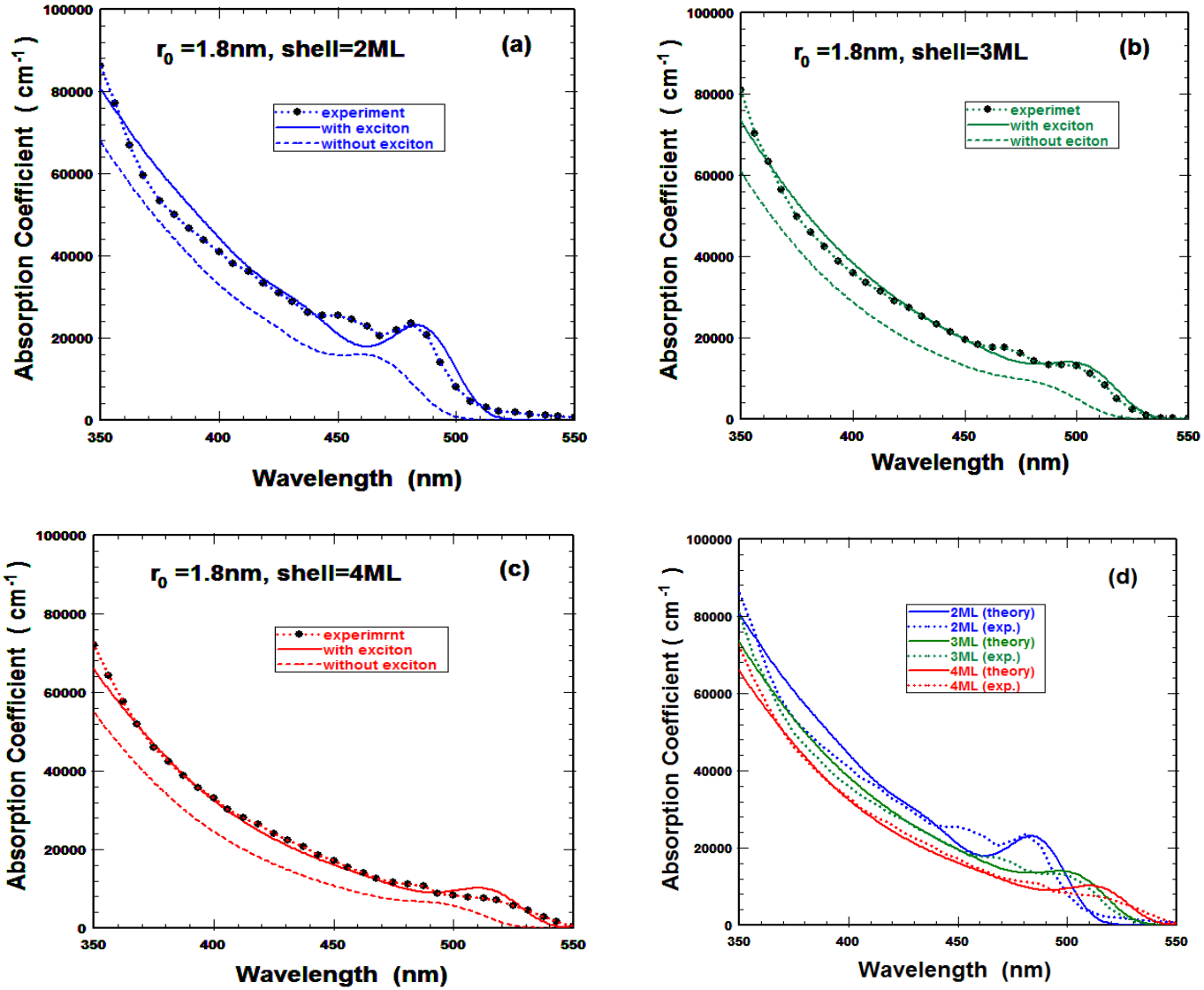

Transport through nanostructure junctions

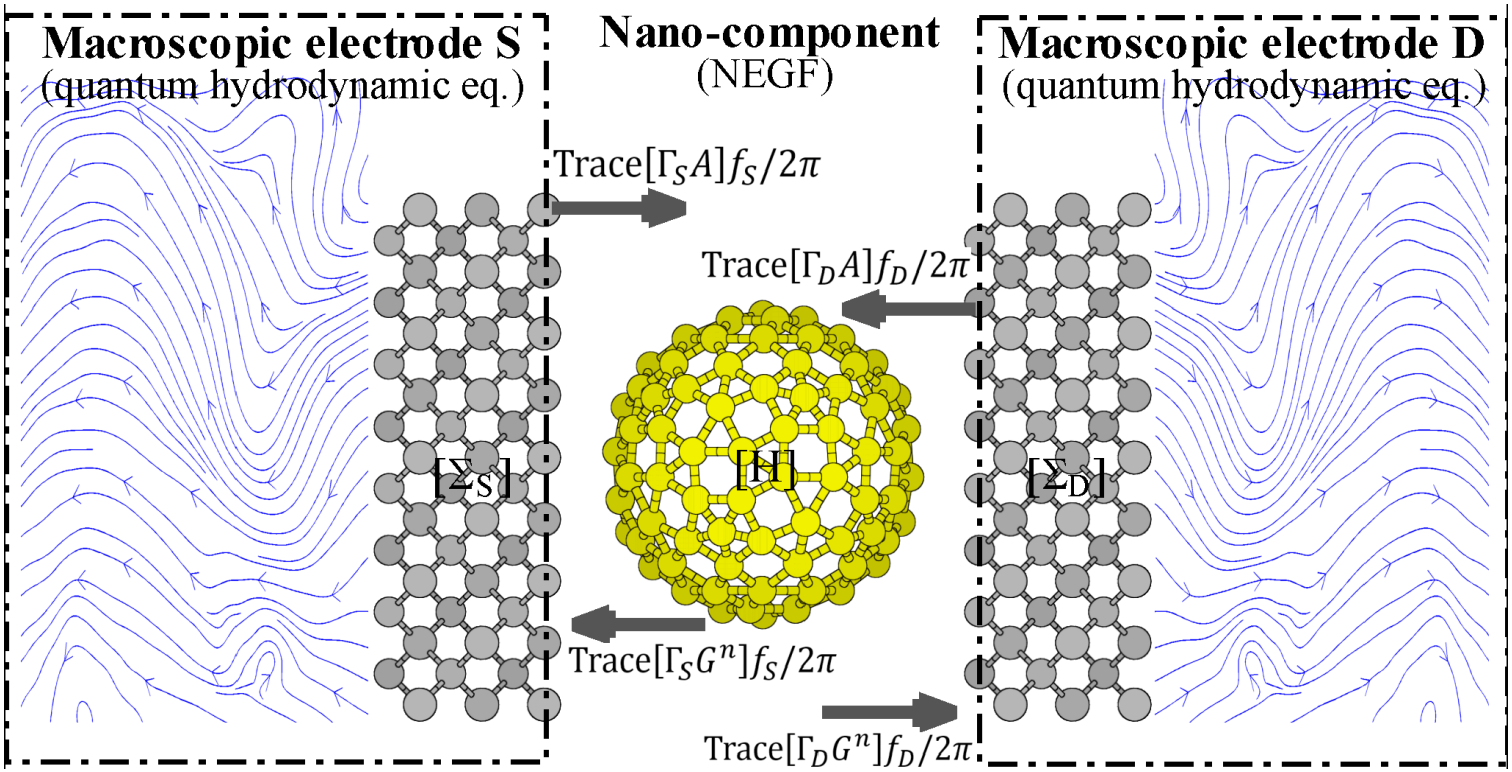

Green function approach for GMR

[J. Velev and Y.-C. Chang, Phys. Rev. B **63**, 184411 (2001)]

A. Fert & P. Grunberg
2007 Nobel Prize (GMR)

$$\begin{bmatrix} \mathbf{H}_{L,0} & \mathbf{V}_{LS} & 0 & 0 & 0 & 0 \\ \mathbf{V}_{LS}^{\dagger} & \mathbf{H}_{S,1} & \mathbf{V}_{SS,12} & 0 & \dots & 0 \\ 0 & \mathbf{V}_{SS,12}^{\dagger} & \mathbf{H}_{S,2} & \mathbf{V}_{SS,23} & 0 & 0 \\ 0 & 0 & \mathbf{V}_{SS,23}^{\dagger} & \mathbf{H}_{S,3} & \mathbf{V}_{SS,34} & 0 \\ 0 & \dots & 0 & \mathbf{V}_{SS,34}^{\dagger} & \dots & \mathbf{V}_{SR} \\ 0 & 0 & 0 & 0 & \mathbf{V}_{SR}^{\dagger} & \mathbf{H}_{R,m+1} \end{bmatrix}$$

$$\mathbf{G}_{\mathbf{L}}^{0} = (E\mathbf{O}_L - \mathbf{H}_L + i\eta)^{-1}$$

$$\mathbf{G}_{\mathbf{R}}^{0} = (E\mathbf{O}_R - \mathbf{H}_R + i\eta)^{-1}$$

$$\mathbf{G}_S = [E\mathbf{O}_S - \mathbf{H}_S - \mathbf{\Sigma}_L(E) - \mathbf{\Sigma}_R(E)]^{-1},$$

$$\mathbf{\Sigma}_L = (\mathbf{V}_{SL} - E\mathbf{O}_{SL})\,\mathbf{G}_{\mathbf{L}}^{0}\,(\mathbf{V}_{LS} - E\mathbf{O}_{LS})$$

$$\mathbf{\Sigma}_R = (\mathbf{V}_{SR} - E\mathbf{O}_{SR})\,\mathbf{G}_{\mathbf{R}}^{0}\,(\mathbf{V}_{RS} - E\mathbf{O}_{RS})$$

$Fe_4/Cr_3/Fe_4$

trilayer junction

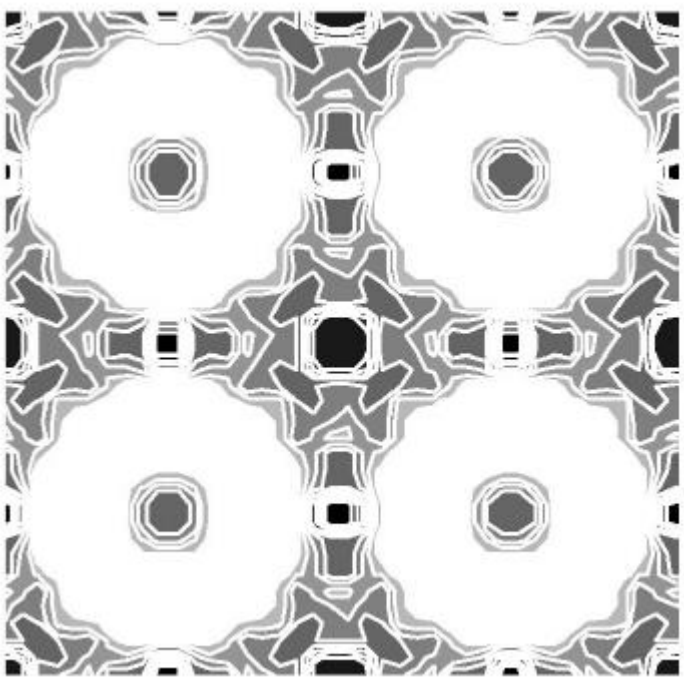

$(Fe_2/Cr_M/Fe_2)_N$

multiilayer junction

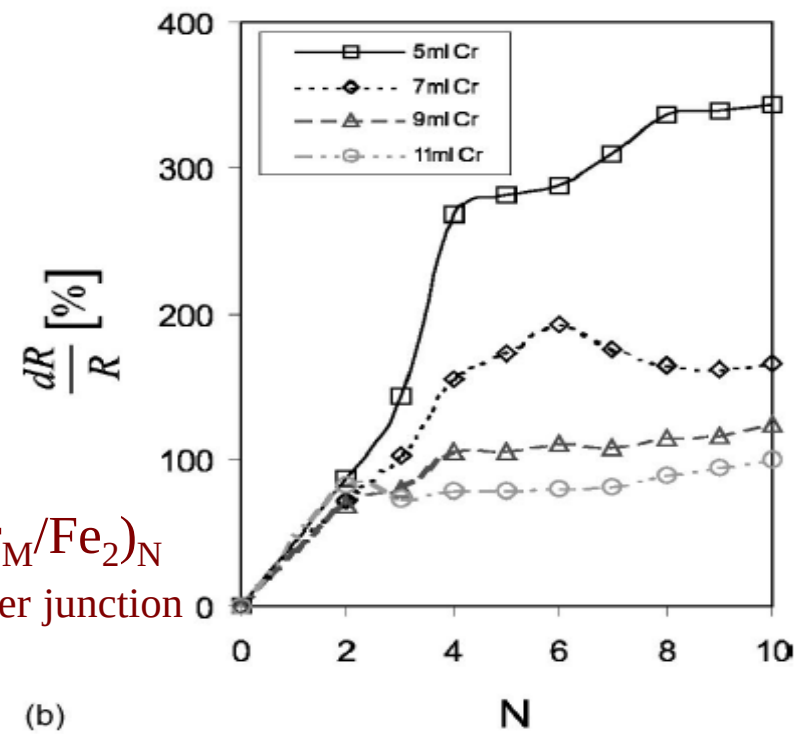

DFT to Tight-binding conversion

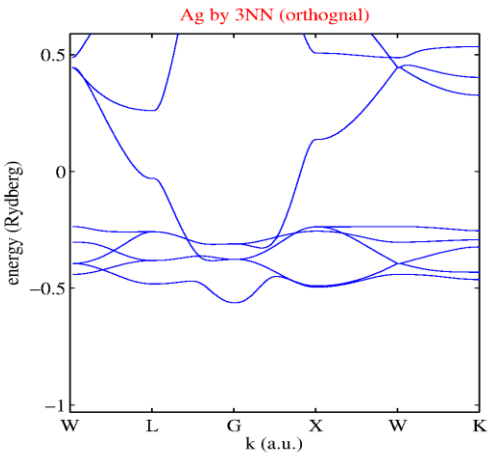

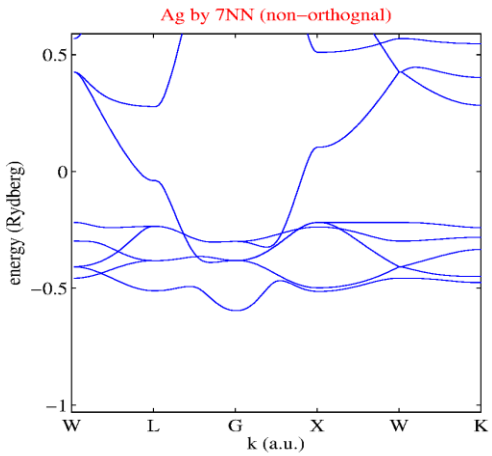

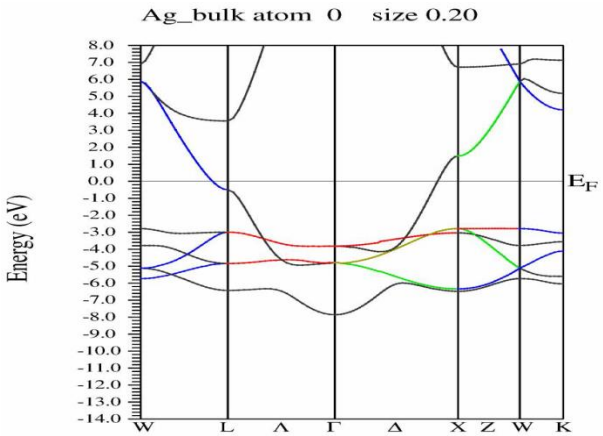

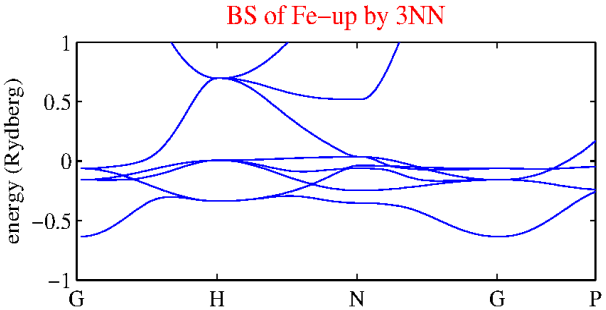

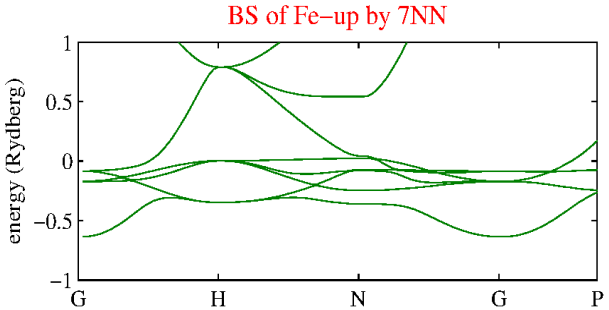

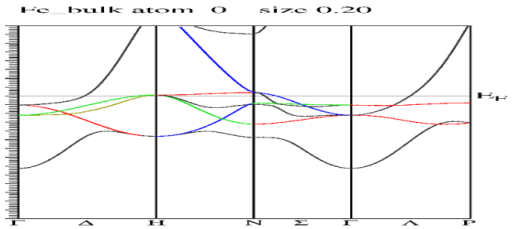

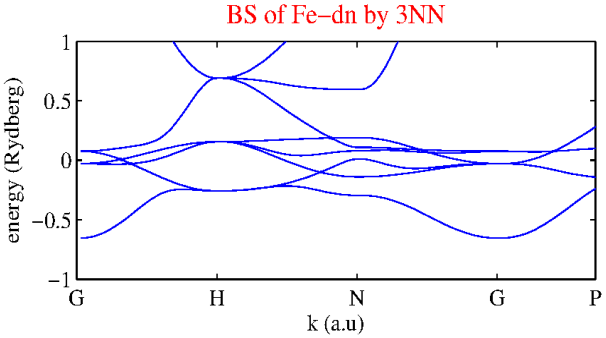

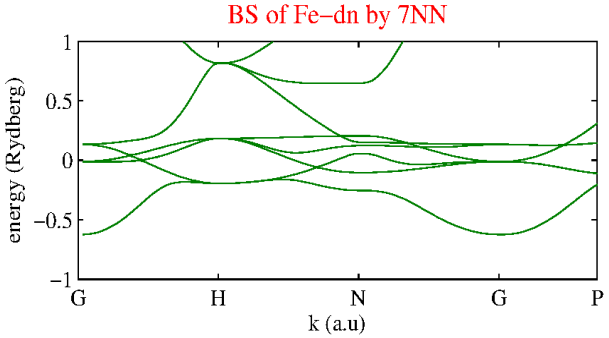

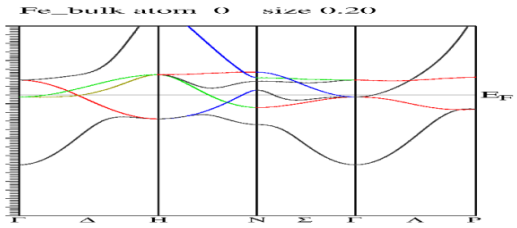

GaAs zineblende/wurtzite heterostructure

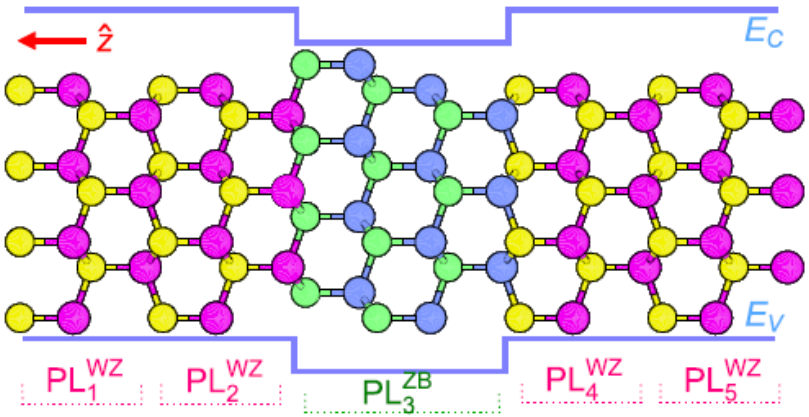

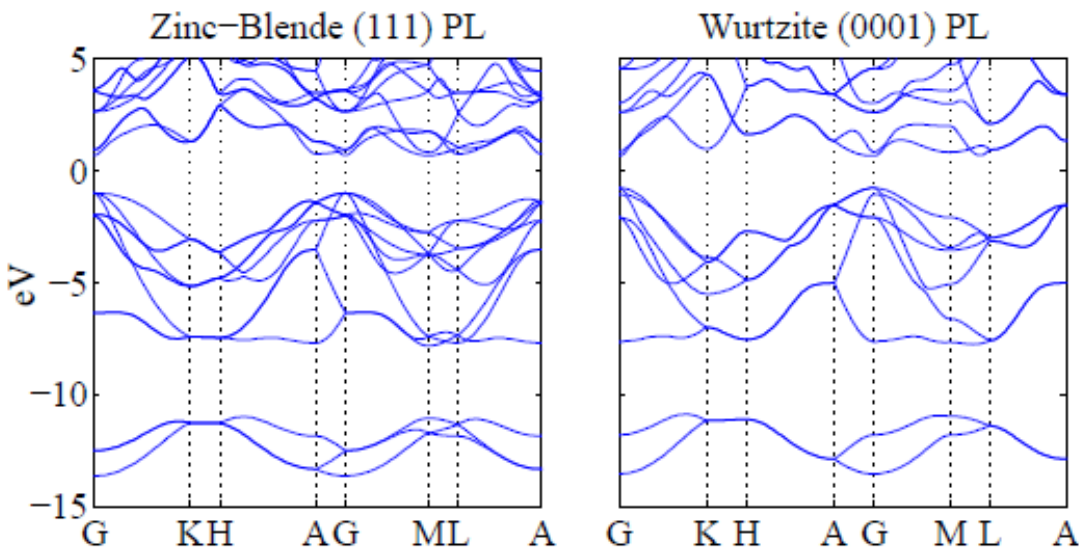

H. Shtrikman et al., Nano Lett., **9**, 215 (2009);

D. Spirkoska1 et al., https://arxiv.org/ftp/arxiv/papers/0907/0907.1444.pdf

Transport characteristics of GaAs ZB/WZ junctions

Potential for zine-blende(ZB)/wurtzite(WZ) heterostructure

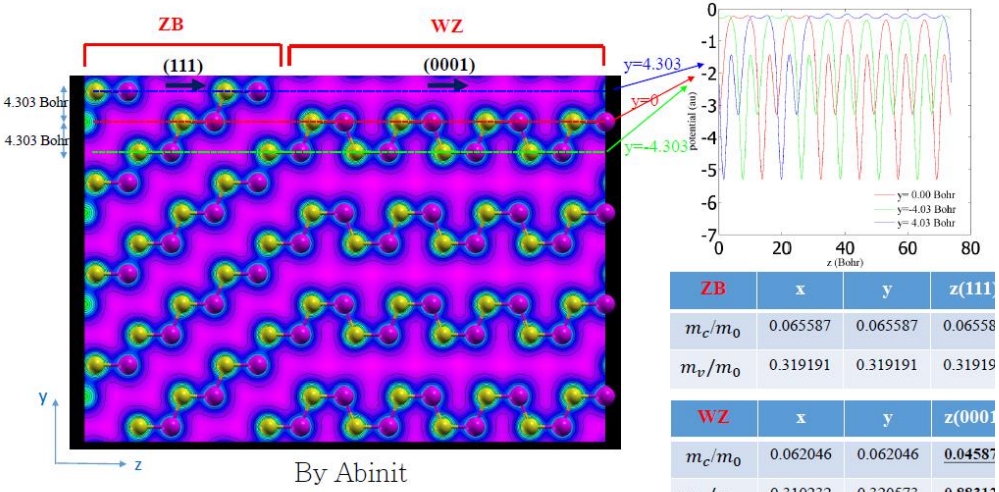

By Abinit

ZB	x	y	z(111)
m_c/m_0	0.065587	0.065587	0.06558
m_v/m_0	0.319191	0.319191	0.31919

WZ	x	y	z(0001)
m_c/m_0	0.062046	0.062046	0.04587
m_v/m_0	0.310232	0.320573	0.88312

Normal-incidence conductance

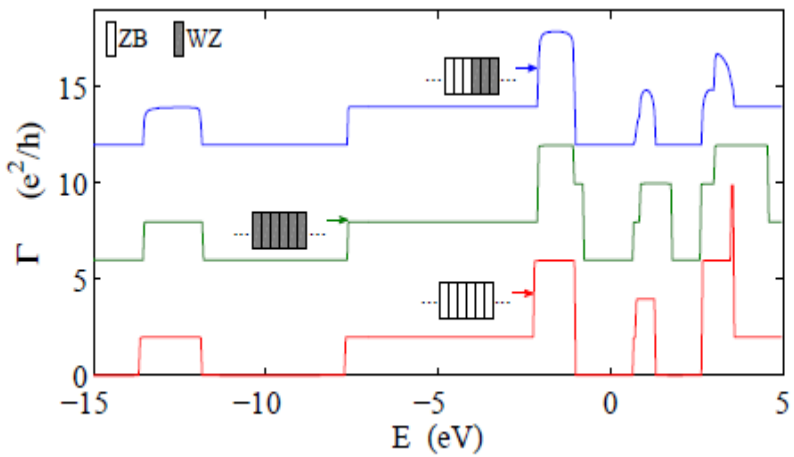

Total potentials of Ga and As atoms by lasto64

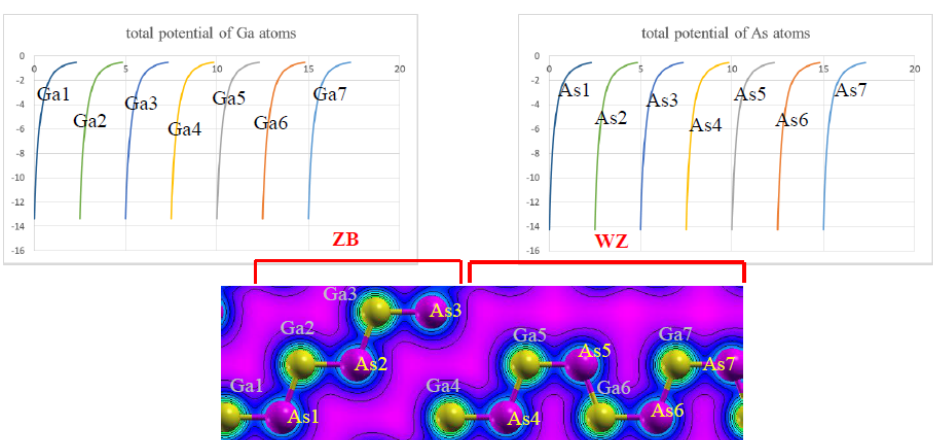

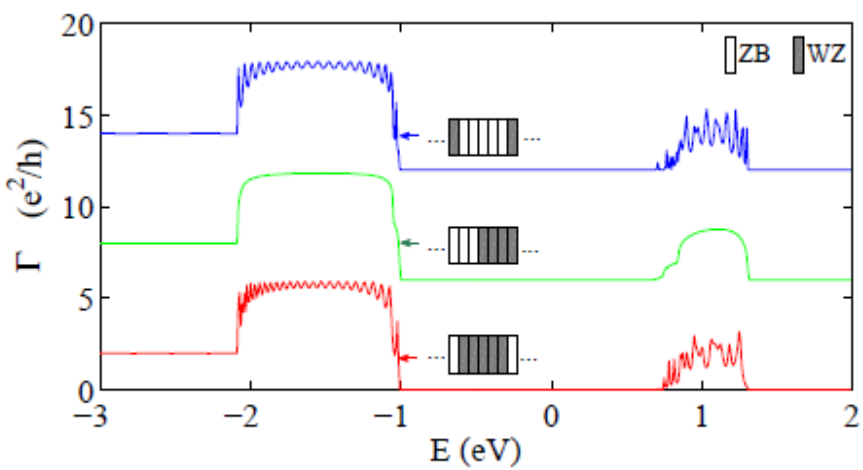

Tunneling current spectroscopy of a nanostructure junction involving multiple energy levels

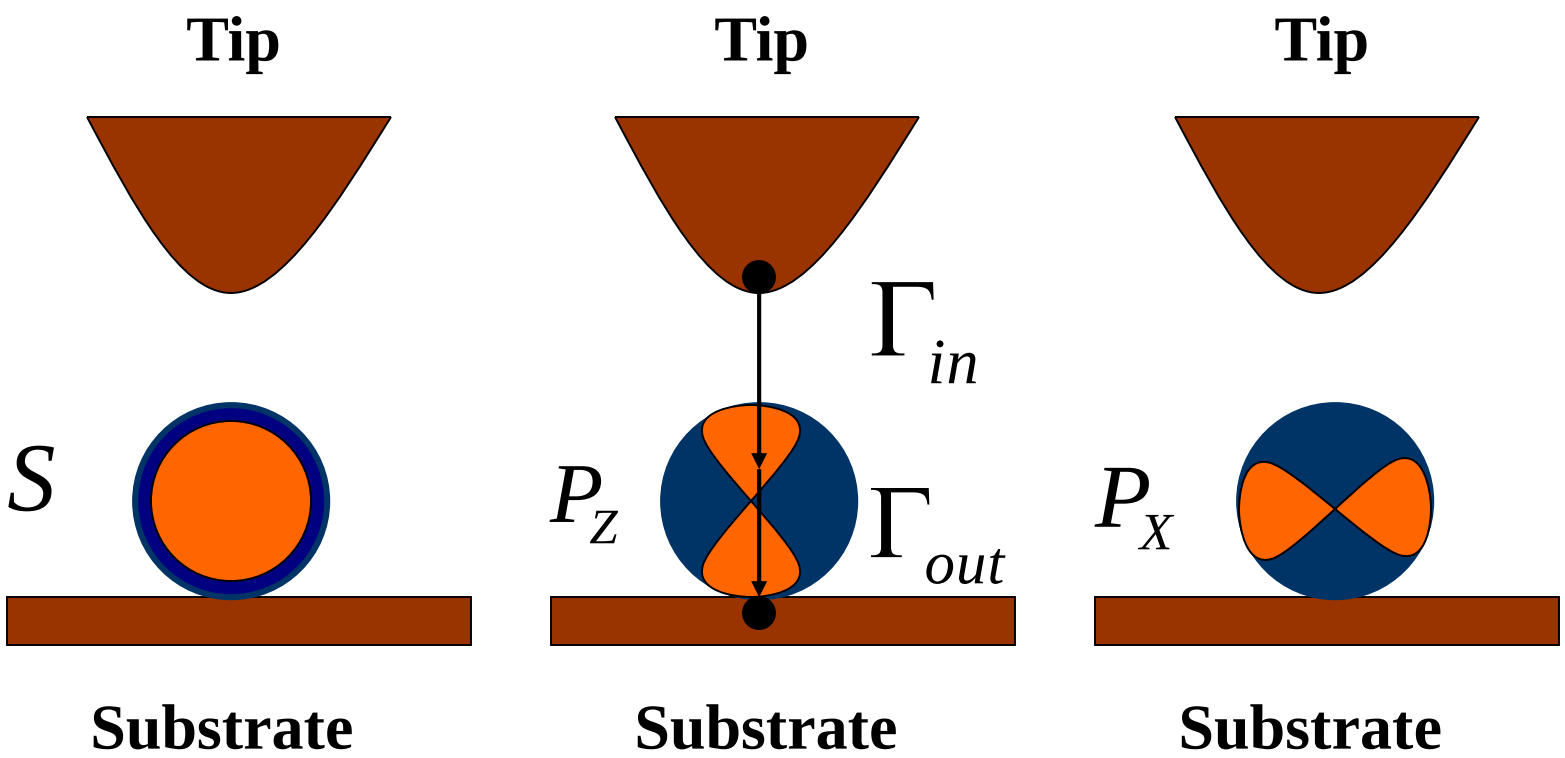

E_s, E_{p_z}, E_d

P. Liljeroth et al, Phys. Chem.chem. Phys. 8, 3845 (2006)

Energy diagram for STM-QD junction

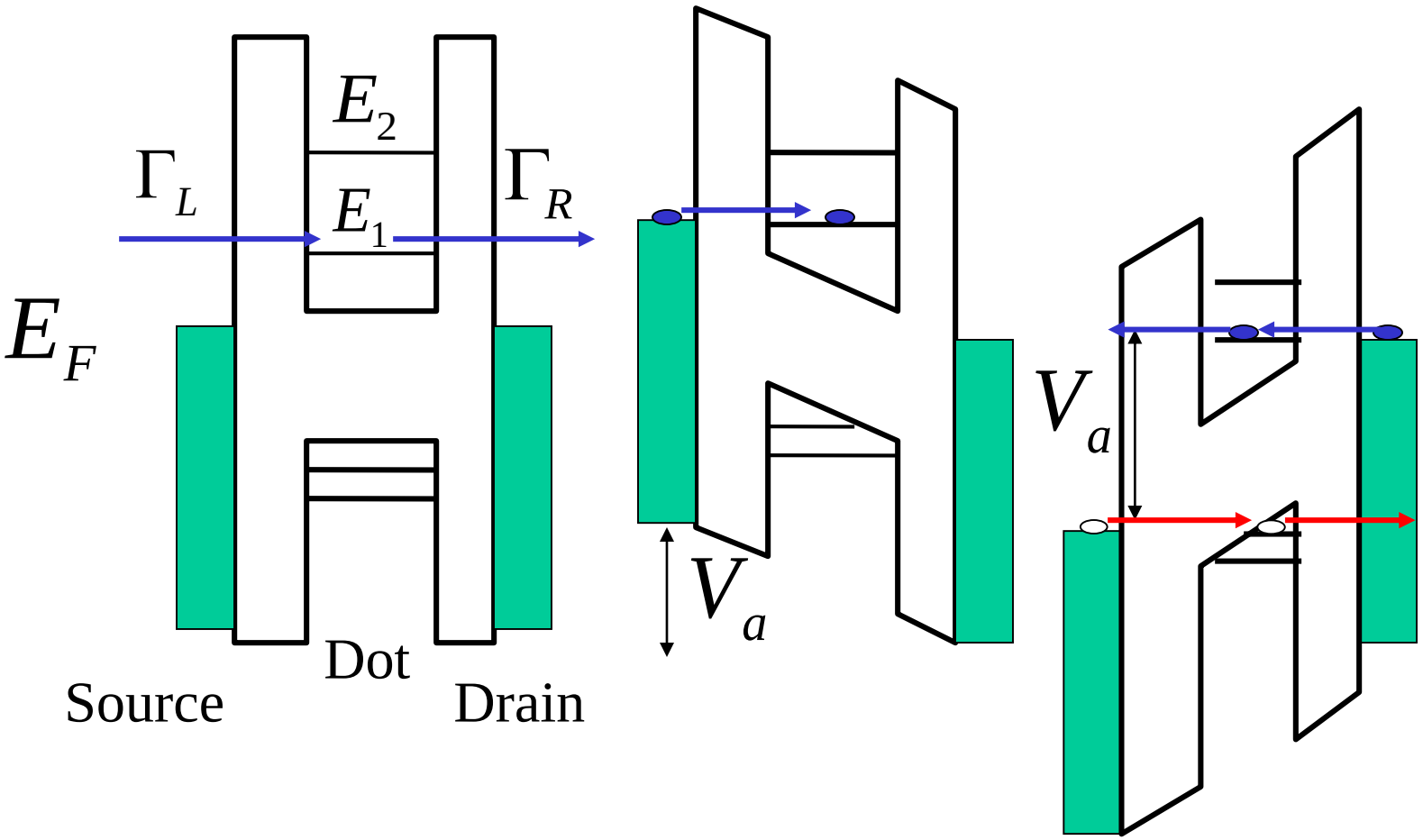

(a) No bias (b) Forward bias (c) Reverse bias

Theory vs. Experiment for STM-QD tunneling spectra

[Data from L. Jdira et al., Phys. Rev. B 73, 115305 (2006)]

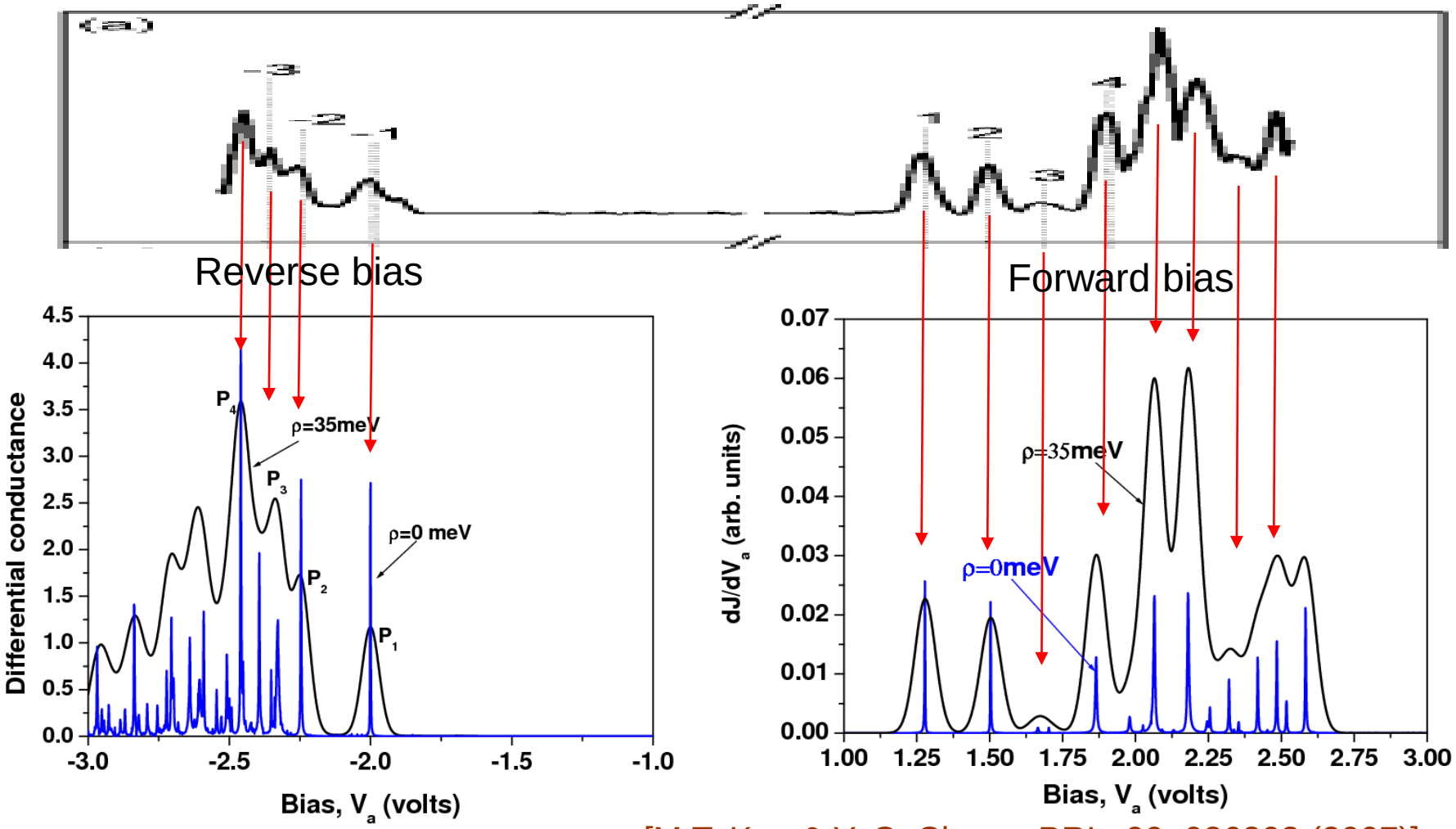

[M.T. Kuo & Y. C. Chang, PRL, 99, 086803 (2007)]

M-level case

$$a^j \equiv 1-(N_{j,\sigma}+N_{j,-\sigma})+\langle n_{j\sigma}n_{j-\sigma}\rangle$$

$$b^j \equiv N_{j,\sigma}+N_{j,-\sigma}-2\langle n_{j\sigma}n_{j-\sigma}\rangle$$

$$c^j \equiv \langle n_{j\sigma}n_{j-\sigma}\rangle$$

$$\ell \neq j \neq j'$$

$$a^{j'} \equiv 1-(N_{j',\sigma}+N_{j',-\sigma})+\langle n_{j'\sigma}n_{j'-\sigma}\rangle$$

$$b^{j'} \equiv N_{j',\sigma}+N_{j',-\sigma}-2\langle n_{j'\sigma}n_{j'-\sigma}\rangle$$

$$c^{j'} \equiv \langle n_{j'\sigma}n_{j'-\sigma}\rangle$$

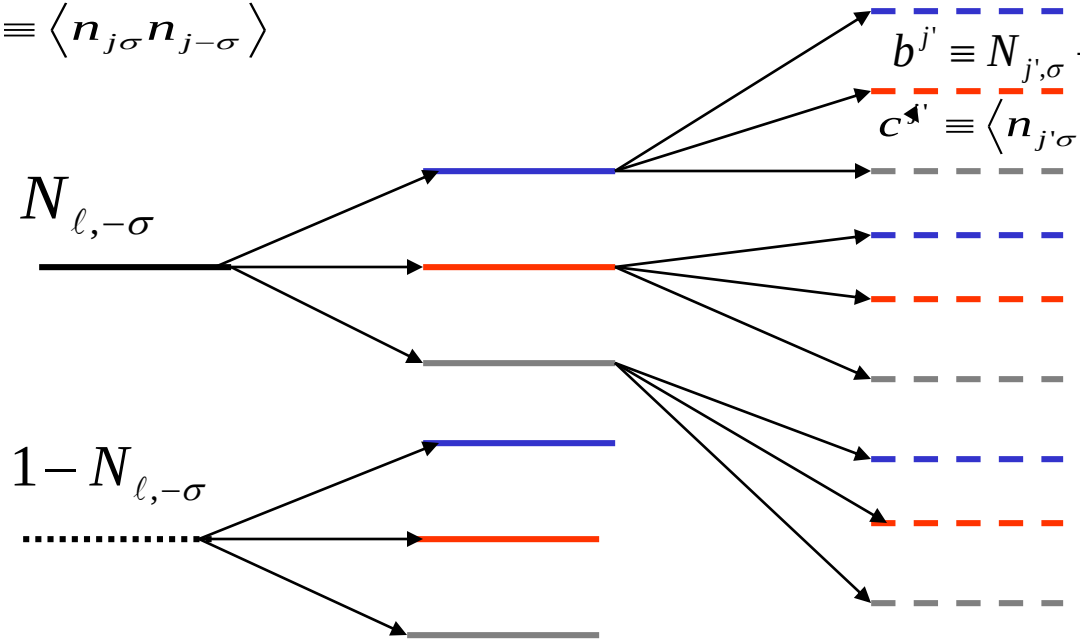

$$p_1 = a^j a^{j'},\ p_2 = b^j a^{j'},\ p_3 = a^j b^{j'},\ p_4 = c^j a^{j'},\ p_5 = c^{j'} a^j, ..$$

$$\Pi_1 = 0, \Pi_2 = U_{\ell j}, \Pi_3 = U_{\ell j'}, \Pi_4 = 2U_{\ell j}, \Pi_5 = 2U_{\ell j'},$$

•單光子發射器(Single-Photon generator)

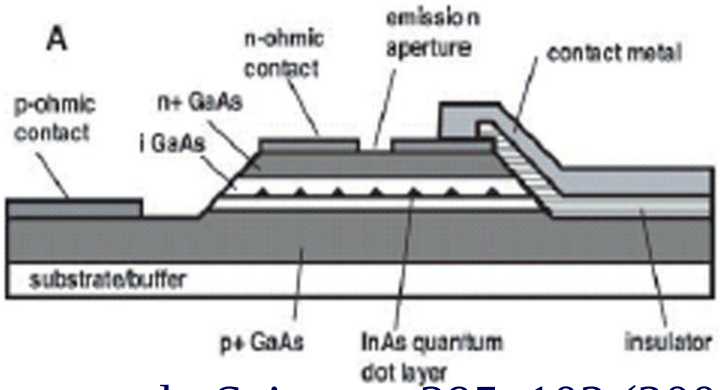

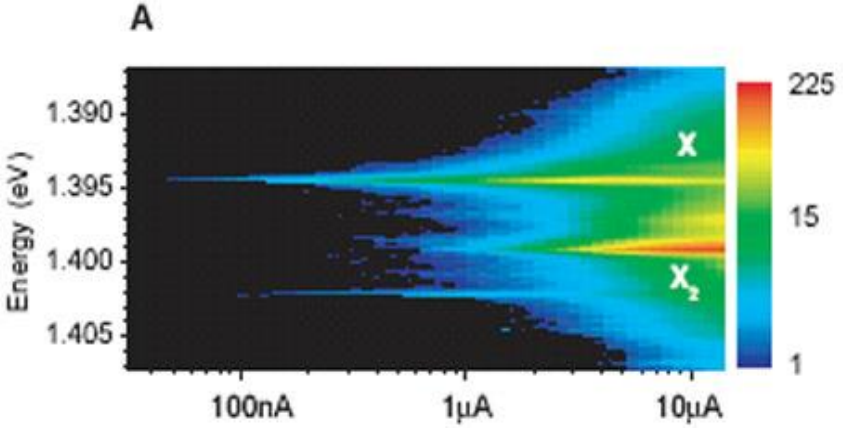

Z. Yuan et al., Science, 295, 102 (2002)

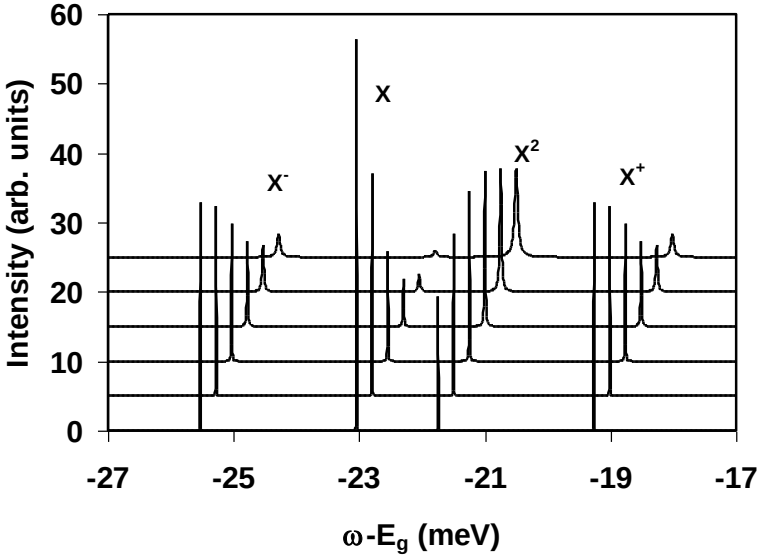

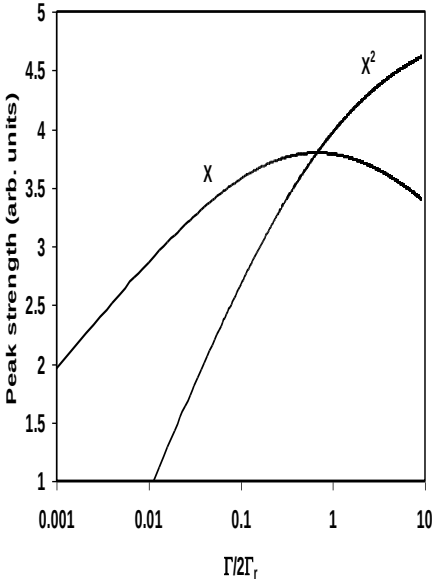

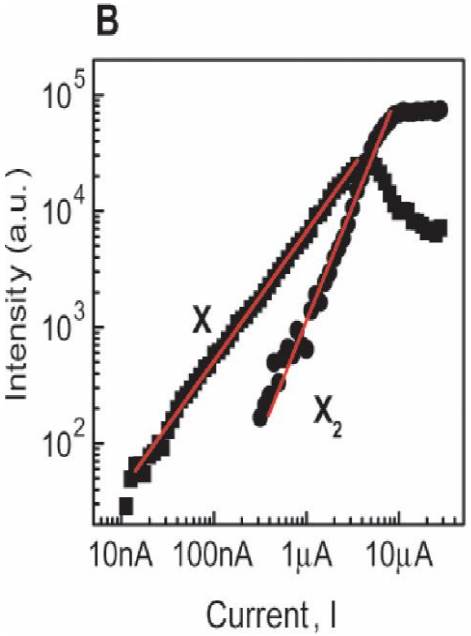

M. T. Kuo, Y. C. Chang, PRB

Quantum interference in triple-QD junction

[C. C. Chen, Y. C. Chang, M. T. Kuo, ***PCCP***, **17**, 6606 (2015)]

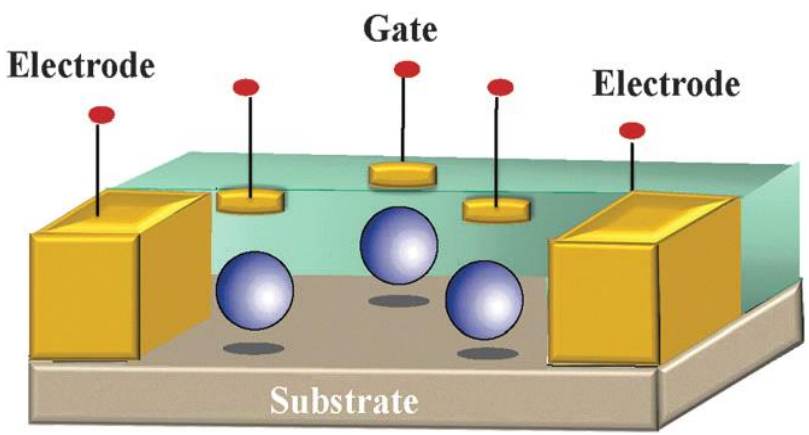

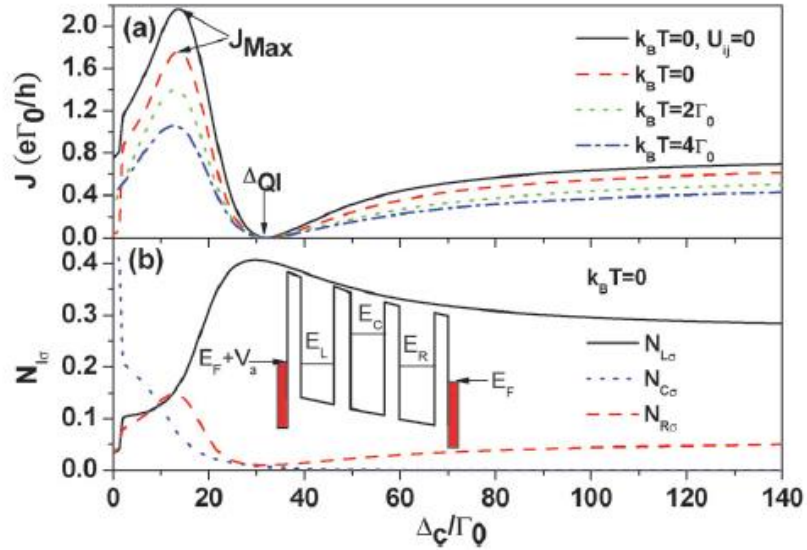

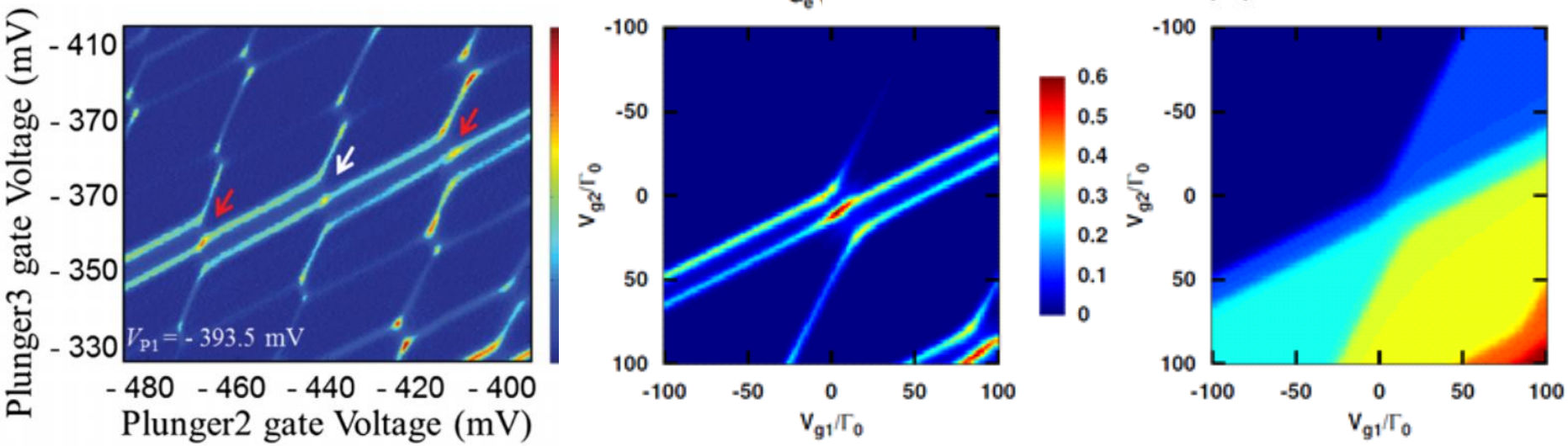

[M. Seo et al., Phys. Rev. Lett.**110**, 046803 (2013)]

Thermal rectification properties of QD junctions

[M. T. Kuo, Y. C. Chang, Phys. Rev. B **81**, 205321 (2010)]

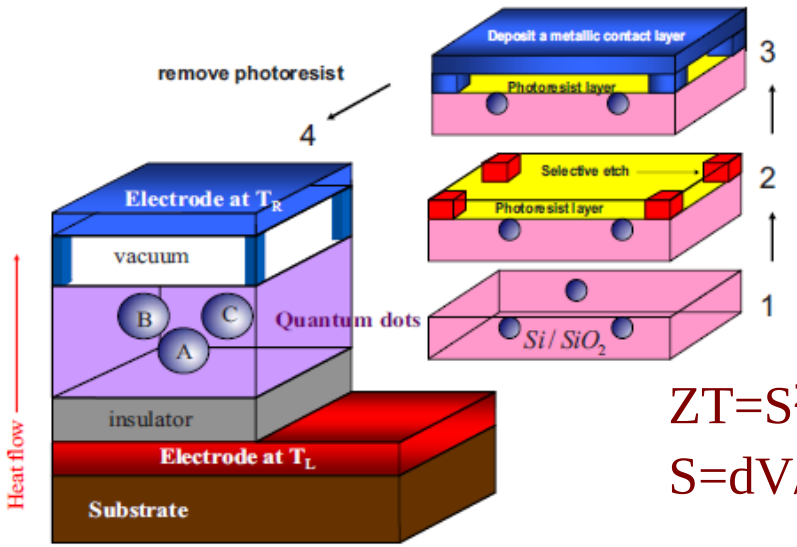

$ZT=S^2GT/k$

$S=dV/dT$

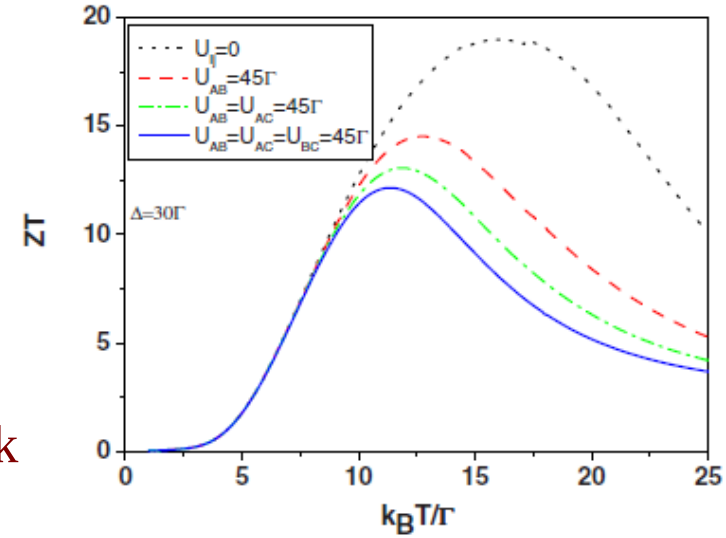

FIG. 3. (Color online) Figure of merit ZT as a function of temperature for various quantum dot configurations.

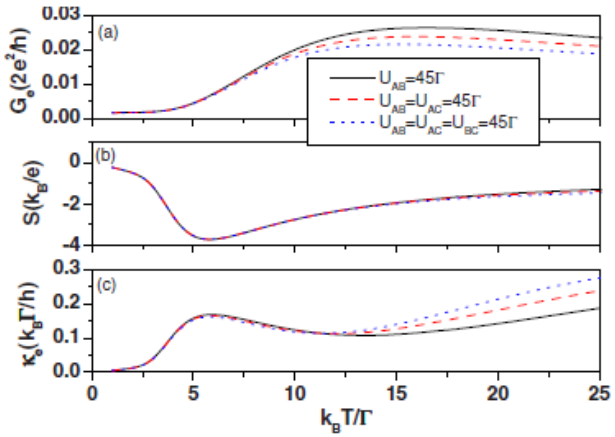

FIG. 6. (Color online) Electrical conductance G_e, thermal power S, and electron thermal conductance κ_e as a function of temperature for various quantum dot configurations.

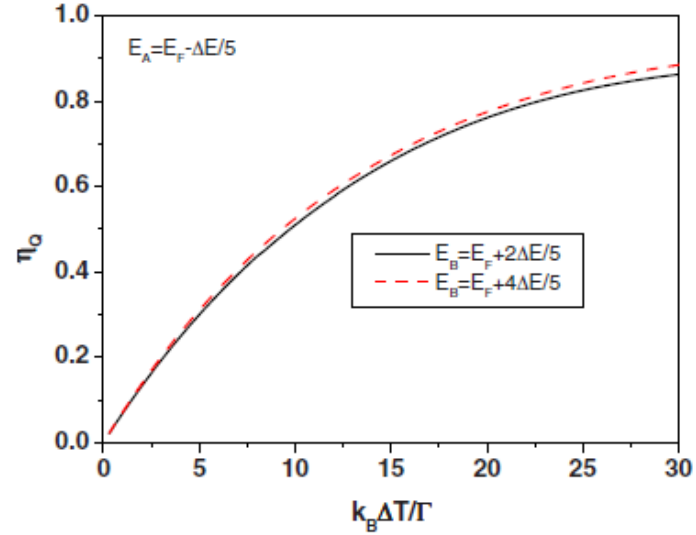

Thermoelectric properties of TQD junctions

[C. C. Chen, M. T. Kuo, Y. C. Chang, ***PCCP***, **17**, 19386 (2015)]

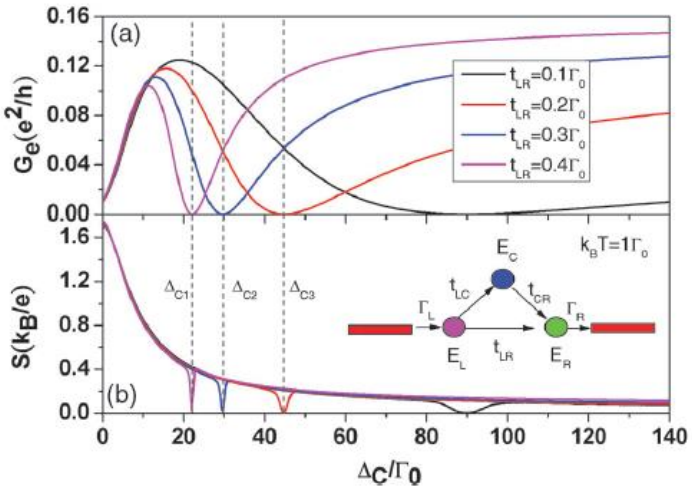

Fig. 1 (a) Electrical conductance (G_e) and (b) Seebeck coefficient (S) of TQDMs as a function of central QD energy ($\Delta_C = E_C - E_F$) for different t_{LR} strengths at $E_L = E_R = E_F$, $t_{LC} = t_{CR} = t_c = 3\Gamma_0$ and $k_BT = 1\Gamma_0$. We assume $U_{LC} = U_{CR} = 30\Gamma_0$, $U_{LR} = 10\Gamma_0$, $U_\ell = U_0 = 100\Gamma_0$ and $\Gamma_L = \Gamma_R = \Gamma = 0.3\Gamma_0$.

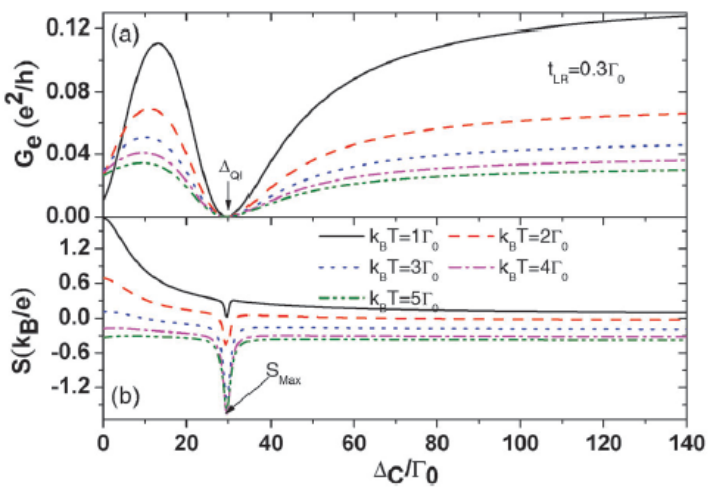

Fig. 2 (a) Electrical conductance (G_e) and (b) Seebeck coefficient (S) of

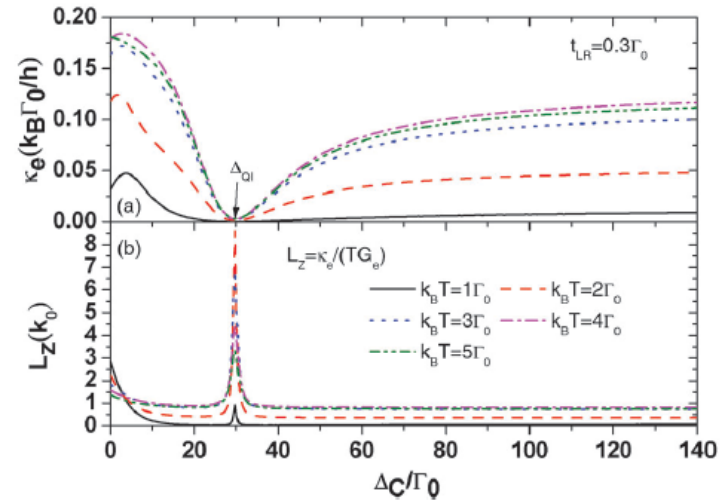

Fig. 4 (a) Electron thermal conductance (κ_e), and (b) Lorenz number ($\kappa_e/(G_eT)$) as a function of central QD energy for different temperatures. The curves of Fig. 4 correspond to those of Fig. 2. $k_0 = k_B^2/e^2$.

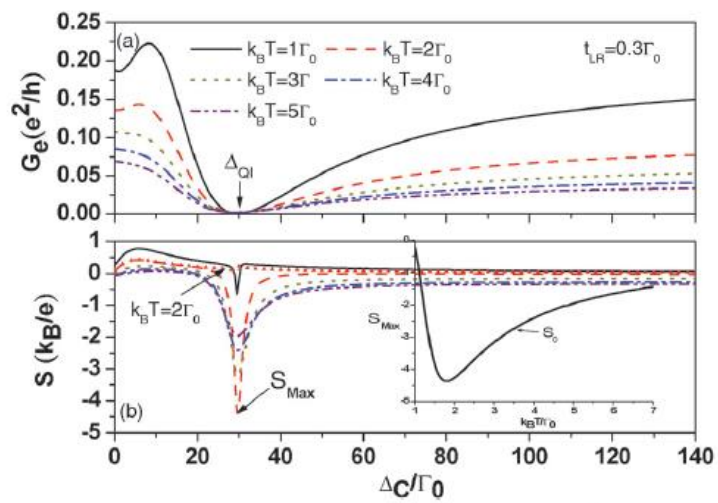

Fig. 3 The curves of Fig. 3 are one to one corresponding to those of Fig. 2. The calculation of Fig. 3 only considers the single particle occupation

TE behavior of QD array

[M. T. Kuo, Y. C. Chang, Nanotechnology **24** 175403 (2013)]

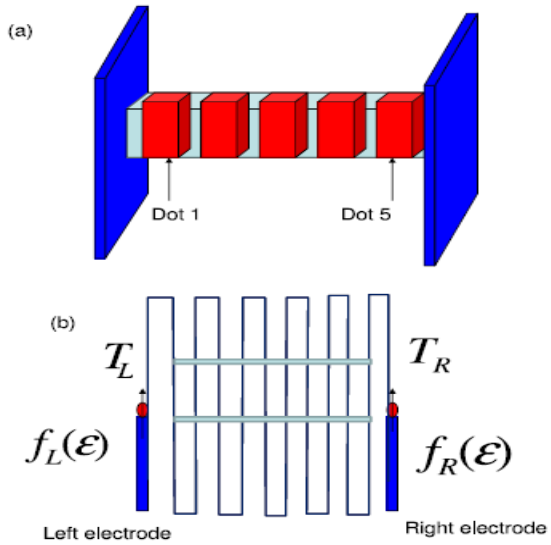

$$\kappa_{ph} = \frac{\pi^2 k_B^2 T}{3h} F_s \qquad (F_s=0.01)$$

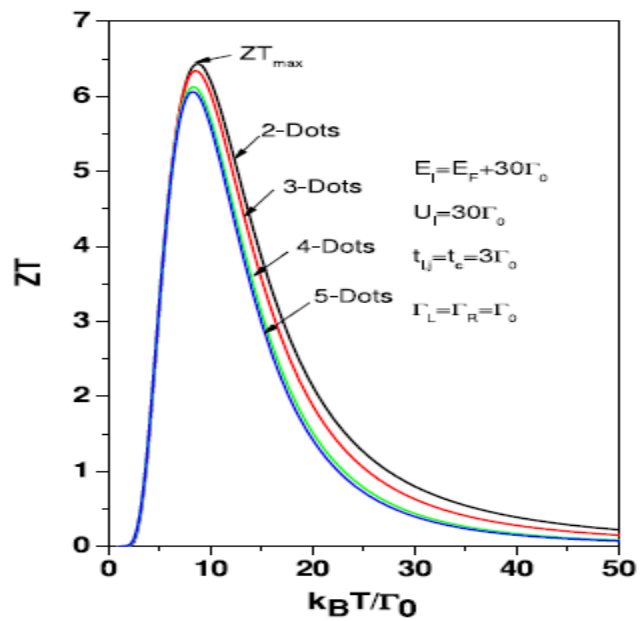

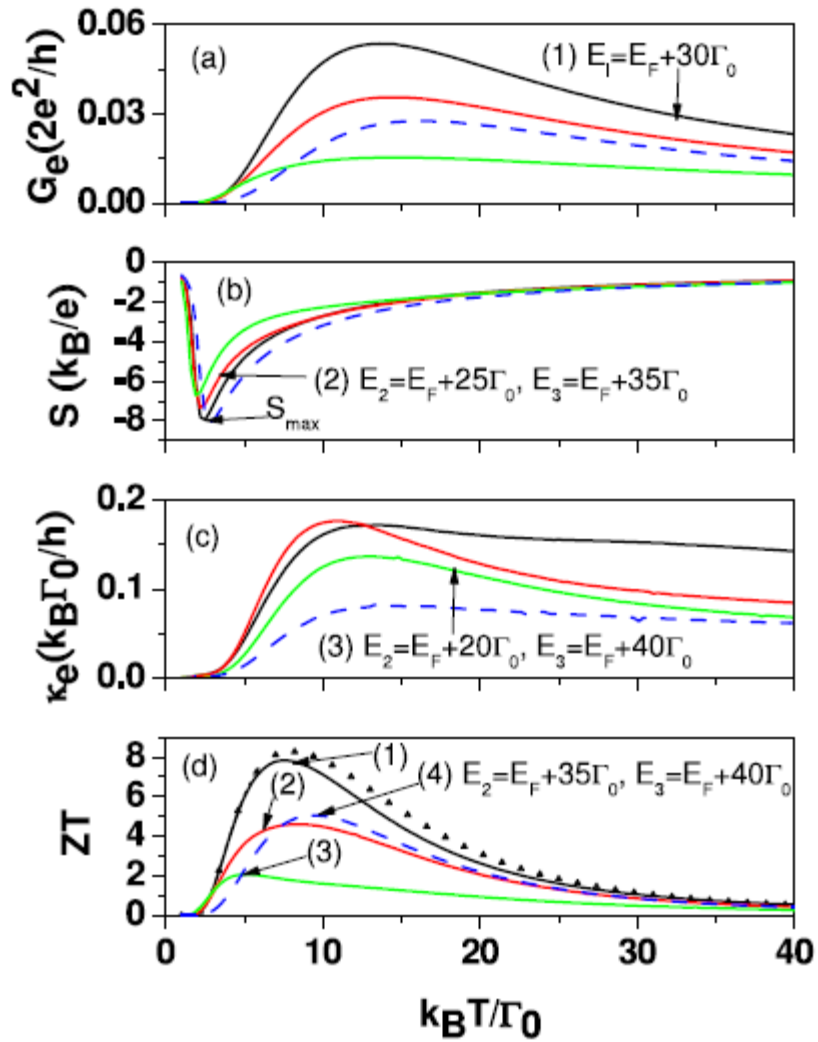

Enhancement in TE efficiency of QD junctions dueto increase of level degeneracy

[M. T. Kuo, C. C. Chen,Y. C. Chang, Phys. Rev. B **95**, 075432 (2017)]

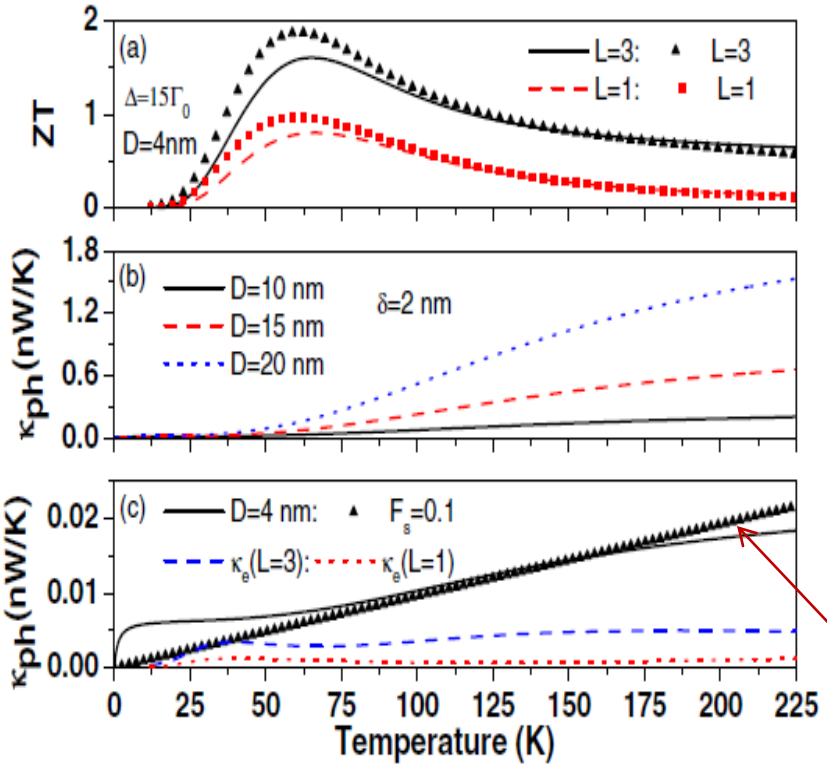

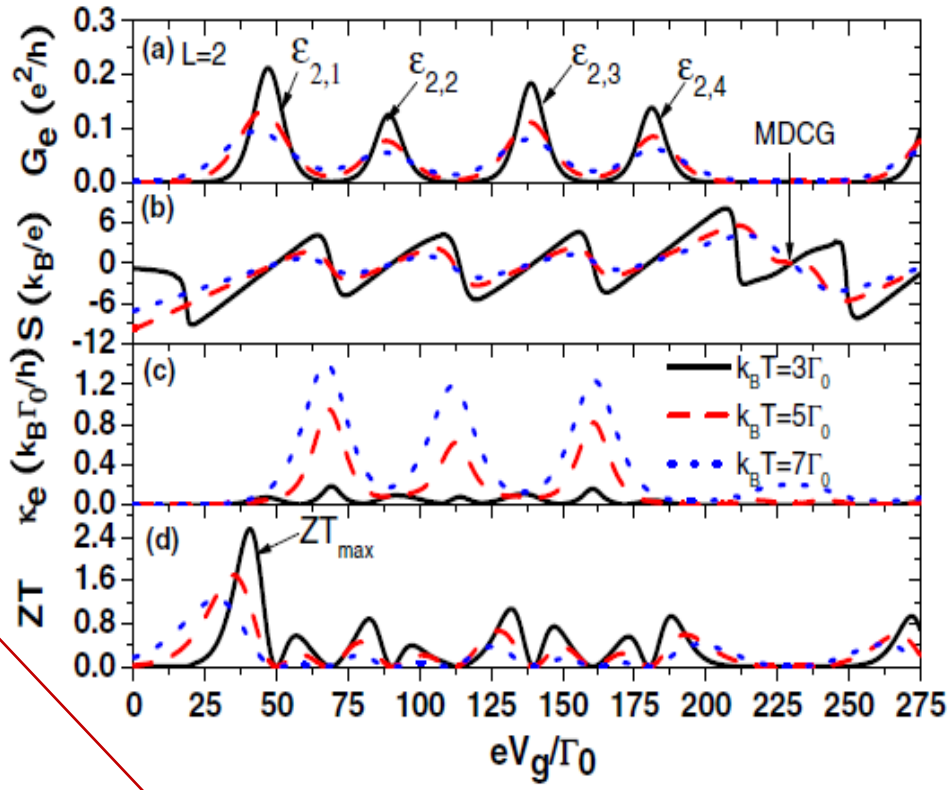

$$\kappa_{ph} = \frac{\pi^2 k_B^2 T}{3h} F_s \quad (F_s=0.1)$$

Single QD

DQD

[P. Murphy and J. Moore, Phys. Rev. B 76, 155313 (2007)]

Summary

- Computation codes were implemented for electronic and optical exciation calculations by using symmetry adapted PW & LASTO basis.
- Electronic states and optical linear response of nanoclusters (with high symmetry) by including the quasi-particle self-energy correction (GW approximation) and the excitonic effects can be calculated efficiently.
- For high-symmetry (Oh,Td,C3v,D2d) systems, our method improves the computation efficiency by two-three orders of magnitude.
- Self-assembled or colloidal QDs can be suitably modeled by VFF model for strain distribution+EBOM for electronic states
- Intra-level and inter-level Coulomb interactions play keys roles in the optical properties
- Non-equilibrium transport and correlation are important in the analysis of nanostructure junction devices
- Computation codes were implemented for electronic and optical exciation calculations of 1D and 2D materials by using PW-B spline mixed basis.

DFT with LASTO basis

A LASTO basis function at a given site (taken as the origin) is defined as

$$\psi_N(\mathbf{r}) = r^{n-1} e^{-\zeta_{nl} r} Y_{lm}(\hat{r})$$

for $\mathbf{r}$ outside muffin-tin (MT) spheres and

$$\psi_N(\mathbf{r}) = \sum_{\tilde{N}} [\beta_{N\tilde{N}} g_{\tilde{l}}(r_{\tilde{i}}) + \alpha_{N\tilde{N}} \dot{g}_{\tilde{l}}(r_{\tilde{i}})] Y_{lm}(\hat{r}_{\tilde{i}})$$

for $\mathbf{r}$ inside MTs sphere, where N is a composite index for the LASTO orbitals, which includes the site index i and orbital index $\{nlm\}$, while $\tilde{N}$ is a composite index for $\{\tilde{i}, \tilde{l}, \tilde{m}\}$, which labels the spherical harmonics expansion of the basis function at site $\tilde{i}$. ζ_{nl} denotes the exponents

J. W. Davenport, Phys. Rev. B **29**, 2896 (1994).
J. W. Davenport, M. Weinert, R. E. Watson, Phys. Rev. B **32**, 4876 (1994).
J. W. Davenport, R. E. Watson, M. Weinert, Phys. Rev. B **32**, 4883 (1994).

•Optical spectra of SiH_4 cluster

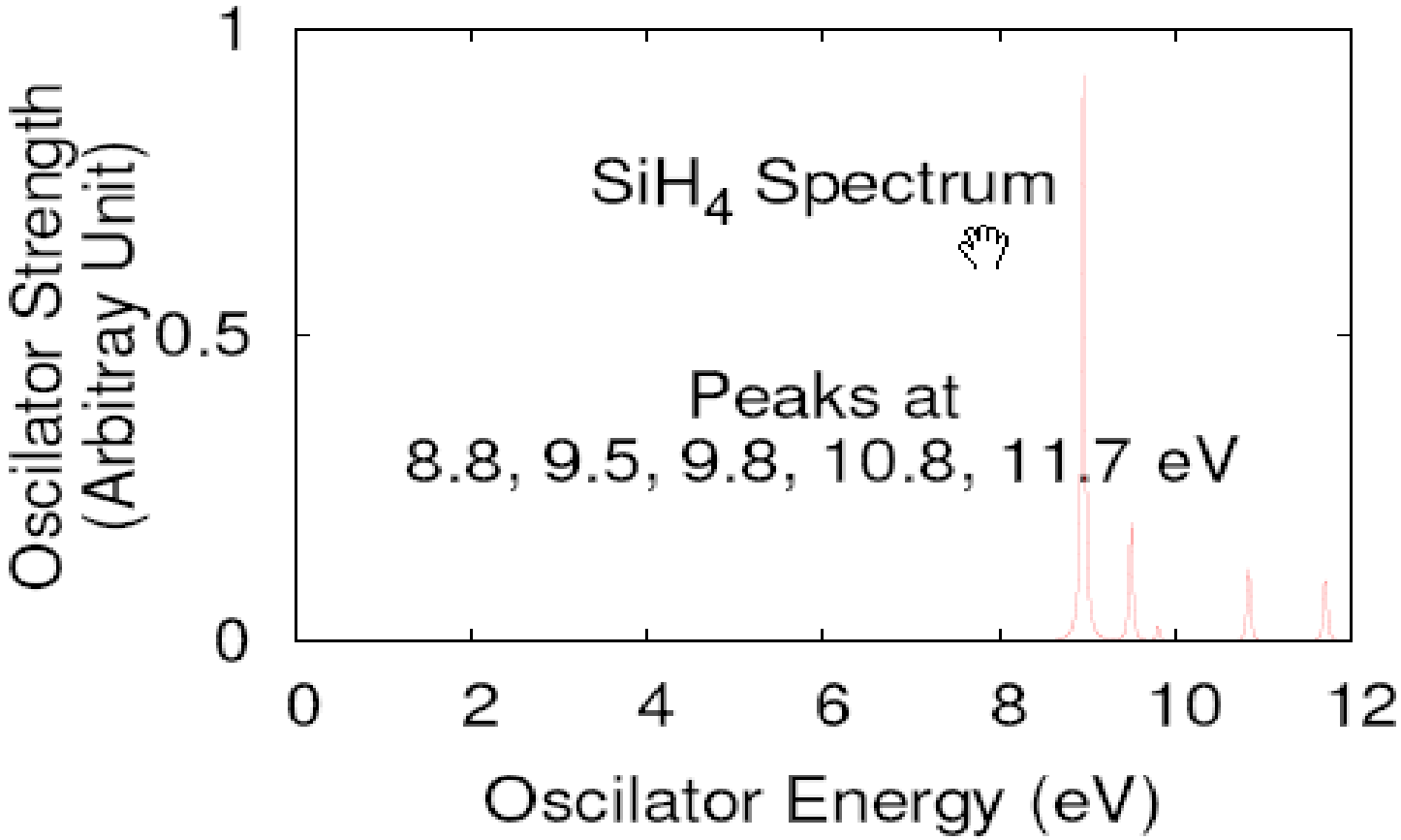

•Optical spectra of 1nm Si clusters

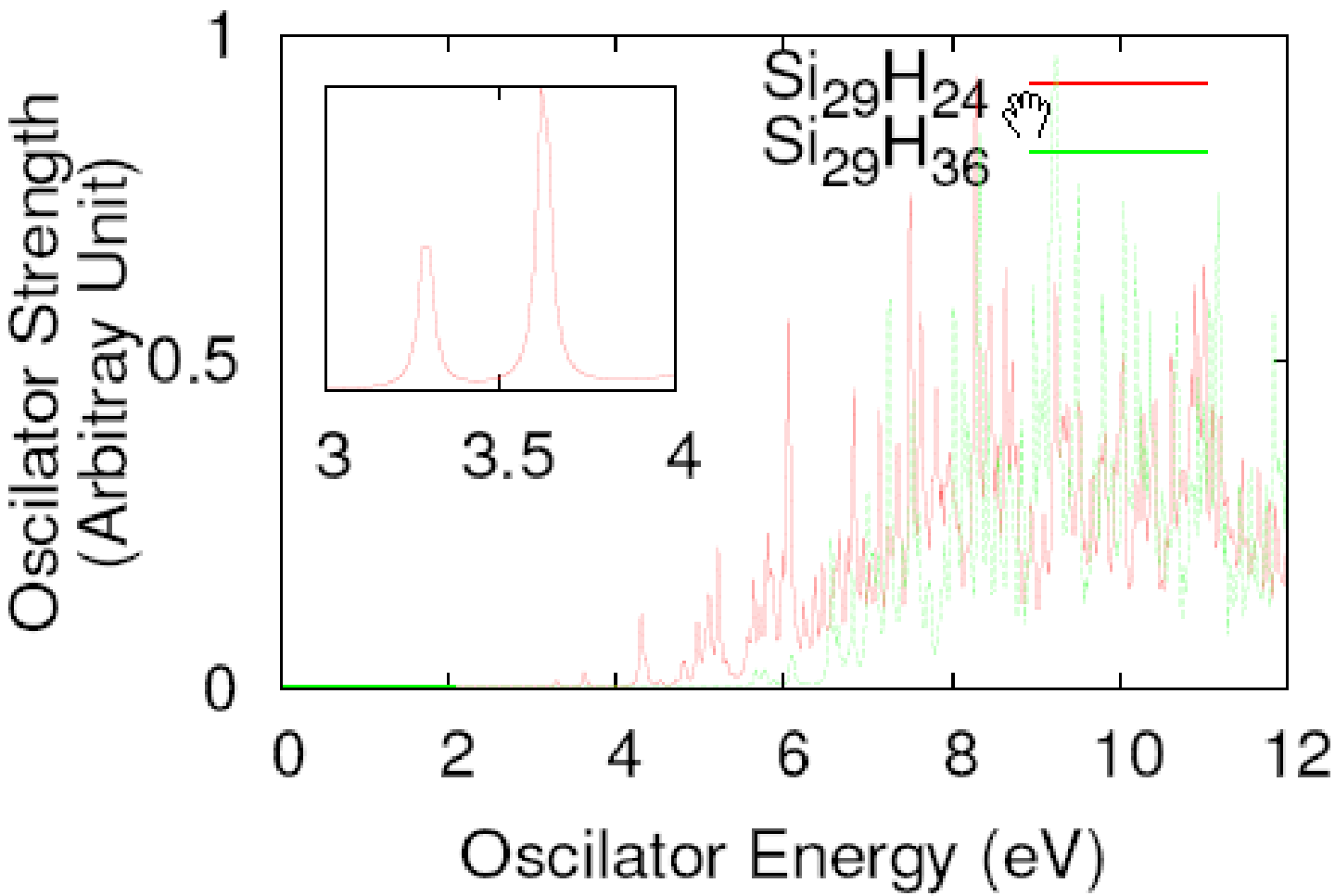

Effect of asymmetric tunneling

$$\Gamma_{out} = 1meV$$

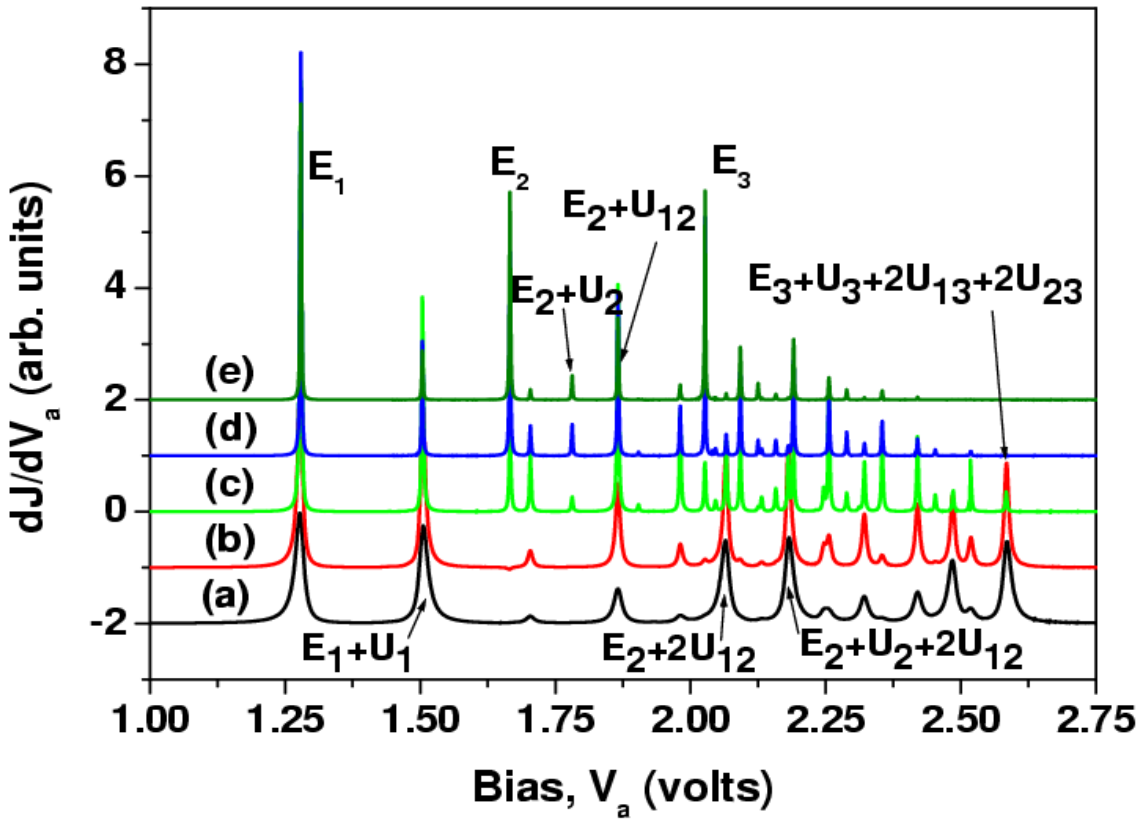

$$\Gamma_{in} = 0.1meV$$

Shell-tunneling

Shell-filling

$$\Gamma_{in} = 10meV$$

Comparison with continuum Model

J. Appl. Phys. **104**, 083524 (2008)

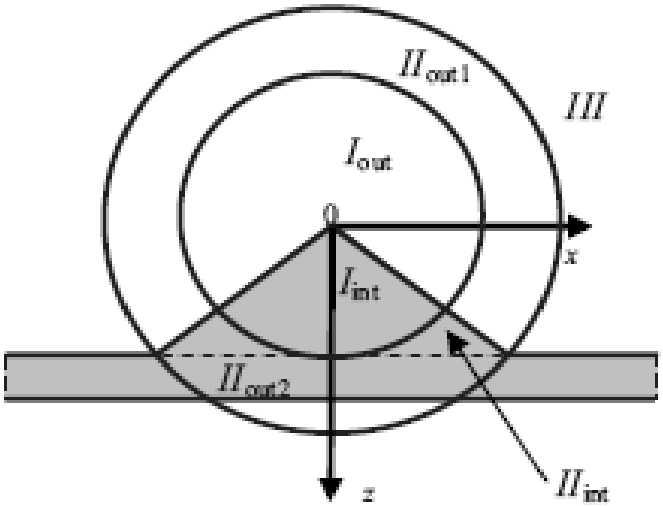

FIG. 1. The schematic representation of the QD-WL system (in gray) in a plan containing OZ axes. The specific regions I_{int}, I_{out}, II_{int}, II_{out}, and III are shown.

using Green's function method one obtains (see Refs. 8–10)

$$\mathbf{u}(\mathbf{r}) = \frac{C}{\pi}\oint \frac{1}{|\mathbf{r}-\mathbf{r}_0|} d\mathbf{S}(\mathbf{r}_0), \tag{1}$$

where $C=\varepsilon_d(1+\nu)/[4(1-\nu)]$, ν is Poisson's ratio,[13] ε_d is the interface dilation defined as $\varepsilon_d=(a_{int}-a_{ext})/a_{ext}$ (a_{ext}, a_{int} are the lattice constant of the external, internal (inclusion) material, respectively) and it coincides with the *compression*

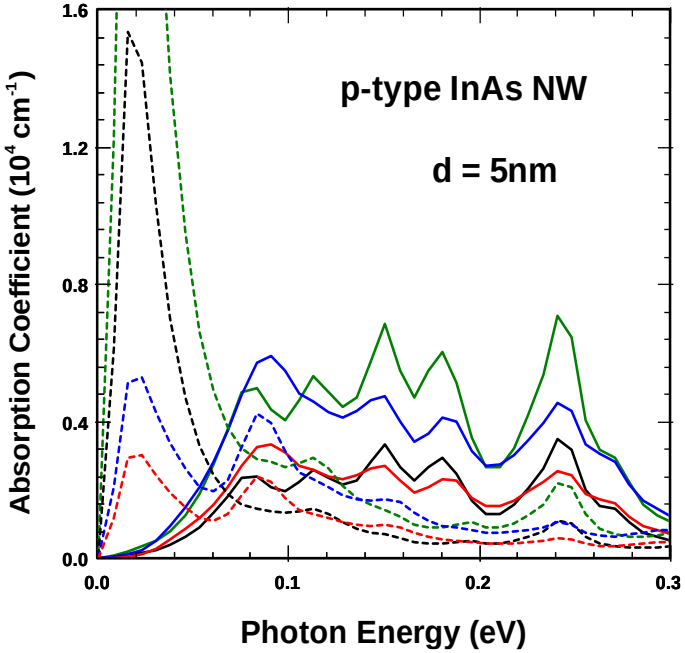
p-type InAs NW
d = 5nm
Absorption Coefficient (10^4 cm^{-1})
Photon Energy (eV)
0.0
0.4
0.8
1.2
1.6
0.0
0.1
0.2
0.3

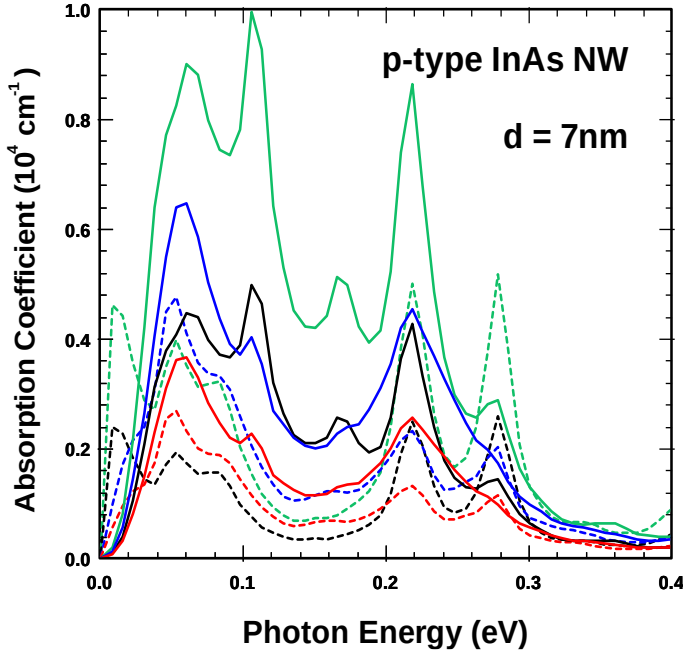
p-type InAs NW
d = 7nm
Absorption Coefficient (10^4 cm^{-1})
Photon Energy (eV)
0.0
0.2
0.4
0.6
0.8
1.0
0.0
0.1
0.2
0.3
0.4

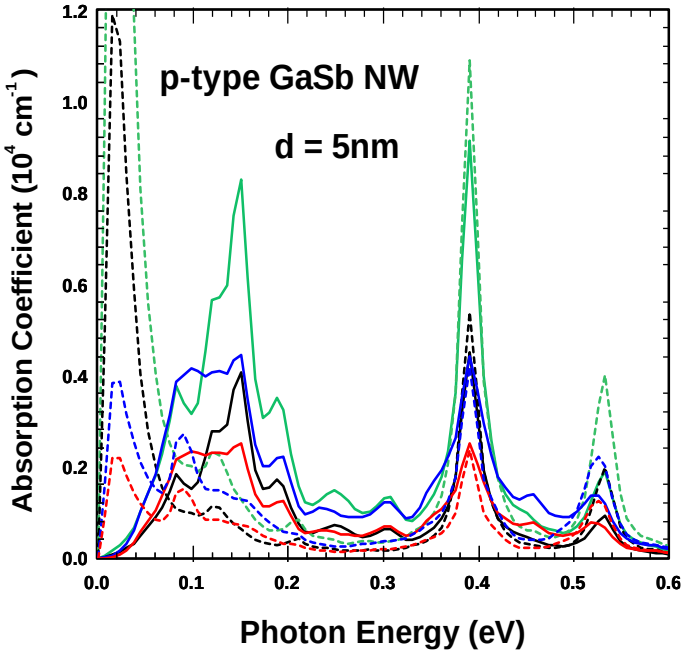
p-type GaSb NW
d = 5nm
Absorption Coefficient (10^4 cm^{-1})
Photon Energy (eV)
0.0
0.2
0.4
0.6
0.8
1.0
1.2
0.0
0.1
0.2
0.3
0.4
0.5
0.6

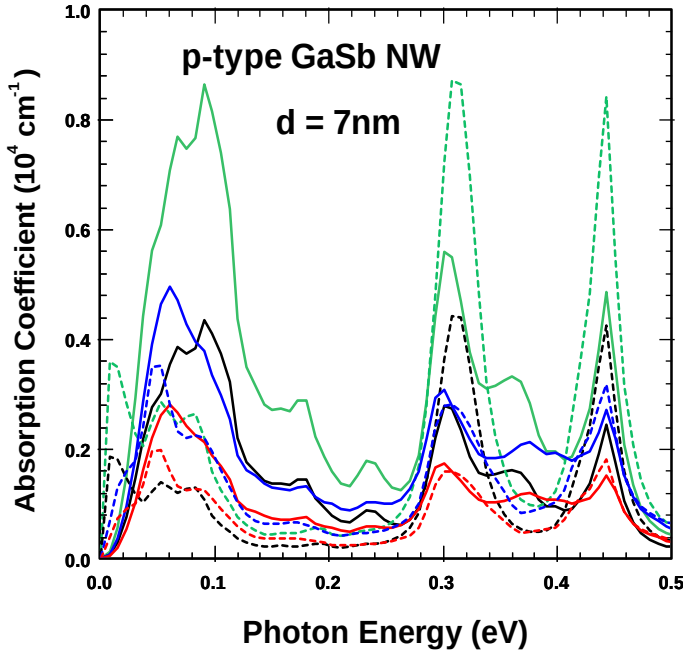
p-type GaSb NW
d = 7nm
Absorption Coefficient (10^4 cm^{-1})
Photon Energy (eV)
0.0
0.2
0.4
0.6
0.8
1.0
0.0
0.1
0.2
0.3
0.4
0.5

Modeling of Quantum Wires

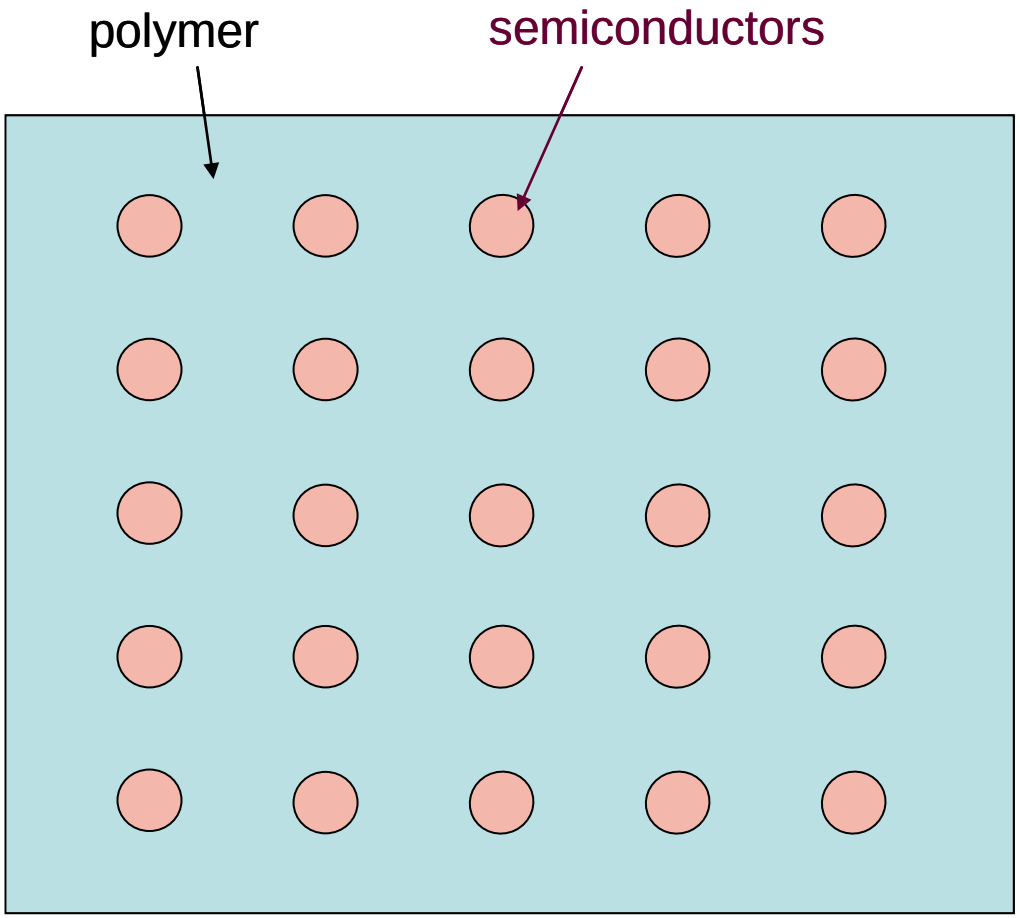

Potential for zine-blende(ZB)/wurtzite(WZ) heterostructure

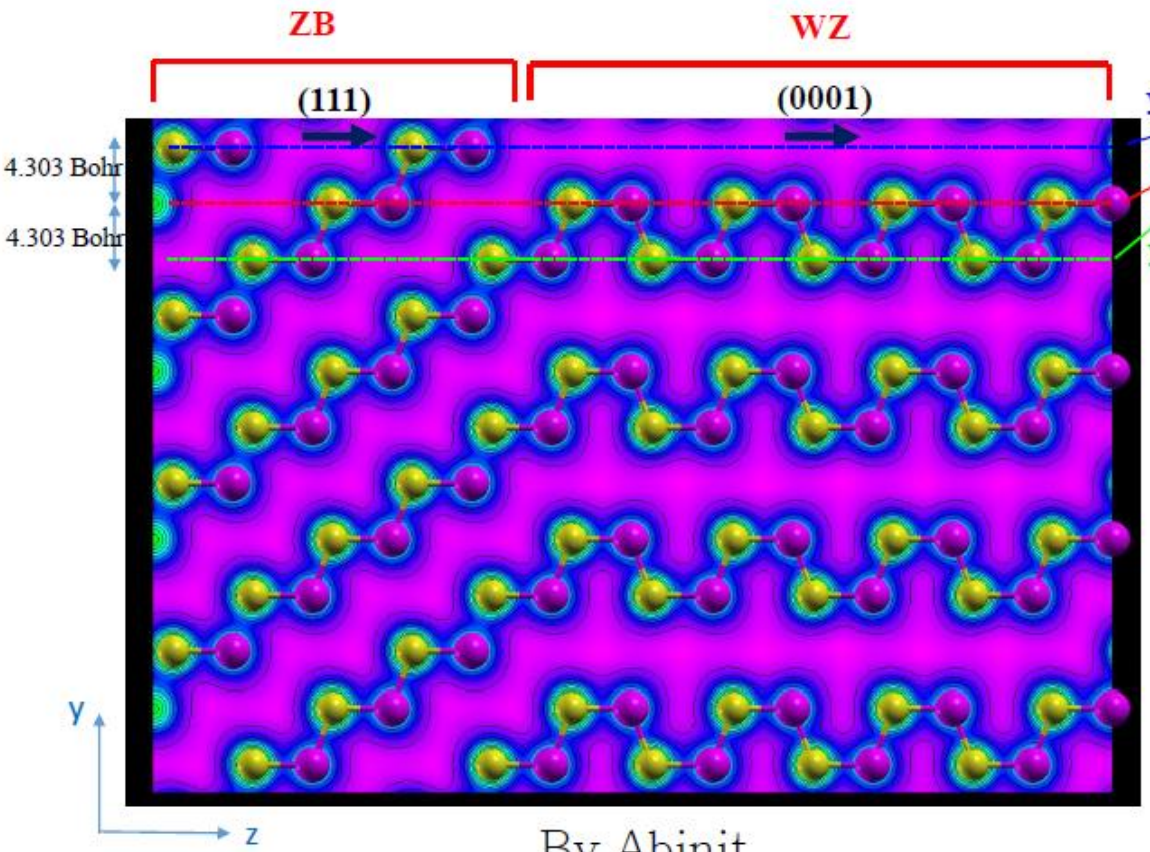

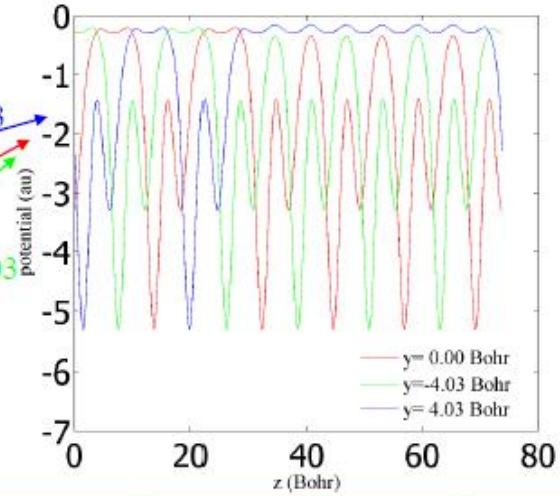

By Abinit

ZB	x	y	z(111)
m_c/m_0	0.065587	0.065587	0.065587
m_v/m_0	0.319191	0.319191	0.319191

WZ	x	y	z(0001)
m_c/m_0	0.062046	0.062046	**0.045876**
m_v/m_0	0.310232	0.320573	**0.883122**

Total potentials of Ga and As atoms by lasto64

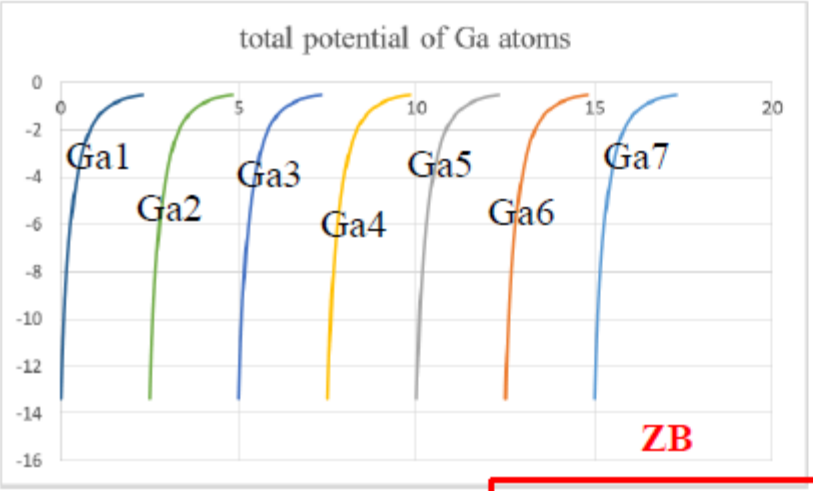

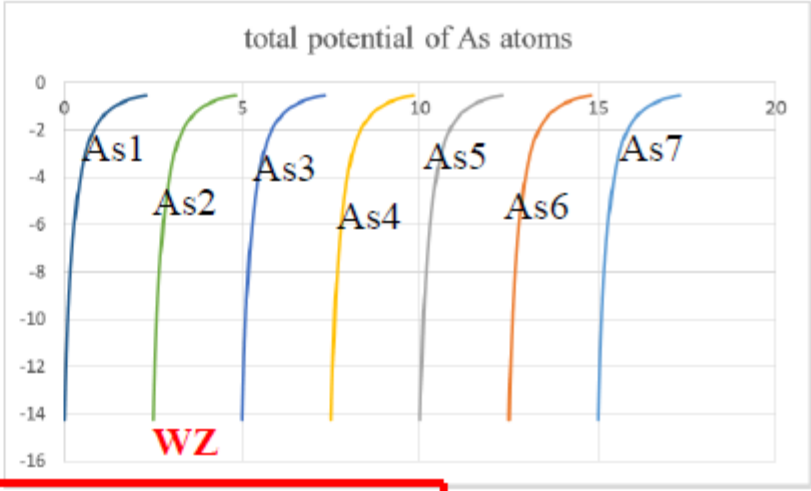

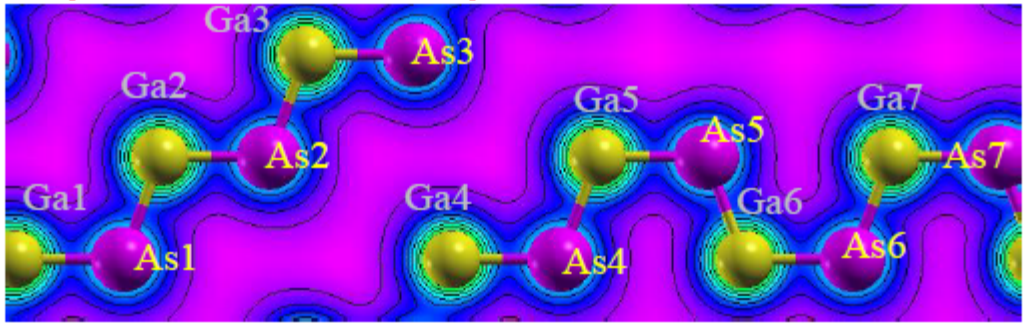

Emission spectrum of QD transistor

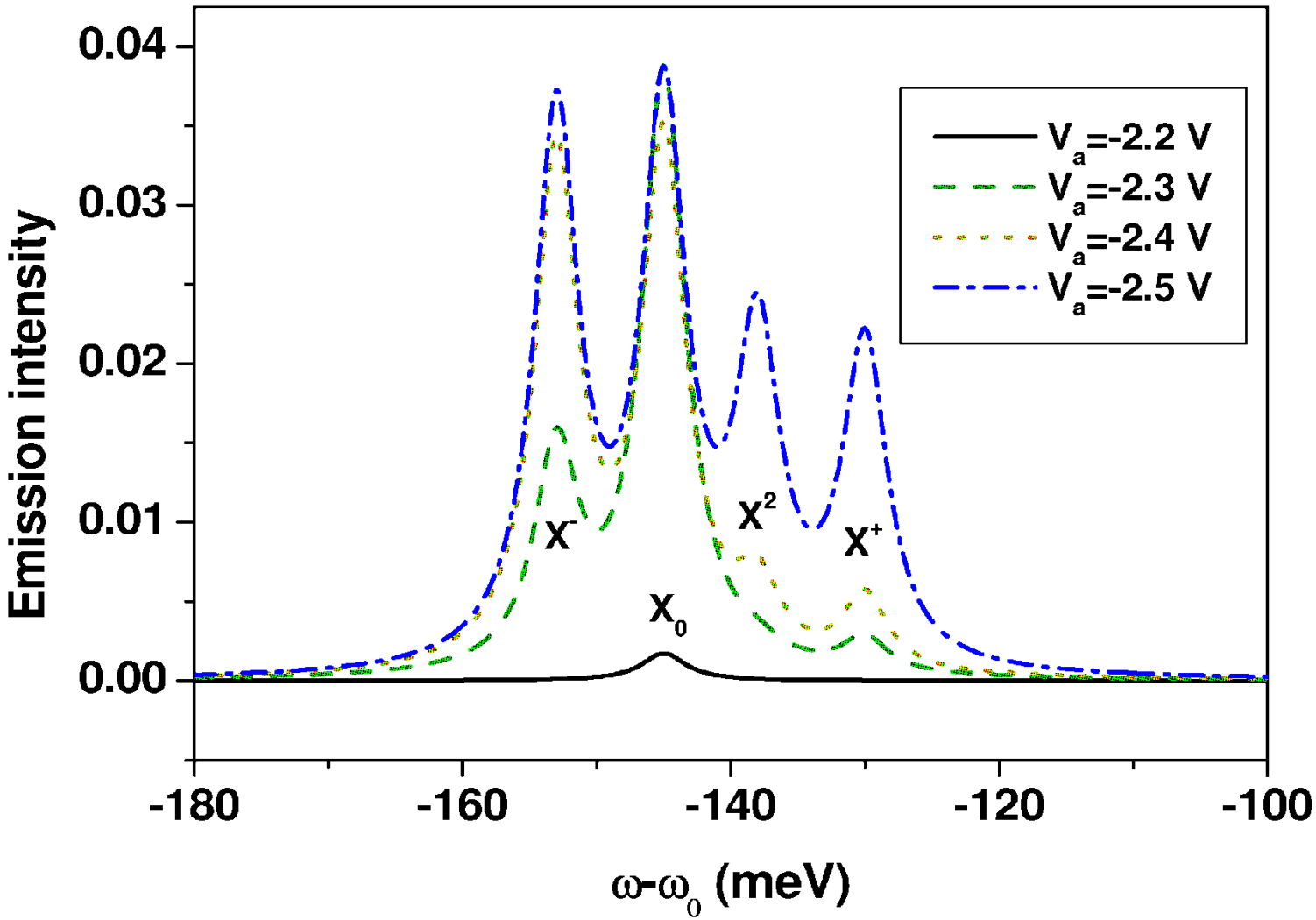

Symmetry-adapted basis for large supercells

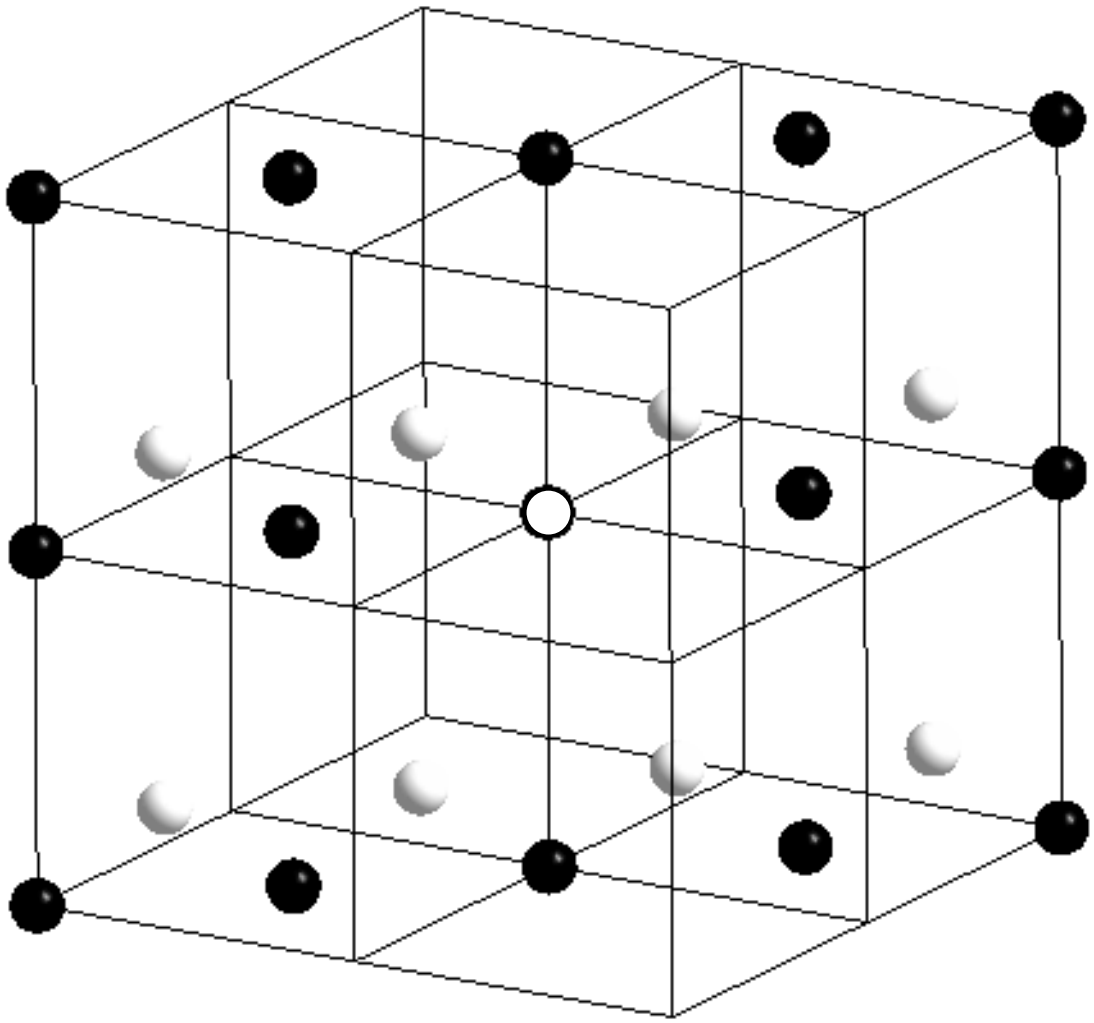

Coupled-wave transfer method

- Energy and wave functions computed using a stabilized transfer matrix technique by dividing the system into many slices along growth direction.
- Envelope function approximation with energy-dependent effective mass is used.
- Effective-mass Hamiltonian in k-sapce:

$$[(k_x^2+k_y^2)/m_t(E)+\partial_z^2/m_l(E)-E]F(\mathbf{k}) +\Sigma_{\mathbf{k}'}[V(\mathbf{k},\mathbf{k}')+V_{imp}(\mathbf{k},\mathbf{k}')]F(\mathbf{k}')=0$$

is solved via plane-wave expansion in each slice.

- 14-band k·p effects included perturbatively in optical matrix elements calculation
- Dopant effects incorporated as screened Coulomb potential
- The technique applies to quantum wells and quantum dots (or any 2D periodic nanostructures)

Charge densities of low-lying states in lens-shaped QD

s-like

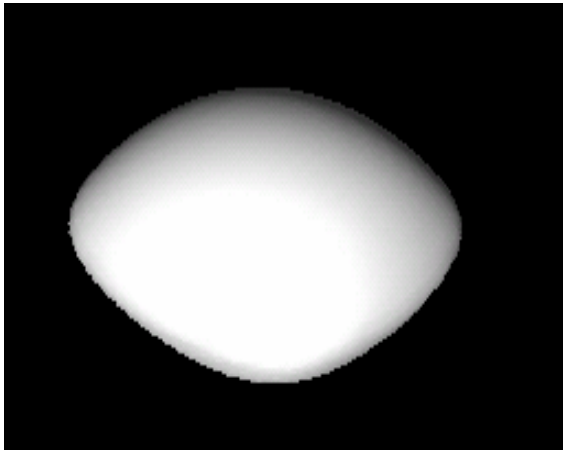

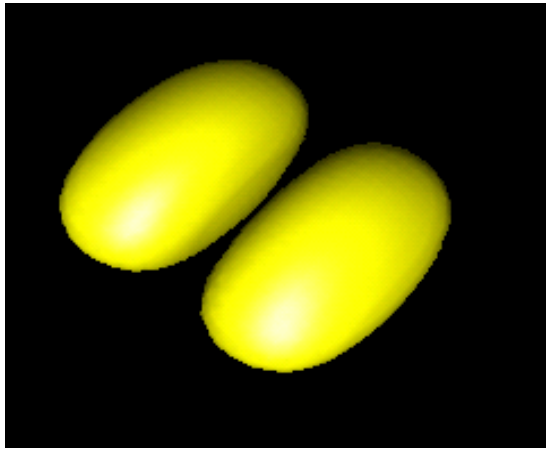

p_x/p_y like

d-like

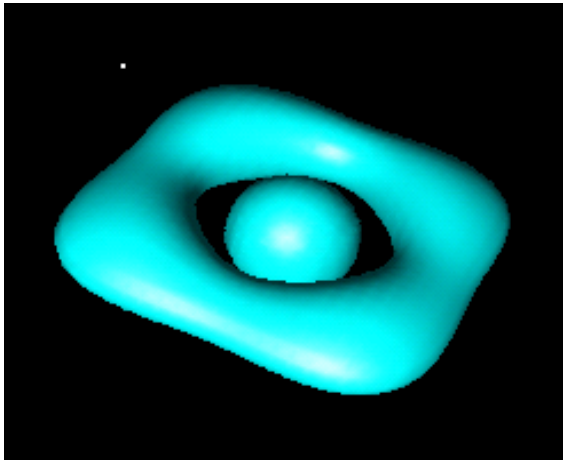

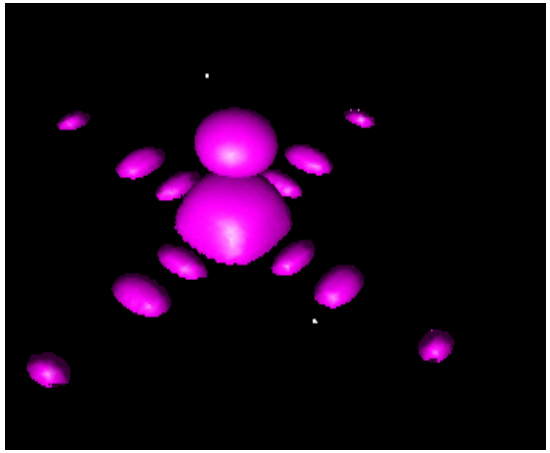

p_z like

Quantum well intrasubband photodetector (QWISP) for far infared and terahertz radiation detection

[Ting et al., APPLIED PHYSICS LETTERS 91, 073510 (2007)]

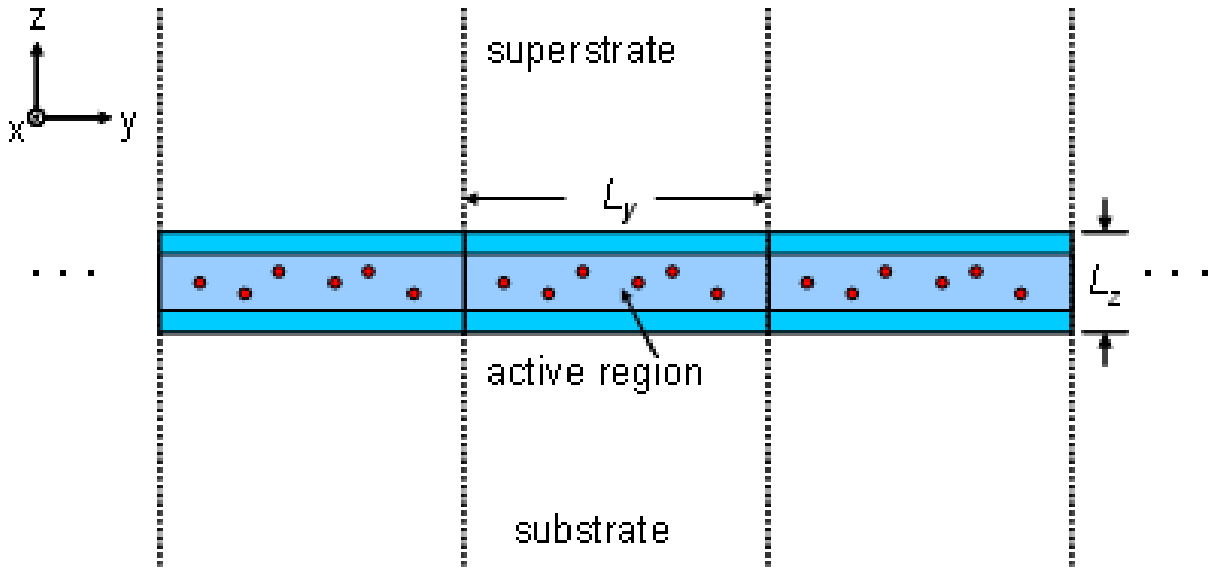

Fig. 4 A schematic illustration of the laterally repeating supercell geometry used in our simulations. Note that the supercell also repeats in the x direction with periodicity of L_x (not drawn). The example shown in this figure illustrates a quantum well containing several randomly placed dopant impurities.

Quantum well intrasubband photodetector (QWISP) for far infared and terahertz radiation detection

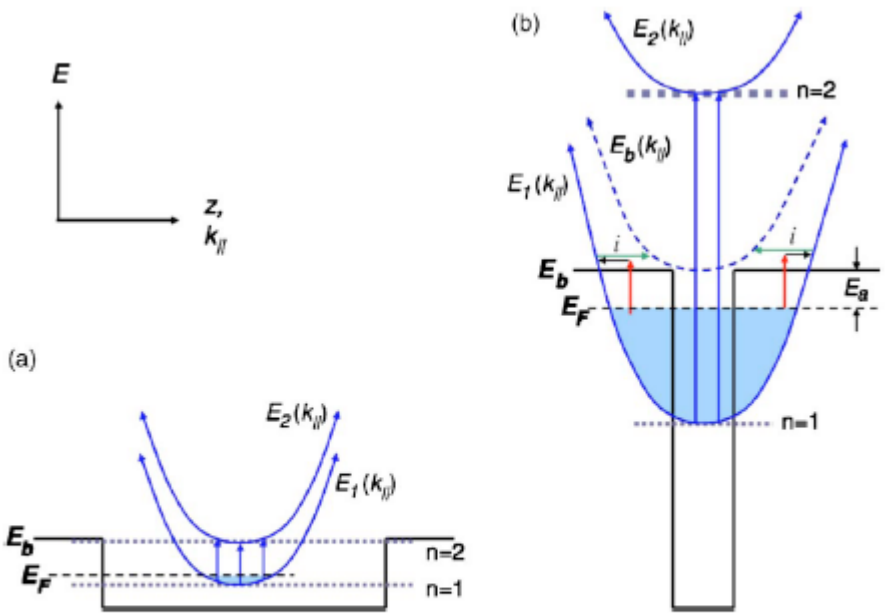

FIG. 1. (Color online) Schematic illustrations of the energy dispersions and energy band diagrams of (a) FIR/terahertz QWIP; (b) QWISP showing intersubband and impurity scattering assisted intrasubband optical absorption and carrier extraction mechanisms.

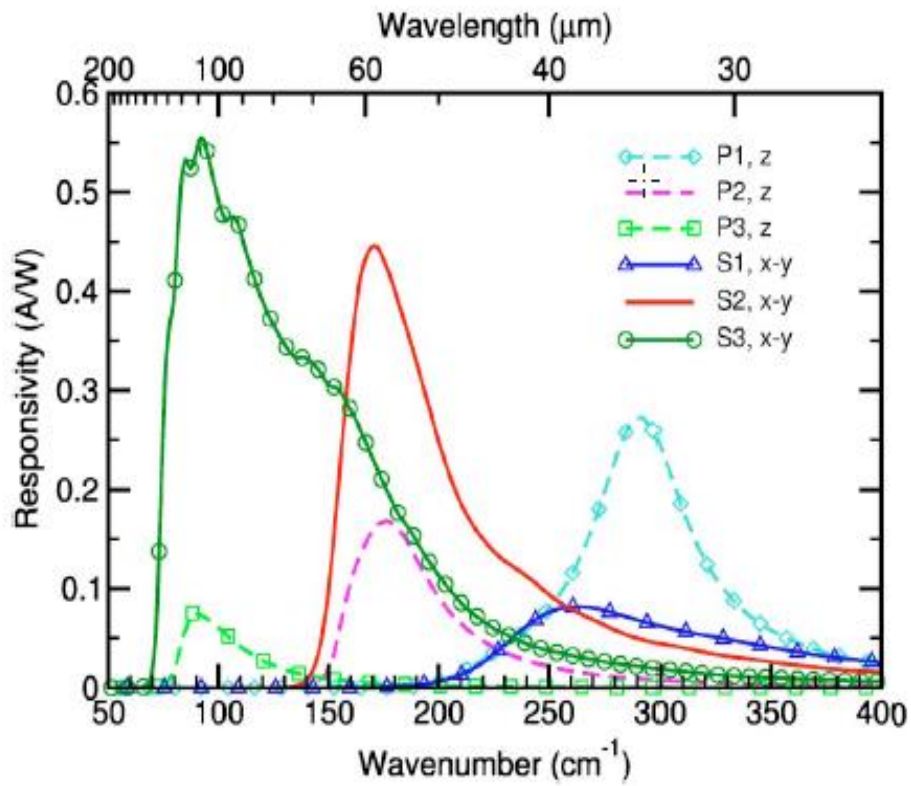

FIG. 3. (Color online) Low-temperature FIR/terahertz QWIP (set P) side-incidence responsivity and QWISP (set S) normal-incidence responsivity. Modeling parameters are listed in Table I.

Quantum well intrasubband photodetector (QWISP) for far infared and terahertz radiation detection

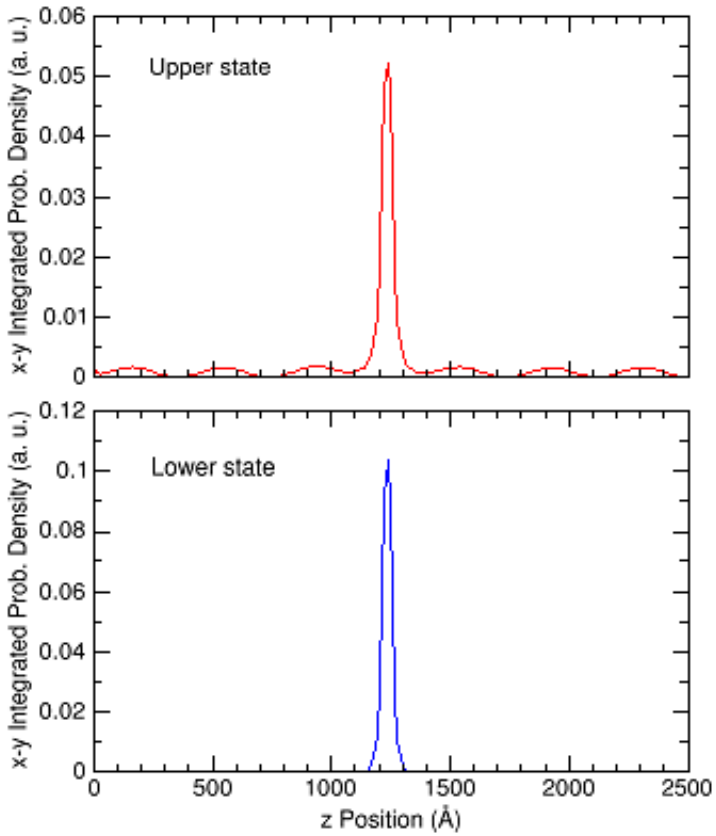

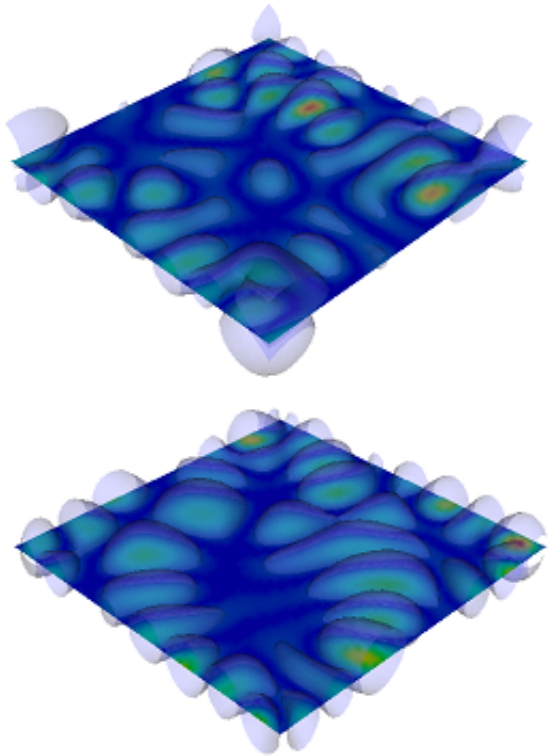

Fig. 5 The zero-bias wave functions of a pair of states involved in an intra-subband transition in a QWISP structure. The energy of the lower state is slightly below the Fermi level, and the energy of the upper state is just above the barrier band edge. The left panel shows the in-plane averaged probability densities as functions of z (growth direction). The random dopant distribution induced in-plane fluctuations of the wave functions are displayed in the right panel, which shows the translucent probability density isosurfaces, overlaid on top of probability density color contour plane located at the middle of the quantum well.

Submonolayer QD infrared photodetector

[Ting et al., APPLIED PHYSICS LETTERS 94, 1 (2009)]

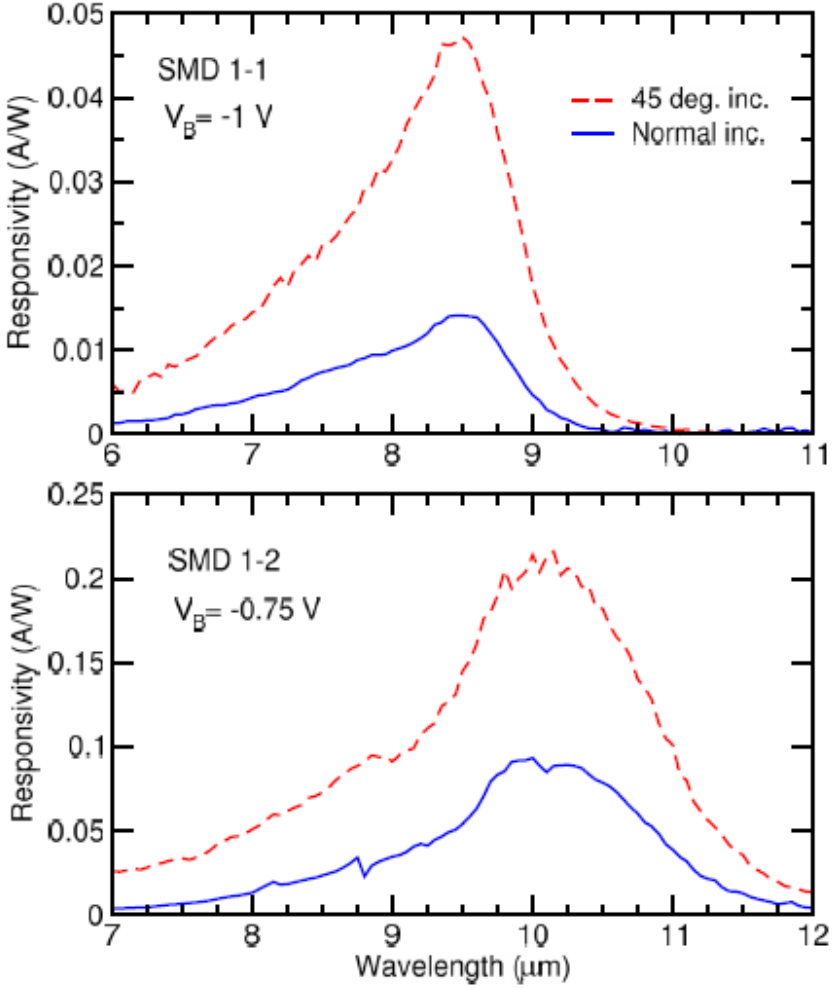

FIG. 2. (Color online) Measured normal and 45° incidence spectral responsivity curves for two SML QDIP samples.

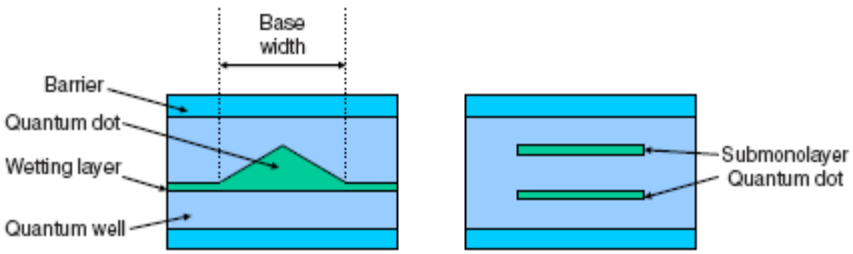

FIG. 1. (Color online) The left panel illustrates a conventional DWELL structure where a SK QD, consisting of pyramidal shape QD resting on a wetting layer, is embedded in a QW structure. The right panel show two stacks of SML QDs embedded in a QW.

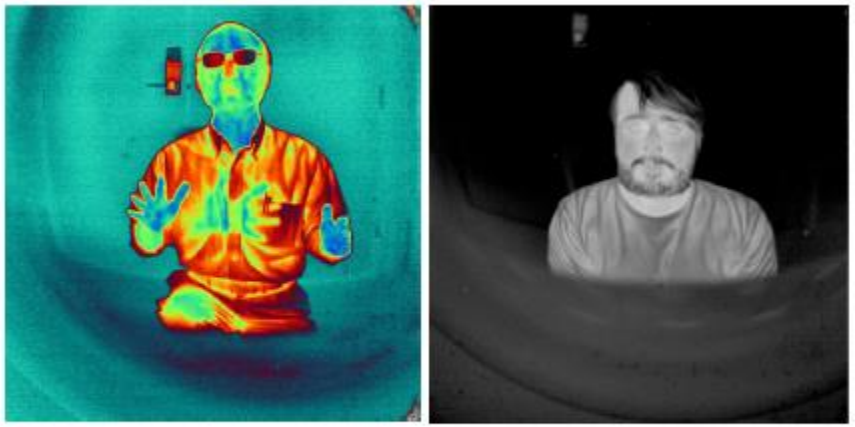

FIG. 4. (Color online) 80 K images taken with a 1024×1024 pixel SML QDIP FPA with $f/2$ optics.

Optical absorption spectra of Si

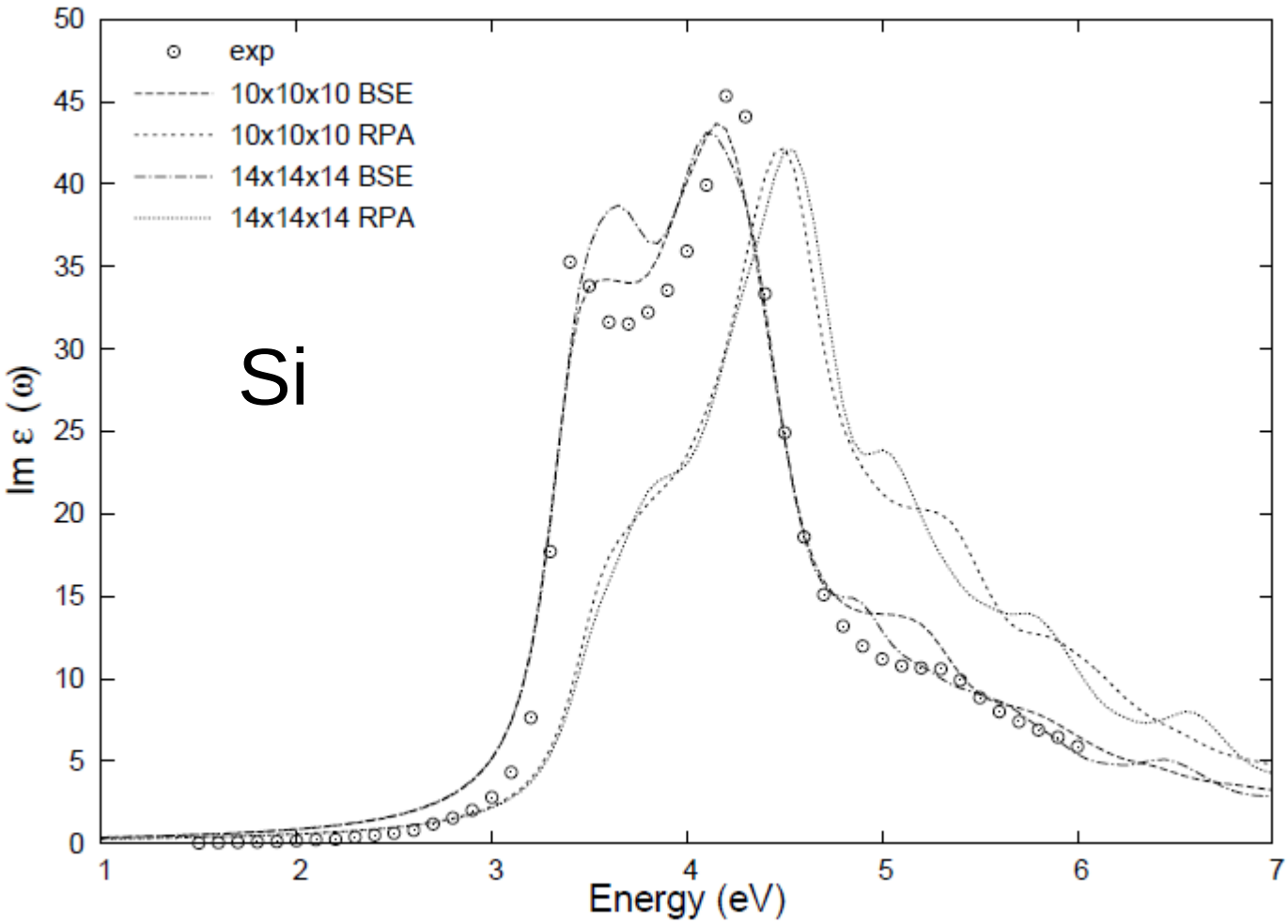

•Comparison in CPU time

- The algorithm is tested on SiH_4 with a XEON 3GHz/4GB PC.

Methods	Memory	CPU Usage
Straight PW	3GB	24hrs
Fully symmetrized	50MB	5mins

- Memory reduced to 2%, CPU reduced to 0.3%.
- The coding is much more complicated.

•GW approximation for Quasi-particle energy

$$E_n^{QP} \equiv \epsilon_n + \langle \phi_n \mid \Sigma(E_n^{QP}) - V_{xc} \mid \phi_n \rangle$$
$$\approx \epsilon_n + Z_i \langle \phi_n \mid \Sigma(\epsilon_n) - V_{xc} \mid \phi_n \rangle \qquad (2)$$

with $Z_n^{-1} = 1 - \langle \phi_n \mid d\Sigma/d\epsilon|_{\epsilon_n} \mid \phi_n \rangle$.

In real space and energy domain, we have,

$$\Sigma(\mathbf{r}, \mathbf{r}'; \omega) = \frac{i}{2\pi} \int_{-\infty}^{\infty} d\omega' \; W(\mathbf{r}, \mathbf{r}'; \omega') \; G(\mathbf{r}, \mathbf{r}'; \omega - \omega') e^{i\omega'\delta}, \qquad (13)$$

where the screened Coulomb interaction W is expressed as,

$$W(\mathbf{r}, \mathbf{r}'; \omega) = \int d^3\mathbf{r}'' v(\mathbf{r} - \mathbf{r}'') \; \epsilon^{-1}(\mathbf{r}'', \mathbf{r}'; \omega) \qquad (14)$$

where $v(\mathbf{r} - \mathbf{r}'')$ is the Coulomb interaction $1/|\mathbf{r} - \mathbf{r}''|$ and G is the one-particle Green's function. G itself depends on Σ through the Dyson equation and should arguably be determined self-consistently. In practice, however, in calculations for real systems, G can approximated by the non-interacting LDA Green's function, i.e.,

$$G^{LDA}(\mathbf{r}, \mathbf{r}'; \omega) = \sum_n \frac{\Psi_{n\mathbf{k}}(\mathbf{r}) \; \Psi^*_{n\mathbf{k}}(\mathbf{r}')}{\omega - \epsilon_n - i\eta_n} \qquad (15)$$

$$\Delta_n(E_n) \equiv \langle \phi_n \mid \Sigma(E_n) - V_{xc}\delta(\mathbf{r} - \mathbf{r}') \mid \phi_n \rangle$$
$$= \int d\mathbf{r} d\mathbf{r}' \phi_n^*(\mathbf{r}) \Sigma(\mathbf{r}, \mathbf{r}'; \epsilon_n) \phi_n(\mathbf{r}')$$
$$- \int d\mathbf{r} \phi_n^*(\mathbf{r}) V_{xc}(\mathbf{r}) \phi_{n'}(\mathbf{r}) \qquad (18)$$

In our scheme, we first workout W in reciprocal space. We define the matrix element

$$W_{\mathbf{G}\mathbf{G}'}(\omega) \equiv \langle \mathbf{G} \mid W(\omega) \mid \mathbf{G}' \rangle = \frac{1}{V_{cell}} v_{\mathbf{G}} \epsilon^{-1}_{\mathbf{G}\mathbf{G}'}(\omega), \qquad (19)$$

where V_{cell} is the volume of the supercell and $v_{\mathbf{G}}$ is the Fourier transform of the Coulomb interaction.

In real space, we have,

$$W(\mathbf{r}, \mathbf{r}'; \omega) = \sum_{\mathbf{G}, \mathbf{G}'} e^{-i\mathbf{G}\mathbf{r}} W_{\mathbf{G}, \mathbf{G}'}(\omega) e^{i\mathbf{G}'\mathbf{r}'} \qquad (20)$$

• ω Integration & plasma pole approximation

$$\Sigma_n(E_n) = \sum_{m\mathbf{GG}'} \zeta^*_{nm}(\mathbf{G})\zeta_{nm}(\mathbf{G}') \cdot \frac{i}{2\pi}\int d\omega' \frac{W_{\mathbf{GG}'}(\omega')}{\omega' - \omega_{mn} - i\eta_m} = \sum_m \frac{i}{2\pi}\int d\omega' \frac{\bar{W}_{nm}(\omega')}{\omega' - \omega_{mn} - i\eta_m} \quad (24)$$

where

$$\bar{W}_{nm}(\omega) = \sum_{\mathbf{GG}'} \zeta^*_{nm}(\mathbf{G}) W_{\mathbf{GG}'}(\omega')\zeta_{nm}(\mathbf{G}') \quad (25)$$

and η_m is a small imaginary part depending on m,

$$\eta_m = \begin{cases} -\delta & for\ m = unocc, \\ +\delta & for\ m = occ \end{cases} \quad (26)$$

Note that $\epsilon^{-1}(\omega) - 1$ is an analytic function, which decays to zero as $|\omega| \to \infty$ and has no pole in the upper half of the complex ω plane for retarded screening. So is the function $\bar{W}_{nm}(\omega) - v_{nm}$. These properties allow us to perform the ω' integral in Equ.(24) analytically.

For retarded screening, the polarization and dielectric function have poles in the lower half of the complex plane. This means that, in time domain, $t \to 0^-$.

$$\Sigma_n(E_n) = -\sum_m^{occ} \bar{W}_{nm}(\omega_{mn}) - \sum_m \sum_j \frac{z_j(nm)}{\omega_{mn} + \omega_j}. \quad (27)$$

In the above equation, the first term is due to the screened exchange while the second term the Coulomb-hole (COH) contribution, which is a result beyond RPA.

•How to obtain symmetrization coefficients

To obtain the symmetrization coefficients, $C(i, lm)$, we first construct the lattice harmonics at each site j. The lattice harmonics is the linear combination of spherical harmonics of the same l that transforms like a basis function (labelled ν) associated with an irreducible representation (labelled Γ) of a point group. We define

$$K_l^{\Gamma\nu}(\mathbf{G}) = \sum_m C_{lm}^{\Gamma\nu} Y_{lm}(\mathbf{G}). \tag{1}$$

In general, these coefficients can be obtained via the use of projection operator. We have

$$C_{lm}^{\Gamma\nu} = \frac{n(\Gamma)}{h} \sum_\Lambda \Gamma_{\nu,\nu}(\Lambda) \mathcal{D}_{m,m'}^{(l)}(\Lambda), \tag{2}$$

where $n(\Gamma)$ is the dimension of irreducible representation, Γ, h is the order of the point group, Λ denotes a group operation, and $\mathcal{D}_{m,m'}^{(l)}(\Lambda) \equiv \int d\Omega Y_{lm}^*(\Omega) Y_{lm'}(\Lambda^{-1}\Omega)$, which can be evaluated efficiently via the Gaussian quadrature method.

Next we construct the symmetrized site functions for each shell, s defined as

$$S_s^{\Gamma\nu} = \sum_m C_s^{\Gamma\nu}(j) e^{i\mathbf{G}\cdot\mathbf{r}_j}. \tag{3}$$

using the projection operator, we obtain

$$C_s^{\Gamma\nu}(j) = \frac{n(\Gamma)}{h} \sum_\Lambda \Gamma_{\nu,\nu}(\Lambda) \mathcal{D}_{j,j'}^{(s)}(\Lambda), \tag{4}$$

where $\mathcal{D}_{j,j'}^{(s)}(\Lambda) \equiv \sum_{\mathbf{G}} e^{i\mathbf{G}\cdot(\mathbf{r}_j - \Lambda^{-1}\mathbf{r}_j)}$ which is 1 if $(\mathbf{r}_j - \Lambda^{-1}\mathbf{r}_j)$ is a lattice vector of the "superlattice" and zero otherwise. Finally, we use the direct products of cubic harmonics and the symmetrized site functions to obtain the fully symmetrized states. We have

$$\psi_{ls}^{\Gamma\mu} = \sum_{\gamma\nu,\gamma'\nu'} V_\mu^\Gamma(\gamma\nu, \gamma'\nu') K_l^{\gamma\nu} S_s^{\gamma'\nu'}, \tag{5}$$

where $V_\mu^\Gamma(\gamma\nu, \gamma'\nu')$ are the vector coupling coefficients, which are readily available in Ref.

•Ref. G. F. Koster, J. O. Dimmock, R. G. Wheeler, and H. Statz, in *Properties of the Thirty-Two Point Groups* (MIT Press, Cambridge, Massachusetts, 1963).

•Evaluating matrix elements

The most time consuming part of the LASTO code is the evaluation of the structure coefficients (α and β) and the overlap (S) and hamiltonian (H) matrices, which involve double summation over the reciprocal lattice vectors $\mathbf{G}$ and $\mathbf{G}'$. [14] For $\mathbf{k} = 0$ these matrices are given by

$$S_{N,N'} = \sum_{\tilde{N}} (\beta^*_{N\tilde{N}} \beta_{N'\tilde{N}} + \alpha^*_{N\tilde{N}} \alpha_{N'\tilde{N}} \langle \dot{g}_{\tilde{l}} | \dot{g}_{\tilde{l}} \rangle)$$

$$+ \frac{1}{v_s} \sum_{\mathbf{G}} \psi^*_N(\mathbf{G}) \psi_{N'}(\mathbf{G})$$

$$- \frac{1}{v_s^2} \sum_{\mathbf{G},\mathbf{G}'} \psi^*_N(\mathbf{G}) \psi_{N'}(\mathbf{G}') \sum_{\tilde{N}} e^{i(\mathbf{G}'-\mathbf{G})\cdot\mathbf{R}_{\tilde{i}}} f(|\mathbf{G}' - \mathbf{G}|),$$

$$H_{N,N'} = \epsilon \sum_{\tilde{N}} (\beta^*_{N\tilde{N}} \beta_{N'\tilde{N}} + \alpha^*_{N\tilde{N}} \alpha_{N'\tilde{N}} \langle \dot{g}_{\tilde{l}} | \dot{g}_{\tilde{l}} \rangle)$$

$$+ \frac{1}{v_s} \sum_{\mathbf{G}} \psi^*_N(\mathbf{G}) (|\mathbf{G}|^2 + V_0) \psi_{N'}(\mathbf{G})$$

$$+ \frac{1}{2} R_s^2 \sum_{\tilde{N}} [g'_{\tilde{l}} \dot{g}_{\tilde{l}} (\beta^*_{N\tilde{N}} \alpha_{N'\tilde{N}} + \alpha^*_{N\tilde{N}} \beta_{N'\tilde{N}}) + g_{\tilde{l}} g'_{\tilde{l}} \beta^*_{N\tilde{N}} \beta_{N'\tilde{N}}$$

$$+ \dot{g}'_{\tilde{l}} \dot{g}_{\tilde{l}} \alpha^*_{N\tilde{N}} \alpha_{N'\tilde{N}}$$

$$- \frac{1}{v_s^2} \sum_{\mathbf{G},\mathbf{G}'} \psi^*_N(\mathbf{G}) \psi_{N'}(\mathbf{G}') \sum_{\tilde{N}} e^{i(\mathbf{G}'-\mathbf{G})\cdot\mathbf{R}_{\tilde{i}}} [\mathbf{G}\cdot\mathbf{G}' + V_0] f(|\mathbf{G}' - \mathbf{G}|),$$

where $f(|\mathbf{G}|)$ is the Fourier transform of the cut-off function $\theta(r_s - |\mathbf{r}|)$, v_s is the supercell volume, and $\psi_N(\mathbf{G})$ is the Fourier transform of the LASTO orbital, $\psi_N(\mathbf{r} - \mathbf{r_i})$.

•Symmetry reduction factor ~ n_h^2

•Optical spectra of 1nm Si clusters

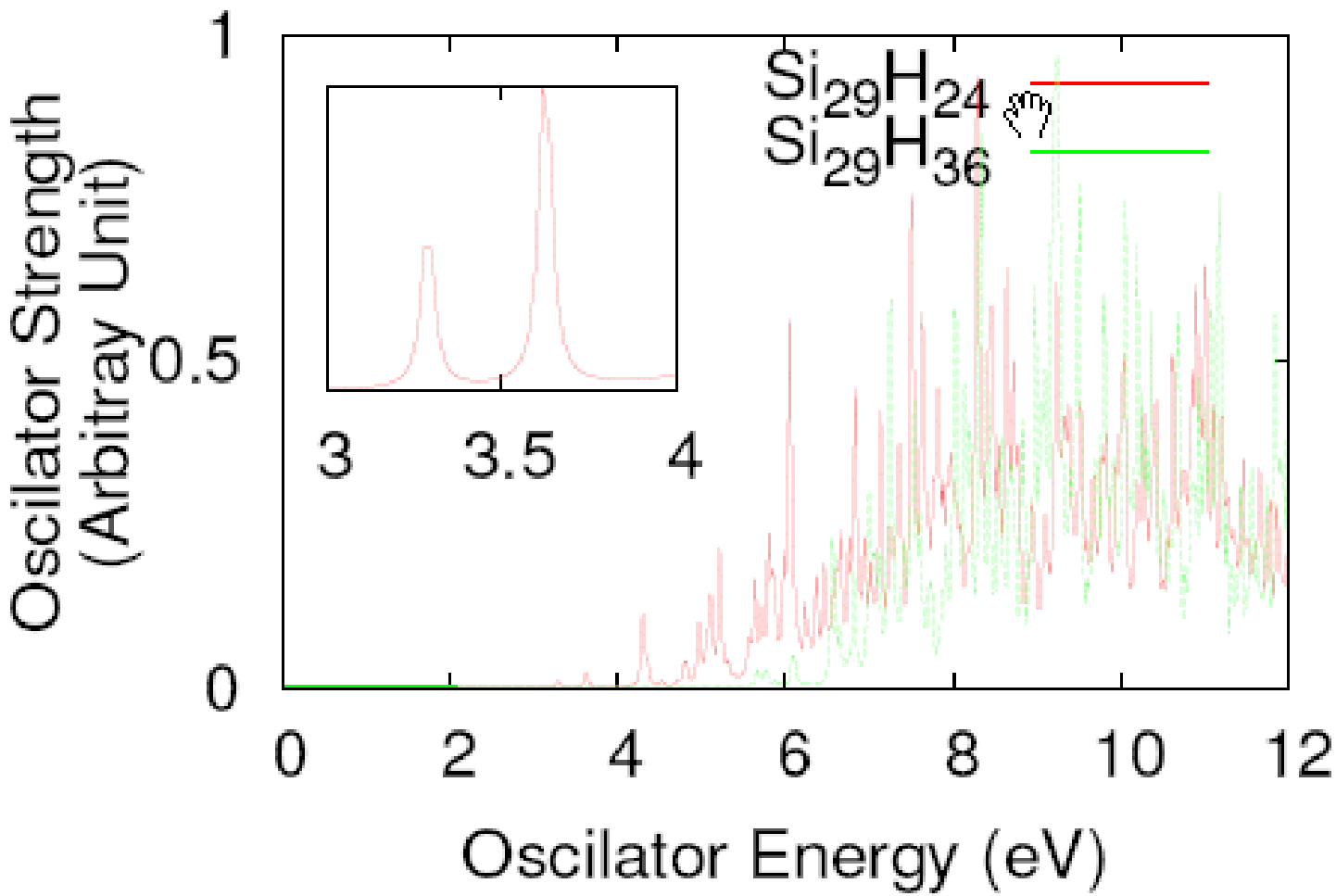

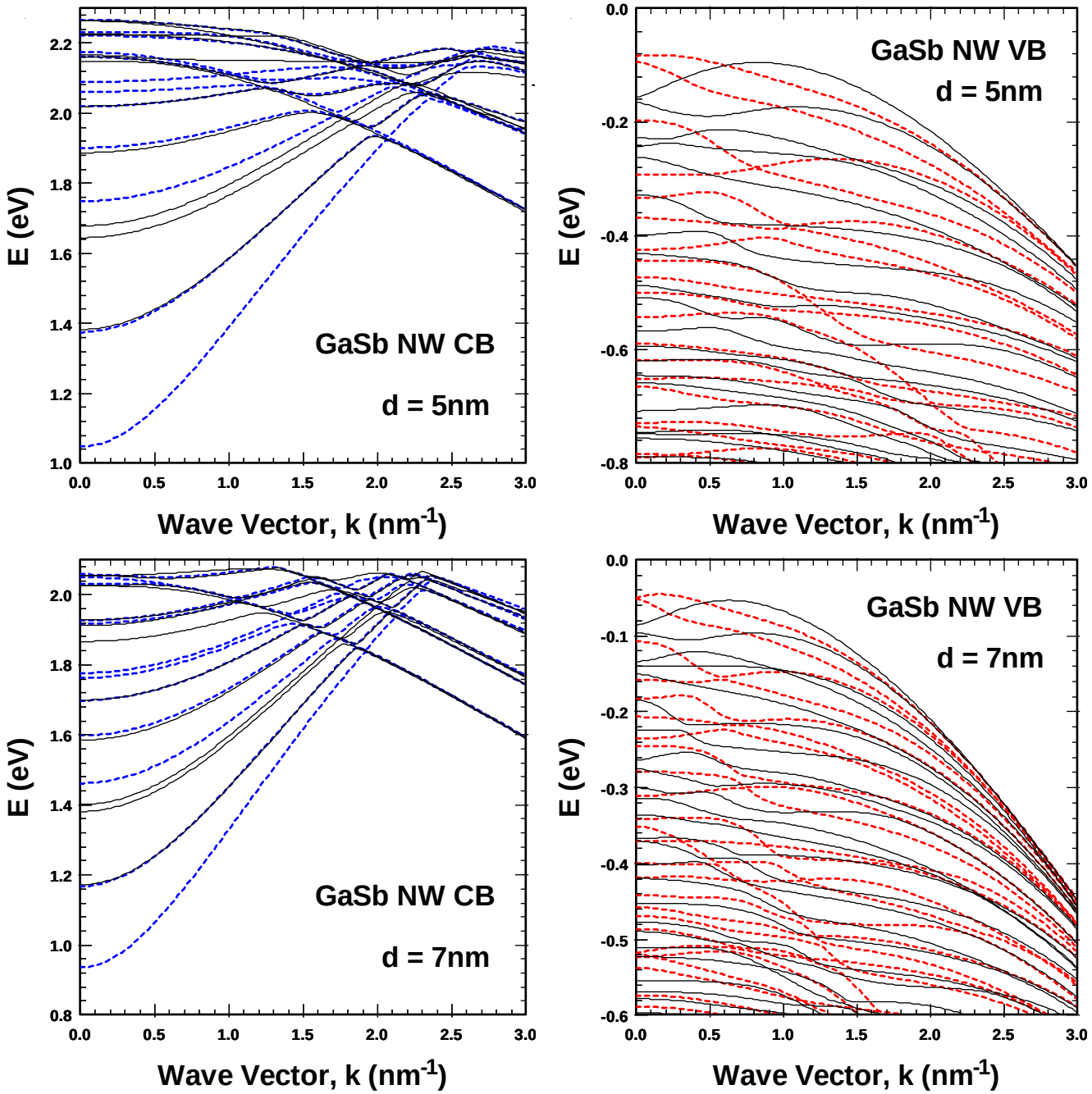
GaSb NW CB
d = 5nm
GaSb NW VB
d = 5nm
GaSb NW CB
d = 7nm
GaSb NW VB
d = 7nm
E (eV)
Wave Vector, k (nm-1)

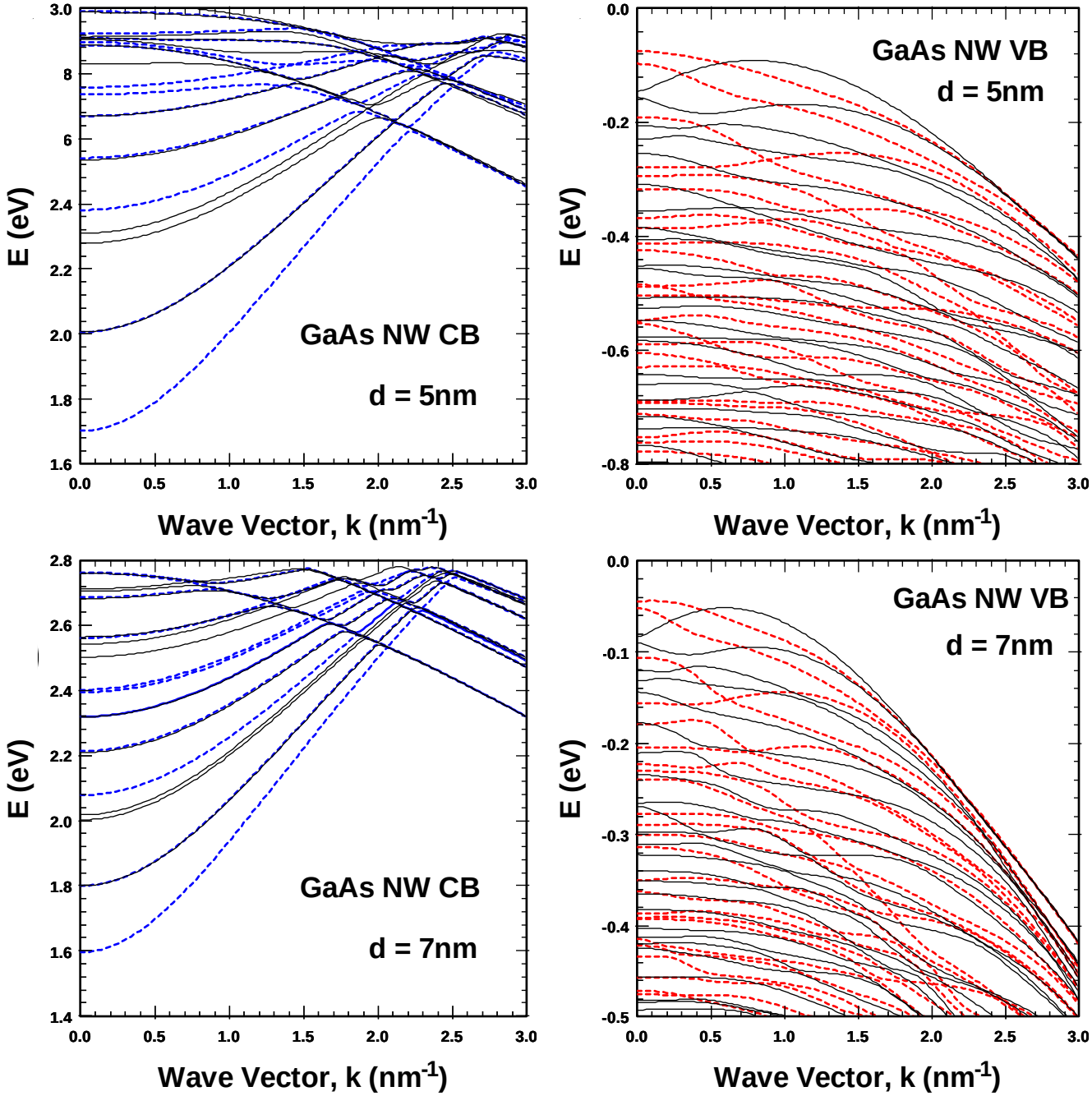
GaAs NW CB
d = 5nm
GaAs NW VB
d = 5nm
GaAs NW CB
d = 7nm
GaAs NW VB
d = 7nm
E (eV)
Wave Vector, k (nm-1)

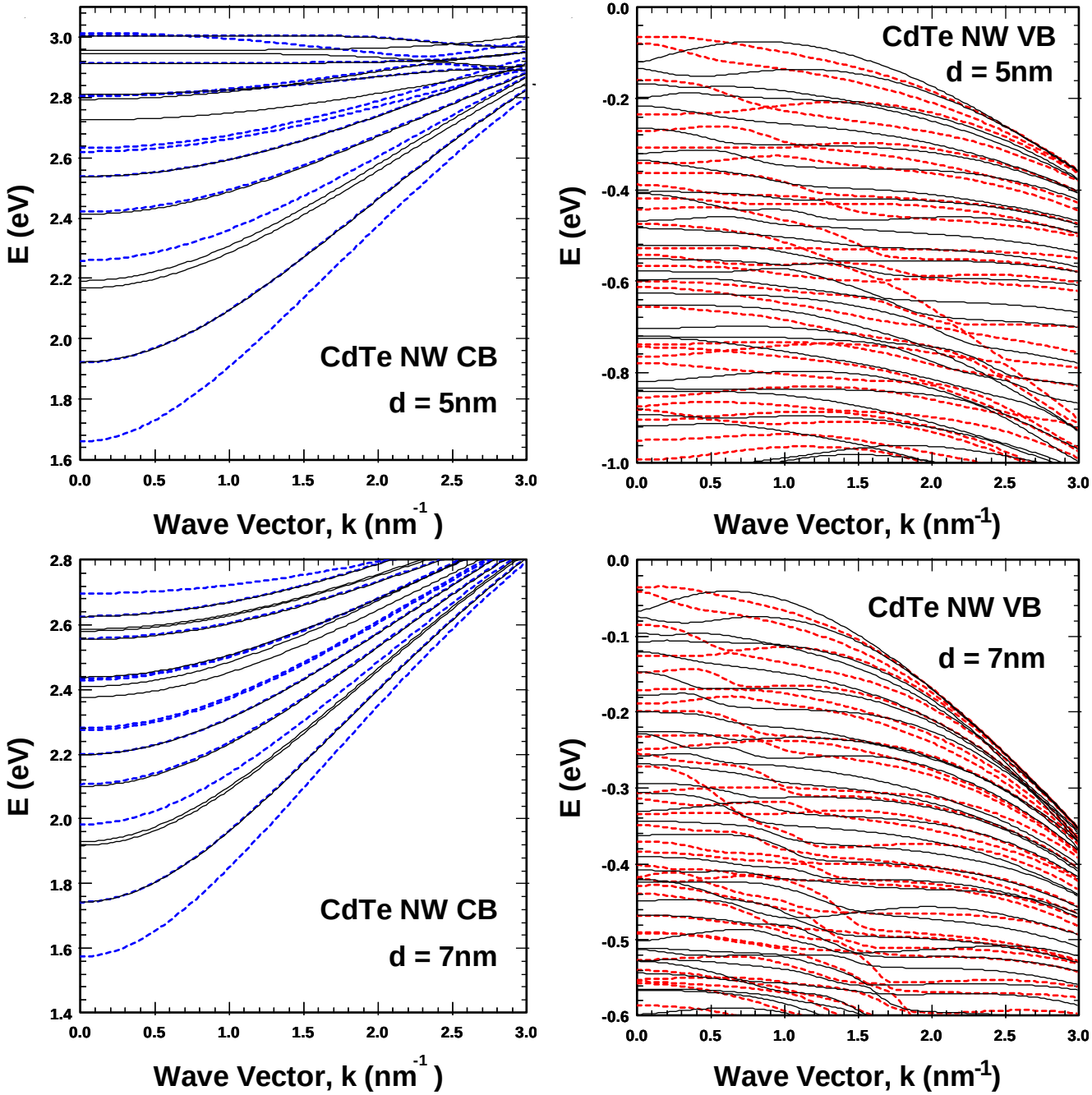
CdTe NW CB
d = 5nm
E (eV)
Wave Vector, k (nm^{-1})
CdTe NW VB
d = 5nm
E (eV)
Wave Vector, k (nm^{-1})
CdTe NW CB
d = 7nm
E (eV)
Wave Vector, k (nm^{-1})
CdTe NW VB
d = 7nm
E (eV)
Wave Vector, k (nm^{-1})

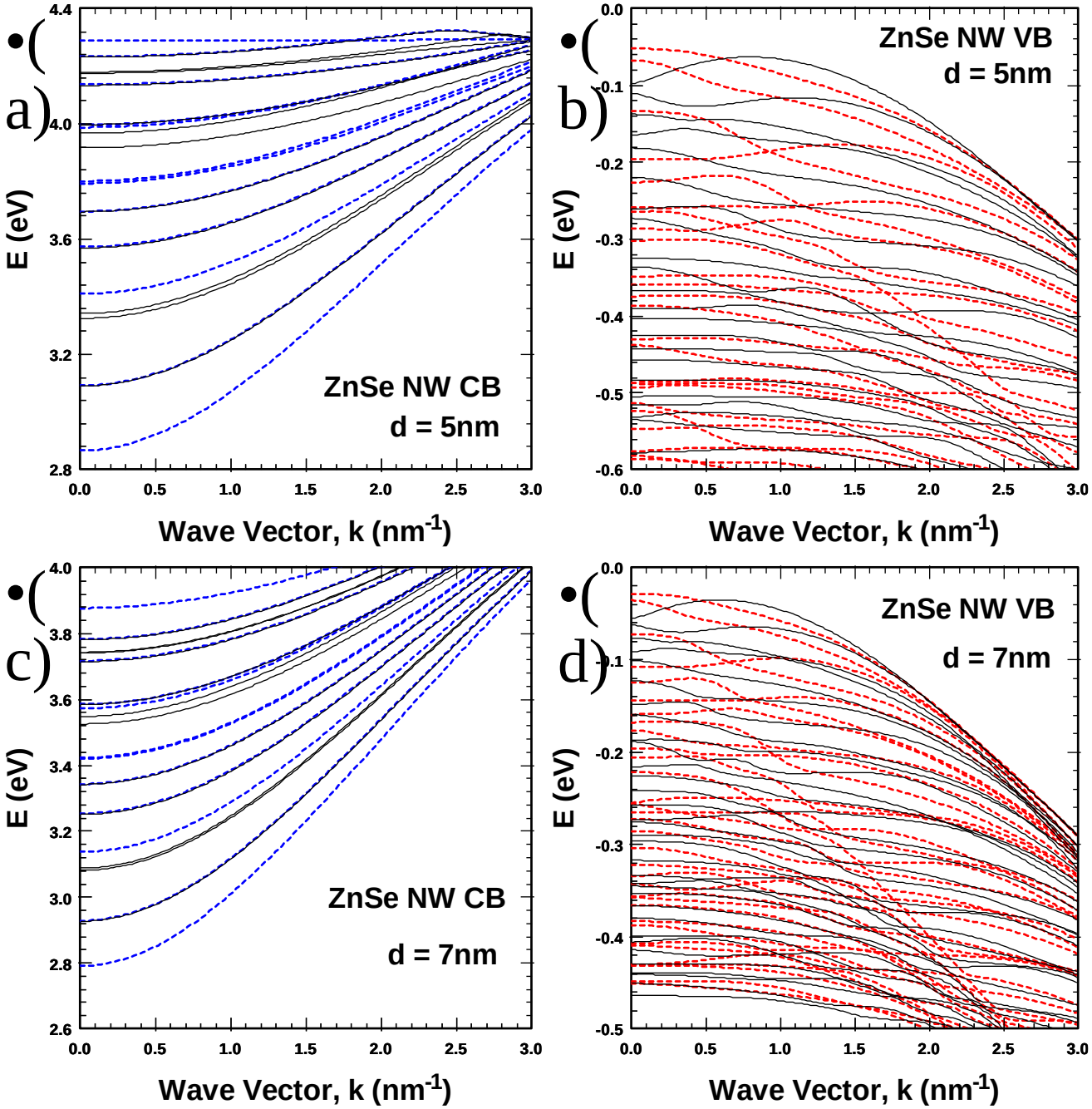
a)
ZnSe NW CB
d = 5nm
E (eV)
Wave Vector, k (nm-1)
b)
ZnSe NW VB
d = 5nm
E (eV)
Wave Vector, k (nm-1)
c)
ZnSe NW CB
d = 7nm
E (eV)
Wave Vector, k (nm-1)
d)
ZnSe NW VB
d = 7nm
E (eV)
Wave Vector, k (nm-1)

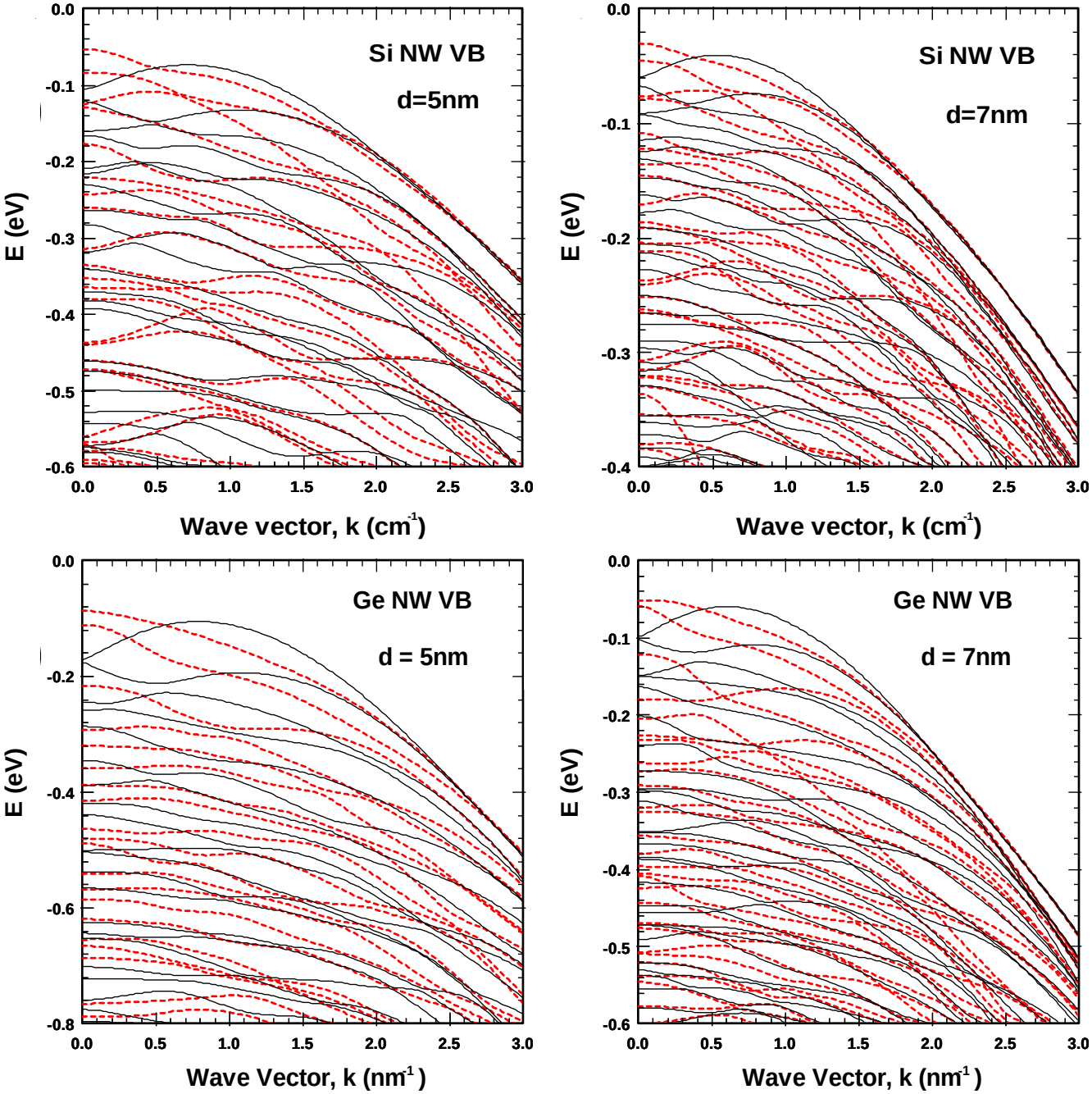
Si NW VB
d=5nm
E (eV)
Wave vector, k (cm-1)
Si NW VB
d=7nm
E (eV)
Wave vector, k (cm-1)
Ge NW VB
d = 5nm
E (eV)
Wave Vector, k (nm-1)
Ge NW VB
d = 7nm
E (eV)
Wave Vector, k (nm-1)

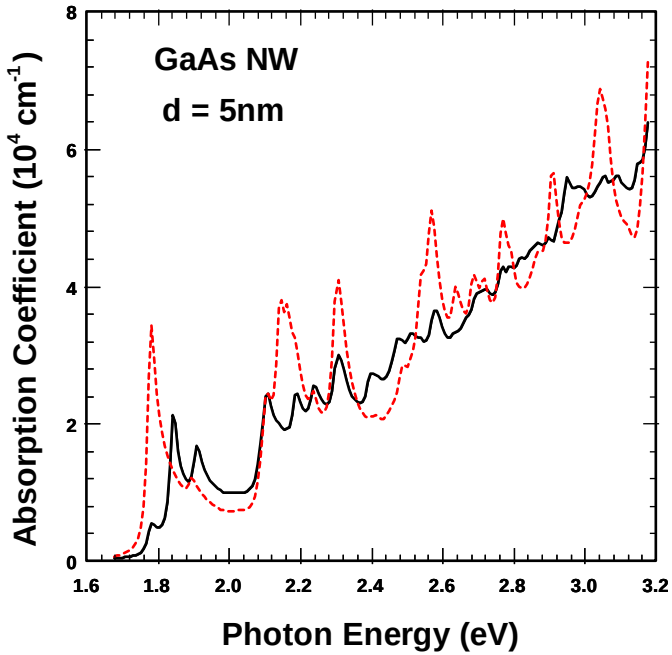
GaAs NW
d = 5nm
Absorption Coefficient (10^4 cm^{-1})
Photon Energy (eV)
0
2
4
6
8
1.6
1.8
2.0
2.2
2.4
2.6
2.8
3.0
3.2

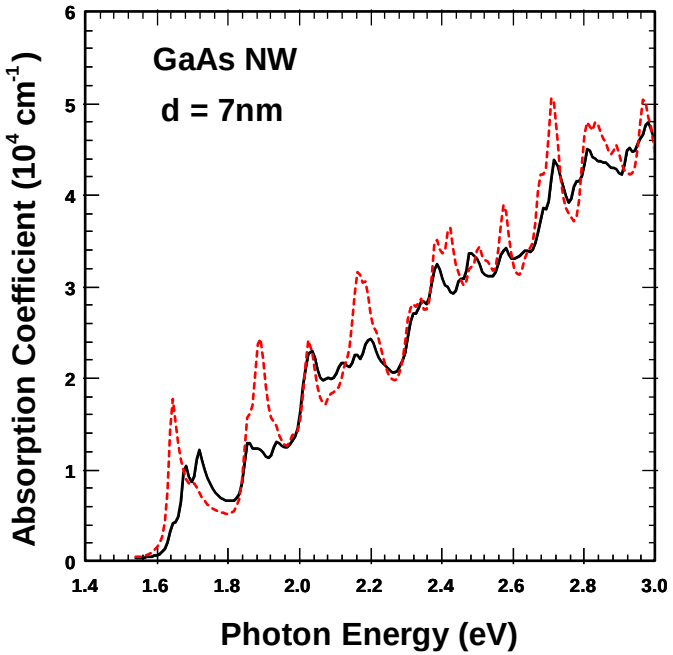
GaAs NW
d = 7nm
Absorption Coefficient (10^4 cm^{-1})
Photon Energy (eV)
0
1
2
3
4
5
6
1.4
1.6
1.8
2.0
2.2
2.4
2.6
2.8
3.0

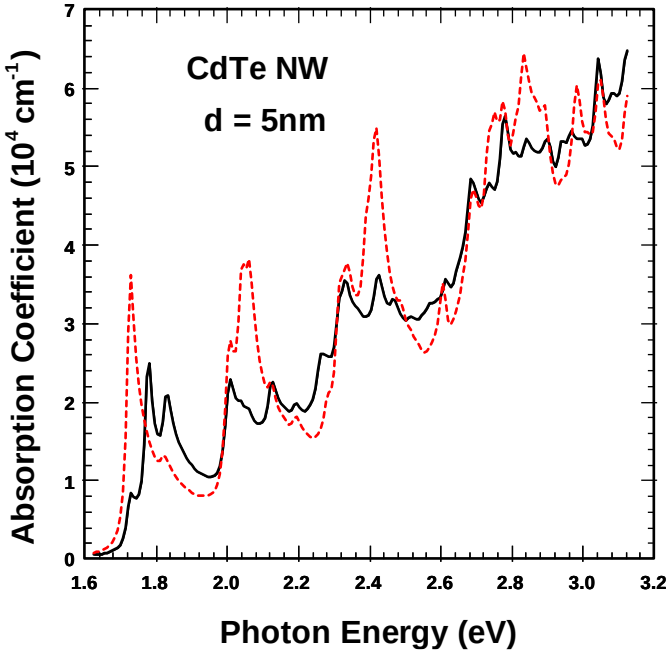
CdTe NW
d = 5nm
Absorption Coefficient (10^4 cm^{-1})
Photon Energy (eV)
0
1
2
3
4
5
6
7
1.6
1.8
2.0
2.2
2.4
2.6
2.8
3.0
3.2

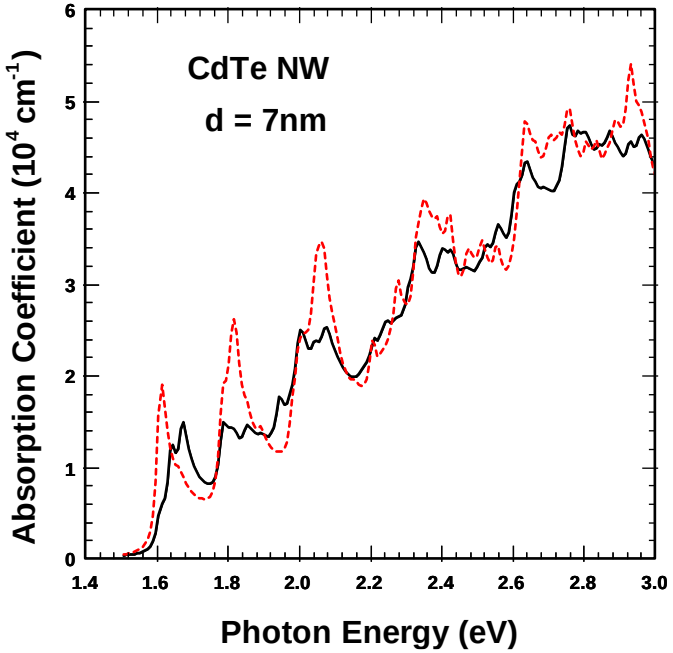
CdTe NW
d = 7nm
Absorption Coefficient (10^4 cm^{-1})
Photon Energy (eV)
0
1
2
3
4
5
6
1.4
1.6
1.8
2.0
2.2
2.4
2.6
2.8
3.0

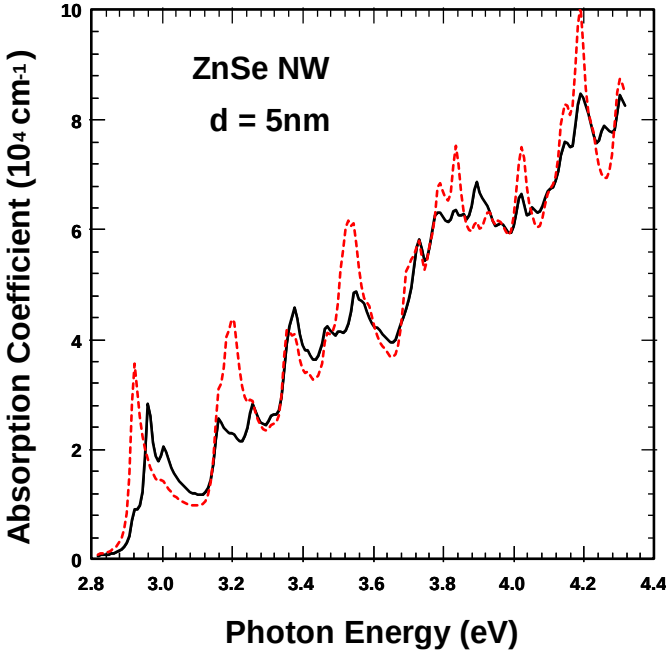
ZnSe NW
d = 5nm
Absorption Coefficient (10^4 cm^{-1})
Photon Energy (eV)
0
2
4
6
8
10
2.8
3.0
3.2
3.4
3.6
3.8
4.0
4.2
4.4

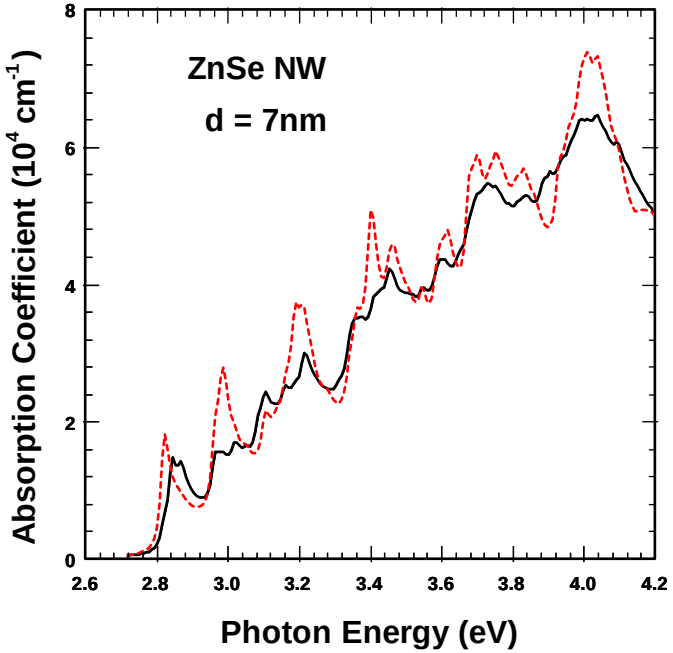
ZnSe NW
d = 7nm
Absorption Coefficient (10^4 cm^{-1})
Photon Energy (eV)
0
2
4
6
8
2.6
2.8
3.0
3.2
3.4
3.6
3.8
4.0
4.2

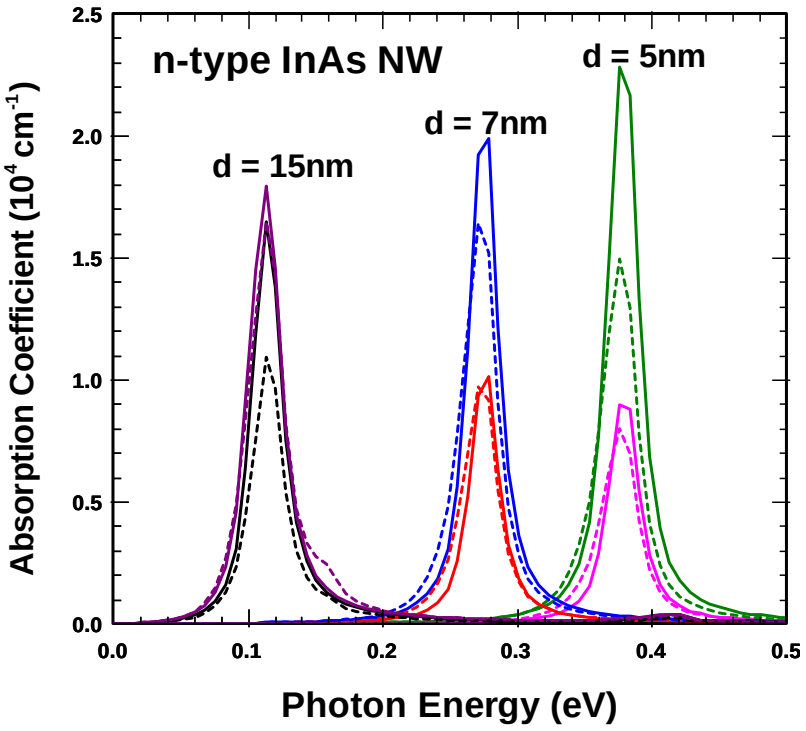
n-type InAs NW
d = 15nm
d = 7nm
d = 5nm
Absorption Coefficient (10^4 cm^{-1})
Photon Energy (eV)
0.0
0.5
1.0
1.5
2.0
2.5
0.0
0.1
0.2
0.3
0.4
0.5

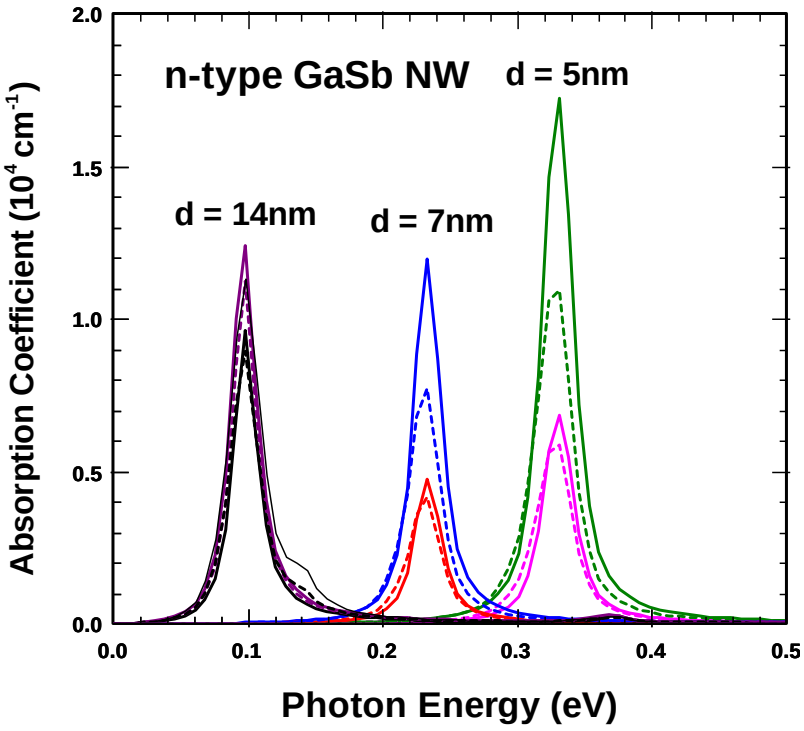
n-type GaSb NW
d = 14nm
d = 7nm
d = 5nm
Absorption Coefficient (10^4 cm^{-1})
Photon Energy (eV)
0.0
0.5
1.0
1.5
2.0
0.0
0.1
0.2
0.3
0.4
0.5

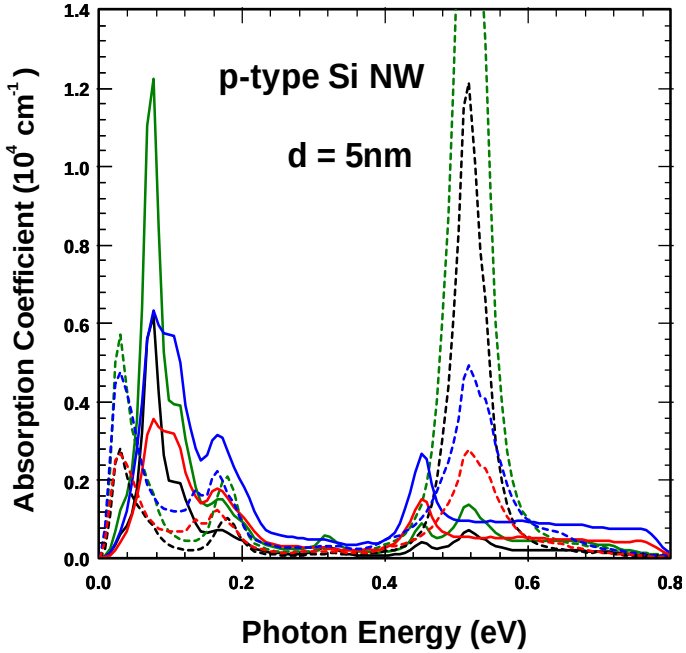
p-type Si NW
d = 5nm
Absorption Coefficient (10^4 cm^{-1})
Photon Energy (eV)
0.0
0.2
0.4
0.6
0.8
1.0
1.2
1.4

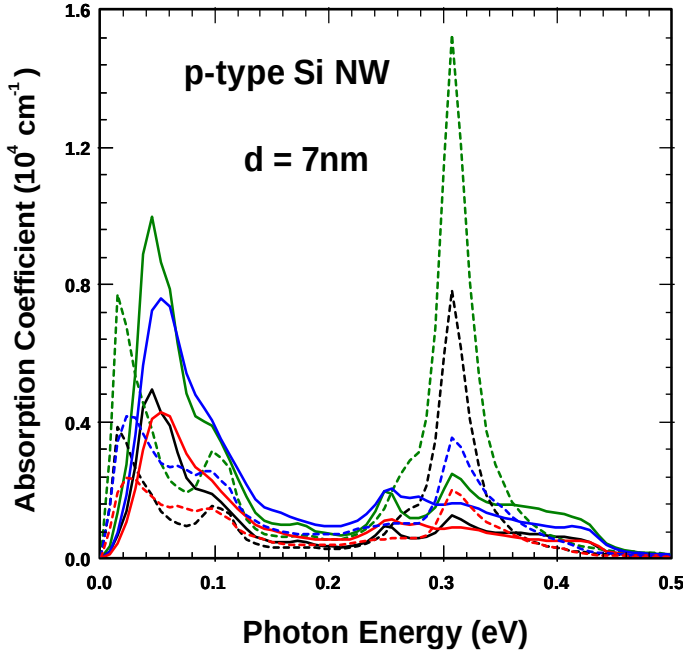
p-type Si NW
d = 7nm
Absorption Coefficient (10^4 cm^{-1})
Photon Energy (eV)
0.0
0.1
0.2
0.3
0.4
0.5
0.8
1.2
1.6

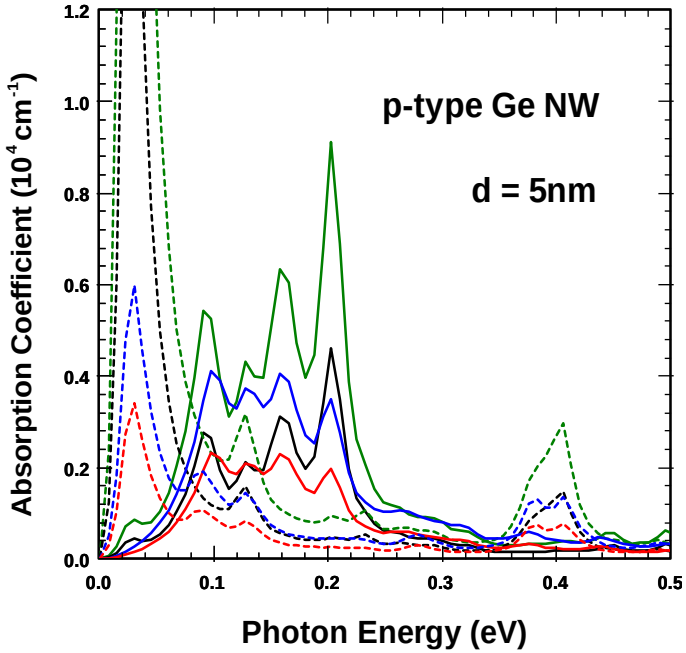
p-type Ge NW
d = 5nm
Absorption Coefficient (10^4 cm^{-1})
Photon Energy (eV)
0.0
0.1
0.2
0.3
0.4
0.5
0.6
0.8
1.0
1.2

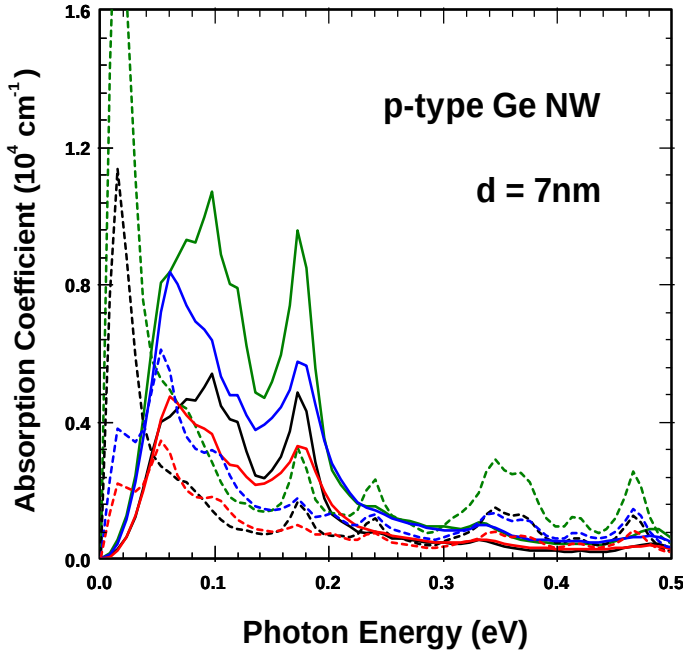
p-type Ge NW
d = 7nm
Absorption Coefficient (10^4 cm^{-1})
Photon Energy (eV)
0.0
0.1
0.2
0.3
0.4
0.5
0.8
1.2
1.6

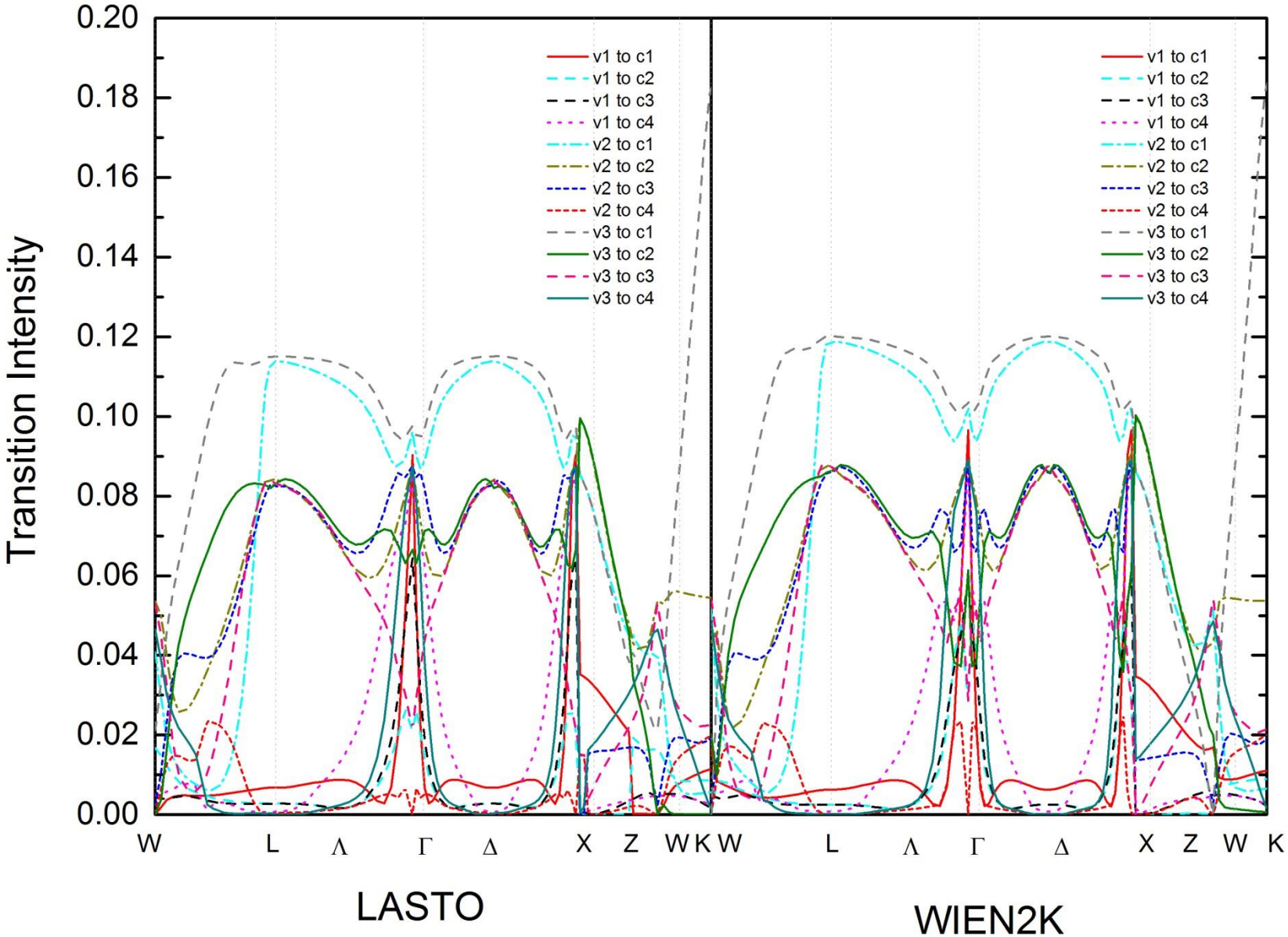
Transition Intensity
0.20
0.18
0.16
0.14
0.12
0.10
0.08
0.06
0.04
0.02
0.00
v1 to c1
v1 to c2
v1 to c3
v1 to c4
v2 to c1
v2 to c2
v2 to c3
v2 to c4
v3 to c1
v3 to c2
v3 to c3
v3 to c4
W L Λ Γ Δ X Z W K W L Λ Γ Δ X Z W K
LASTO
WIEN2K

Application to optical excitation of solids & superlattices

$$\Phi^{\lambda}(\mathbf{r}_e,\mathbf{r}_h)=\sum_{vc\mathbf{k}} A^{\lambda}_{vc\mathbf{k}}\psi^{*}_{v\mathbf{k}}(\mathbf{r}_h)\psi_{c\mathbf{k}}(\mathbf{r}_e).$$

$$\sum_{v'c'\mathbf{k}'} H^{e}_{vc\mathbf{k},v'c'\mathbf{k}'}A^{\lambda}_{v'c'\mathbf{k}'}=E^{\lambda}A^{\lambda}_{vc\mathbf{k}}.$$

•*K* = $H^{e}=H^{diag}+H^{dir}+2H^{x}.$

$$H^{diag}_{vc\mathbf{k},v'c'\mathbf{k}'}=(E_{c\mathbf{k}}-E_{v\mathbf{k}})\delta_{vv'}\delta_{cc'}\delta_{\mathbf{k}\mathbf{k}'}$$

$$\epsilon_2(\omega)=\frac{8\pi^2}{\Omega}\sum_{\lambda}\left|\sum_{vc\mathbf{k}} A^{\lambda}_{vc\mathbf{k}}\frac{\langle v\mathbf{k}|p_i|c\mathbf{k}\rangle^{\mathrm{LDA}}}{\varepsilon_{c\mathbf{k}}-\varepsilon_{v\mathbf{k}}}\right|^2\delta(E^{\lambda}-\omega)$$

•Use time-reversal symmetry

$$\Psi_{cv-\mathbf{k}}(\mathbf{r}_h,\mathbf{r}_e)=\Psi^{*}_{cv\mathbf{k}}(\mathbf{r}_h,\mathbf{r}_e)$$

$$<\Psi^{\pm}_{cv\mathbf{k}}|K|\Psi^{\pm}_{c'v'\mathbf{k}'}>=Re[<\Psi_{cv\mathbf{k}}|K|\Psi_{c'v'\mathbf{k}'}>\pm<\Psi_{cv\mathbf{k}}|K|\Psi_{c'v'-\mathbf{k}'}>],$$

$$<\Psi^{\pm}_{cv\mathbf{k}}|K|\Psi^{\mp}_{c'v'\mathbf{k}'}>=\pm Im[<\Psi_{cv\mathbf{k}}|K|\Psi_{c'v'\mathbf{k}'}>\mp<\Psi_{cv\mathbf{k}}|K|\Psi_{c'v'-\mathbf{k}'}>].$$

$$G(E)=G_0(E)+G_0(E)KG(E),$$

$$<\Psi^{\pm}_{cv\mathbf{k}}|G_0(E)p_\alpha|0>=<\Psi^{\pm}_{cv\mathbf{k}}|p|0>/[E-E_c(\mathbf{k})+E_v(\mathbf{k})+i\delta].$$

$$<\Psi^{\pm}_{cv\Lambda\mathbf{k}}|Gp_\alpha|0>=<\Psi^{\pm}_{cv\mathbf{k}}|Gp_{\Lambda\alpha}|0>,$$

•for k in IBZ

$$-Im<0|p_\alpha Gp_\alpha|0>=-Im\sum_{cvks}<0|p_\alpha|\Psi^{s}_{cv\Lambda\mathbf{k}}><\Psi^{s}_{cv\Lambda\mathbf{k}}|Gp_\alpha|0>$$

•[Puschnig* and C. Ambrosch-Draxl, PRB **66**, 165105 (2002)]

Piezoeletric Potential

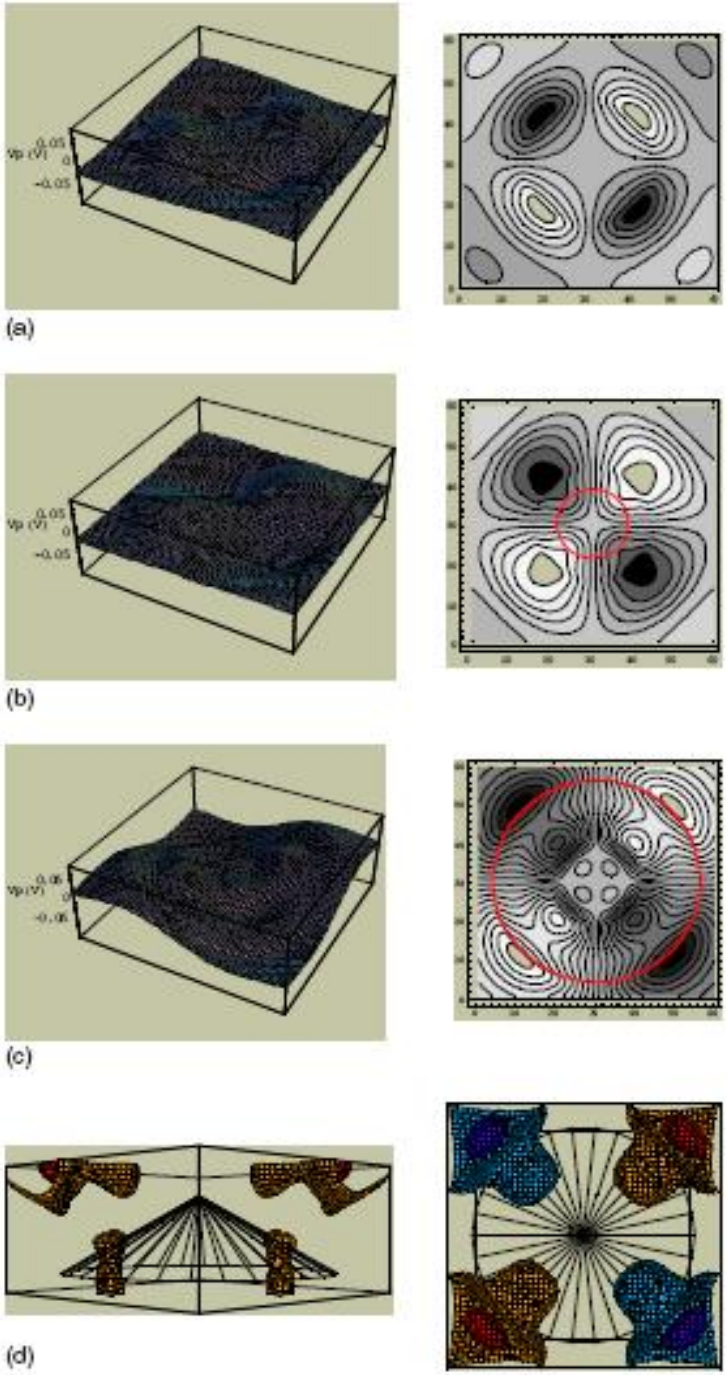

FIG. 5. (Color online) The piezoelectric potential V_p: (a) in the horizontal plane, $z=0$ containing the top of the cone; (b) in the horizontal plan $z=H/3$; (c) in the horizontal plane $z=H$. The left side figures are the three-dimensional plots and the right side figures are the contour plots. The red circles in these plots represent the cross sections of the QD with the horizontal planes. (d) equipotential surfaces of piezoelectric potential V_p for 0.065 V (red), −0.065 V (dark blue), 0.04 V (orange), and −0.04 V (blue). In the left side figure only the positive equipotential surfaces are plotted. In the right side figure are plots with a top view.

Supercell calculations in symmetry-adpated LASTO basis

[Y.-C. Chang, R. B. James, and J. W. Davenport, PRB **73**, 035211 (2006)]

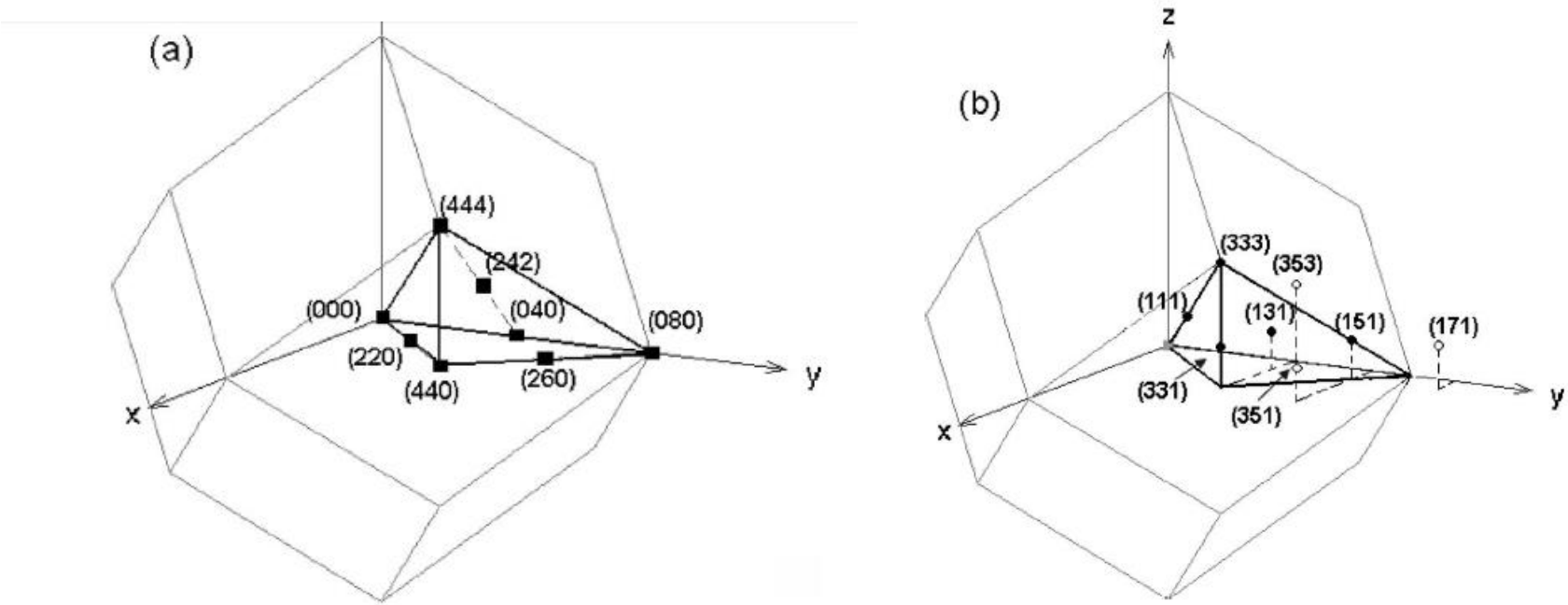

FIG. 1. (a) Wigner-Seitz cell of a 128-atom supercell. The solid squares indicate the positions of cations in the irreducible segment of the Wigner-Seitz cell. The coordinates are in units of $a/4$. (b) Wigner-Seitz cell of a 54-atom supercell. The solid circles indicate the positions of anions in the irreducible segment of the Wigner-Seitz cell. The open circles indicate the positions of anions outside the irreducible segment of the 54-atom supercell but within the irreducible segment of the 128-atom supercell.